

**CHARACTERIZATION OF BPHD, A C-C BOND HYDROLASE INVOLVED IN  
THE DEGRADATION OF POLYCHLORINATED BIPHENYLS**

by

Geoffrey P. Horsman

A THESIS SUBMITTED IN PARTIAL FULFILMENT OF  
THE REQUIREMENTS FOR THE DEGREE OF

DOCTOR OF PHILOSOPHY

in

THE FACULTY OF GRADUATE STUDIES  
(Biochemistry and Molecular Biology)

THE UNIVERSITY OF BRITISH COLUMBIA

January 2008

© Geoffrey P. Horsman, 2008

## ABSTRACT

Microbial aromatic compound degradation often involves carbon-carbon bond hydrolysis of a *meta*-cleavage product (MCP). BphD<sub>LB400</sub> (EC 3.7.1.8), the MCP hydrolase from the biphenyl degradation pathway of *Burkholderia xenovorans* LB400, hydrolyzes 2-hydroxy-6-oxo-6-phenylhexa-2,4-dienoate (HOPDA) to 2-hydroxypenta-2,4-dienoate (HPD) and benzoate. Although MCP hydrolases contain the catalytic triad (Ser112-His265-Asp237) and structural fold of the  $\alpha/\beta$ -hydrolase superfamily, previous studies suggest they deviate from the classical hydrolytic mechanism in two respects: (1) enol-keto tautomerization precedes hydrolysis and (2) hydrolysis involves a *gem*-diol intermediate.

Stopped-flow kinetic studies revealed rapid accumulation of a transient intermediate possessing a red-shifted absorption spectrum ( $\lambda_{\text{max}} = 492$  nm) versus HOPDA ( $\lambda_{\text{max}} = 434$  nm), consistent with an enzyme-bound, strained enolate (E:S<sup>sc</sup>). In studies with BphD<sub>LB400</sub> variants, S112A trapped the E:S<sup>sc</sup> intermediate, implying that Ser112 is required for subsequent tautomerization and hydrolysis. His265 is required for E:S<sup>sc</sup> formation, as H265A variants instead generated a species assigned to a non-strained HOPDA enolate, which was not spectroscopically observed in the WT enzyme. The proposed importance of double bond strain in the reaction was supported by crystallographic observation of a non-planar, strained substrate in the S112A:HOPDA complex.

Inhibition of BphD<sub>LB400</sub> by 3-Cl HOPDA was investigated to understand a block in the degradation of polychlorinated biphenyls. BphD<sub>LB400</sub> preferentially hydrolyzed 3-substituted HOPDAs in the order H > F > Cl > Me, indicating that steric bulk impairs catalysis. Kinetic analyses further indicated that large 3-substituents impede formation of

the strained enolate by binding in an alternate conformation, as observed in the S112A:3-Cl HOPDA crystal structure.

Finally, rate-determining hydrolysis of a benzoyl-enzyme was suggested from the observations that: (i) HOPDA and *p*-nitrophenyl benzoate were transformed with similar  $k_{\text{cat}}$  values and (ii) yielded a common product ratio in the presence of methanol.

Overall, the studies demonstrate the importance of an intermediate possessing significant double bond strain in an MCP hydrolase, establish the role of the catalytic His in forming this intermediate, indicate a mechanism of inhibition, and suggest the possibility that hydrolysis may proceed via an acyl-enzyme.

## TABLE OF CONTENTS

|  |             |
|--|-------------|
| <b>ABSTRACT</b> .....  | <b>ii</b>   |
| <b>TABLE OF CONTENTS</b> .....   | <b>iv</b>   |
| <b>LIST OF TABLES</b> .....  | <b>vii</b>  |
| <b>LIST OF FIGURES</b> .....   | <b>viii</b> |
| <b>ABBREVIATIONS</b> .....   | <b>xi</b>   |
| <b>PREFACE</b> .....   | <b>xii</b>  |
| <b>ACKNOWLEDGEMENTS</b> .....  | <b>xiii</b> |
| <br>   |             |
| <b>CHAPTER ONE: INTRODUCTION</b> .....                                       | <b>1</b>    |
| 1.1 Aromatic compounds in nature .....                                       | 1           |
| 1.2 Microbial degradation of aromatic compounds.....                         | 1           |
| 1.3 Microbial <i>meta</i> -cleavage of aromatic compounds.....               | 2           |
| 1.3.1 The biphenyl (Bph) pathway.....  | 2           |
| 1.3.2 The Bph pathway can transform polychlorinated biphenyls (PCBs) .....   | 4           |
| 1.3.2.1 BphD as a determinant of PCB degradation.....                        | 6           |
| 1.4 The MCP hydrolases.....  | 8           |
| 1.4.1 Classification of MCP hydrolases .....                                 | 9           |
| 1.4.2 The $\alpha/\beta$ -hydrolase superfamily.....                         | 13          |
| 1.5 Mechanistic aspects of MCP hydrolase catalysis.....                      | 16          |
| 1.5.1 Nature's strategies for C-C bond hydrolysis.....                       | 16          |
| 1.5.2 The tautomerization reaction.....                                      | 19          |
| 1.5.3 The hydrolytic reaction.....   | 20          |
| 1.6 Structural aspects of MCP hydrolases .....                               | 22          |
| 1.7 Aim of this study .....  | 26          |
| <br>   |             |
| <b>CHAPTER TWO: MATERIALS AND METHODS</b> .....                              | <b>28</b>   |
| 2.1 Chemicals.....   | 28          |
| 2.1.1 Commercially and privately sourced.....                                | 28          |
| 2.1.2 Preparation of 4,4'-difluoro-2,3-dihydroxybiphenyl (4,4'-diF DHB)..... | 28          |
| 2.1.3 Preparation of HOPDAs .....  | 30          |
| 2.2 Mutagenesis, protein production and purification.....                    | 30          |
| 2.3 Protein analysis.....  | 33          |
| 2.4 Steady-state kinetic experiments .....                                   | 33          |
| 2.4.1 Standard spectrophotometric assay .....                                | 33          |
| 2.4.2 Product inhibition .....   | 34          |

|  |           |
|--|-----------|
| 2.4.3 BphD <sub>LB400</sub> -catalyzed HPD ketonization .....                                | 35        |
| 2.5 Stopped-flow kinetic experiments .....   | 35        |
| 2.6 HPLC analysis of coupling .....  | 36        |
| 2.7 Deuterium incorporation .....  | 36        |
| 2.8 HPLC analysis of product ratios from nucleophile partitioning .....                      | 37        |
| <b>CHAPTER THREE: RESULTS .....</b>  | <b>39</b> |
| 3.1 Mechanistic analysis of wild type BphD <sub>LB400</sub> .....                            | 39        |
| 3.1.1 Stopped-flow spectrophotometry .....   | 39        |
| 3.1.2 Coupling of substrate consumption to product formation .....                           | 44        |
| 3.1.3 Deuterium incorporation into HPD .....   | 45        |
| 3.1.4 Product inhibition studies .....   | 48        |
| 3.2 Characterization of BphD <sub>LB400</sub> variants .....                                 | 49        |
| 3.2.1 General kinetic analysis .....   | 49        |
| 3.2.2 Stopped-flow kinetic analysis .....  | 51        |
| 3.2.3 Tautomerization of HPD by variant enzymes .....  | 55        |
| 3.3 The basis for inhibition by 3-Cl HOPDA .....   | 56        |
| 3.3.1 Steady-state kinetics .....  | 56        |
| 3.3.2 Stopped-flow kinetics .....  | 57        |
| 3.4 Characterization of the hydrolysis reaction .....  | 61        |
| 3.4.1 BphD <sub>LB400</sub> catalyzes alcoholysis .....                                      | 61        |
| 3.4.2 Different substrates generate a similar acid:ester product ratio .....                 | 61        |
| 3.4.3 HOPDA and pNPB are hydrolyzed with similar $k_{\text{cat}}$ values .....               | 64        |
| 3.4.4 Steady-state kinetic analysis of nucleophile partitioning for HOPDA .....              | 66        |
| 3.4.5 Detection of possible ‘burst’ kinetics for pNPB .....                                  | 70        |
| <b>CHAPTER FOUR: DISCUSSION .....</b>  | <b>71</b> |
| 4.1 Kinetic features of wild type BphD <sub>LB400</sub> .....                                | 71        |
| 4.1.1 Biphasic kinetics cannot be explained by uncoupling .....                              | 71        |
| 4.1.2 Interpretations of the kinetic data .....  | 72        |
| 4.1.2.1 Mechanism A: Discrete keto-intermediate (general base mechanism) .....               | 72        |
| 4.1.2.2 Mechanism B: Two-conformation model (nucleophilic mechanism) ..                      | 73        |
| 4.2 Behaviour of variant enzymes .....   | 77        |
| 4.2.1 An E:S <sup>red</sup> intermediate was trapped in the S112A variant .....              | 78        |
| 4.2.1.1 The crystal structure of E:S <sup>red</sup> in the S112A:HOPDA complex .....         | 79        |
| 4.2.1.2 Assignment of E:S <sup>red</sup> to a strained enolate, E:S <sup>se</sup> .....      | 80        |
| 4.2.2 H265A variants generate a planar enolate, E:S <sup>c</sup> .....                       | 81        |
| 4.2.2.1 Crystal structure of E:S <sup>c</sup> trapped in the S112A/H265A:HOPDA complex ..... | 82        |
| 4.2.3 Mechanistic insights from enzyme:substrate complexes .....                             | 83        |
| 4.2.3.1 His265-dependent formation of E:S <sup>se</sup> .....                                | 83        |
| 4.2.3.2 Significance of the non-planar conformation of E:S <sup>se</sup> .....               | 85        |

|  |            |
|--|------------|
| 4.2.3.3 Mechanism A: His265 protonates C5.....                 | 87         |
| 4.2.3.4 Mechanism B: Ser112 protonates C5.....                 | 88         |
| 4.2.3.5 Significance of the E:S <sup>c</sup> conformation..... | 90         |
| 4.2.3.6 Active site conformational changes.....                | 91         |
| 4.2.4 Tautomerization of HPD by variant enzymes.....           | 91         |
| 4.3 Basis for inhibition by 3-Cl HOPDA.....                    | 93         |
| 4.4 The mechanism of hydrolysis.....                           | 99         |
| 4.4.1 Evidence for a nucleophilic mechanism.....               | 99         |
| 4.4.2 Evidence for a general base mechanism.....               | 102        |
| 4.5 Overall Mechanism.....                                     | 105        |
| 4.6 Concluding Remarks.....                                    | 107        |
| <br>   |            |
| <b>BIBLIOGRAPHY.....</b>                                       | <b>109</b> |
| <br>   |            |
| <b>APPENDIX I: CRYSTALLOGRAPHIC DATA.....</b>                  | <b>118</b> |
| <br>   |            |
| <b>APPENDIX II: DERIVATIONS OF STEADY-STATE EQUATIONS.....</b> | <b>122</b> |

**LIST OF TABLES**

|  |     |
|--|-----|
| Table 1. Reciprocal relaxation times and amplitudes for single turnover reactions. ....  | 41  |
| Table 2. Kinetic data for BphD <sub>LB400</sub> alanine variants <sup>a</sup> .....  | 55  |
| Table 3. Properties of 3-substituted HOPDAs and the steady-state parameters for their hydrolysis by BphD <sub>LB400</sub> . <sup>a</sup> .....   | 57  |
| Table 4. Reciprocal relaxation times and amplitudes for single turnover reactions monitored by stopped-flow spectrophotometry at the substrate absorption maxima. <sup>a</sup> .....   | 58  |
| Table 5. Experimental steady-state parameters for the BphD <sub>LB400</sub> -catalyzed transformation of HOPDA, compared with values calculated using the equations for either a nucleophilic or general base mechanism, in the presence of varying concentrations of methanol. .... | 69  |
| Table 6. Results of model refinement for BphD variants and complexes. ....   | 120 |
| Table 7. Results of restrained refinements assuming different isomers of HOPDA.....  | 121 |

## LIST OF FIGURES

|   |    |
|---|----|
| Figure 1. Representative aerobic microbial catabolic pathways funnel diverse aromatic compounds to one of four central intermediates: A. catechol; B. cryptic aromatic catabolism via a substituted catechol; C. protocatechuic acid; D. gentisic acid; E. (chloro)hydroxyquinol and (chloro)hydroquinone. .... | 3  |
| Figure 2. The Bph pathway.....  | 4  |
| Figure 3. 3-Cl HOPDAs generated from a range of 4-Cl biphenyls inhibit BphD and therefore block the Bph pathway.....  | 7  |
| Figure 4. Representative reactions catalyzed by MCP hydrolases. See section 1.4.1 for a description of classes. ....  | 8  |
| Figure 5. Dendrogram obtained from alignment of 27 MCP hydrolases. ....   | 10 |
| Figure 6. Structure-based sequence alignment of MCP hydrolases.....   | 11 |
| Figure 7. The “classical” nucleophilic mechanism of serine hydrolases. ....   | 14 |
| Figure 8. Reactions catalyzed by $\alpha/\beta$ -hydrolases.....  | 16 |
| Figure 9. The reaction catalyzed by an esterase (a) is energetically more favourable than the reaction catalyzed by a C-C hydrolase (b).....  | 17 |
| Figure 10. Examples of representative enzymes for each of the three general enzymatic strategies for hydrolytic cleavage of C-C bonds.....  | 18 |
| Figure 11. The role of the catalytic serine in MCP hydrolases proposed in reference (104).....  | 22 |
| Figure 12. The structure of the BphD <sub>LB400</sub> monomer illustrates the lid domain (ochre, top) and the core domain (grey) of the $\alpha/\beta$ -hydrolase fold. ....  | 24 |
| Figure 13. The structure of HPD in the active site of an S112C variant of BphD <sub>LB400</sub> ....  | 25 |
| Figure 14. A representative stopped-flow experiment illustrating a single turnover of HOPDA (4 $\mu$ M) by BphD <sub>LB400</sub> (8 $\mu$ M).....   | 40 |
| Figure 15. A kinetic model involving release of the keto-intermediate. ....   | 44 |
| Figure 16. The <sup>1</sup> H NMR spectrum of HPD generated from BphD <sub>LB400</sub> -catalyzed hydrolysis of HOPDA.....  | 47 |

|  |    |
|--|----|
| Figure 17. Cornish-Bowden plots illustrating the type of inhibition of the BphD <sub>LB400</sub> -catalyzed hydrolysis of HOPDA by reaction products. ....   | 49 |
| Figure 18. Absorption spectra of intermediates arising during the hydrolysis of HOPDA by BphD <sub>LB400</sub> variants. ....  | 54 |
| Figure 19. The catalytic triad residue His265 of BphD <sub>LB400</sub> is required for HPD tautomerization. ....   | 56 |
| Figure 20. Time-resolved spectra from single turnover ( $E = 8 \mu\text{M}$ ; $S = 4 \mu\text{M}$ ) stopped-flow spectrophotometry show that increasing the size of the HOPDA 3-substituent limits accumulation of the high wavelength-absorbing $E:S^{\text{red}}$ intermediate. .... | 59 |
| Figure 21. HPLC chromatograms of BphD <sub>LB400</sub> -catalyzed hydrolysis of HOPDA (50 $\mu\text{M}$ ) in the presence of 1% (v/v) methanol, ethanol, or <i>n</i> -propanol. ....   | 62 |
| Figure 22. HPLC chromatograms illustrating the products of BphD <sub>LB400</sub> -catalyzed conversion of pNPB and HOPDA in the presence of methanol. ....   | 64 |
| Figure 23. Steady-state hydrolysis of pNPB by BphD <sub>LB400</sub> . ....   | 65 |
| Figure 24. Kinetic schemes and steady-state expressions for A) nucleophilic and B) general base mechanisms of BphD <sub>LB400</sub> . ....   | 67 |
| Figure 25. The dependence of $k_{\text{cat}}$ on methanol concentration for the BphD <sub>LB400</sub> -catalyzed degradation of HOPDA. ....  | 68 |
| Figure 26. A multiple turnover stopped-flow experiment observing a burst of pNP formation upon mixing 1 $\mu\text{M}$ BphD <sub>LB400</sub> with 4 $\mu\text{M}$ pNPB (0.1 M potassium phosphate, pH 7.5, 25 °C). ....   | 70 |
| Figure 27. Mechanism A: a mechanism involving reversible ketonization and single step hydrolysis via a <i>gem</i> -diol intermediate. ....   | 73 |
| Figure 28. Model B: A two-conformation kinetic model accounting for biphasic decay of $ES^{\text{red}}$ . ....   | 74 |
| Figure 29. The BphD <sub>LB400</sub> tetramer. ....  | 77 |
| Figure 30. Different forms of HOPDA that were examined as possible interpretations of the S112A:HOPDA crystallographic data. ....  | 79 |
| Figure 31. Crystal structure of the S112A:HOPDA complex illustrating the $E:S^{\text{red}}$ intermediate as a strained enolate. ....   | 80 |

|   |     |
|---|-----|
| Figure 32. Crystal structures of the S112A:HOPDA complex (E:S <sup>sc</sup> , orange carbon atoms) overlaid with the S112A/H265A:HOPDA complex (E:S <sup>c</sup> , yellow carbon atoms, PDB code 2PUJ).....   | 83  |
| Figure 33. Proposed substrate conformational change upon formation of the E:S <sup>sc</sup> intermediate.....   | 85  |
| Figure 34. Stereochemical course of BphD.....   | 87  |
| Figure 35. Mechanism A: His265-mediated tautomerization and hydrolysis via a <i>gem</i> -diolate intermediate.....  | 88  |
| Figure 36. Mechanism B: C5 protonation by Ser112 and hydrolysis via nucleophilic catalysis.....   | 89  |
| Figure 37. Proposed effects of BphD mutations on HPD tautomerization.....   | 92  |
| Figure 38. Possible kinetic schemes for BphD <sub>LB400</sub> -catalyzed hydrolysis of 3,10-diF HOPDA.....  | 94  |
| Figure 39. Stereo view of superposed active sites of S112A:3-Cl HOPDA and S112A:HOPDA.....  | 95  |
| Figure 40. The hydrophobic chlorine-binding pocket of the S112A:3-Cl HOPDA complex.....   | 96  |
| Figure 41. The proposed effect of 3-substituent size on E:S <sup>sc</sup> formation. H.P. = hydrophobic pocket.....   | 98  |
| Figure 42. Partitioning between methanol and water may distinguish hydrolytic mechanisms.....   | 102 |
| Figure 43. Possible mechanisms of BphD <sub>LB400</sub> .....   | 107 |
| Figure 44. Enzyme:substrate interactions in the BphD-S112A:HOPDA complex.....   | 118 |
| Figure 45. Stereo view showing: the refined model of S112A:3-Cl HOPDA complex; the (2F <sub>o</sub> -F <sub>c</sub> ) electron density (cyan, contour level = 1σ) of the refined structure; and the (F <sub>o</sub> -F <sub>c</sub> ) electron density before 3-Cl HOPDA was added to the model (blue, contour level = 3σ)..... | 119 |

**ABBREVIATIONS**

|          |  |
|----------|--|
| ADP      | adenosine diphosphate                                      |
| BPDO     | biphenyl dioxygenase (EC 1.14.12.18)                       |
| C23O     | catechol 2,3-dioxygenase (EC 1.13.11.2)                    |
| CHES     | 2-( <i>N</i> -cyclohexylamino)ethane sulfonic acid         |
| DHB      | 2,3-dihydroxybiphenyl                                      |
| DHBD     | 2,3-dihydroxybiphenyl 1,2-dioxygenase (EC 1.13.11.39)      |
| DHPON    | 2,6-dihydroxy- <i>pseudo</i> -oxynicotine                  |
| DTT      | dithiothreitol   |
| HEPES    | 4-(2-hydroxyethyl)-1-piperazineethanesulfonic acid         |
| HOPDA    | 2-hydroxy-6-oxo-6-phenylhexa-2,4-dienoic acid              |
| HPD      | 2-hydroxypenta-2,4-dienoic acid                            |
| HPLC     | high performance liquid chromatography                     |
| MCP      | <i>meta</i> -cleavage product                              |
| NADH     | $\beta$ -nicotinamide adenine dinucleotide, reduced        |
| NMR      | nuclear magnetic resonance                                 |
| PCB      | polychlorinated biphenyl                                   |
| PLP      | pyridoxal-5'-phosphate                                     |
| pNP      | <i>p</i> -nitrophenol                                      |
| pNPB     | <i>p</i> -nitrophenyl benzoate                             |
| SDS-PAGE | sodium dodecyl sulphate polyacrylamide gel electrophoresis |
| WT       | wild type  |

## PREFACE

Parts of this thesis have been published in refereed journals. Characterization of wild type BphD<sub>LB400</sub> appeared in *Biochemistry* (Horsman, G.P.\*; Ke, J.\*; Dai, S.; Seah, S.Y.K.; Bolin, J.T.; Eltis, L.D. “Kinetic and structural insight into the mechanism of BphD, a C-C bond hydrolase from the biphenyl degradation pathway” *Biochemistry* **2006**, *45*, 11071-11086 (\*shared first authorship)). In this publication, I was responsible for the kinetic, HPLC, and NMR analyses.

Characterization of BphD<sub>LB400</sub> variants appeared in the *Journal of Biological Chemistry* (Horsman, G.P.\*; Bhowmik, S.\*; Seah, S.Y.K.; Kumar, P.; Bolin, J.T.; Eltis, L.D. “The tautomeric half-reaction of BphD, a C-C bond hydrolase: kinetic and structural evidence supporting a key role for histidine 265 of the catalytic triad” *J. Biol. Chem.* **2007**, *282*, 19894-19904 (\*shared first authorship)). I was responsible for the kinetic aspects of this work.

The effect of 3-substituted HOPDAs on BphD<sub>LB400</sub> appeared in the *Journal of Biological Chemistry* (Bhowmik, S.\*; Horsman, G.P.\*; Bolin, J.T.; Eltis, L.D. “The molecular basis for inhibition of BphD, a C-C bond hydrolase involved in PCB degradation: large 3-substituents prevent tautomerization” *J. Biol. Chem.* **2007**, *282*, 36377-36385 (\*shared first authorship)). I was responsible for the kinetic aspects of this study.

Crystal structures were determined by the group of Jeffrey T. Bolin (Purdue University), and are therefore presented only in the Introduction and Discussion sections of this thesis.

## ACKNOWLEDGEMENTS

I would like to thank my supervisor Lindsay Eltis, for his patience, excellent guidance, and support.

I also acknowledge the past and present Eltis lab members Christine Florizone, Pascal Fortin, Yong Ge, Leticia Gómez Gil, Thomas Heuser, Carly Huitema, Jie Liu, Louis Luk, Sachi Okamoto, Fred Vaillancourt, Cheryl Whiting, Katherine Yam, and Mark Yang for all their help. Thanks also to Mark Okon for assistance acquiring NMR data, and to Sally Rocks (University of Rochester) for the NMR data for 4,4'-diF DHB.

Thank you to my committee members, Lawrence McIntosh and Martin Tanner, for your guidance, helpful suggestions, and for reviewing this thesis.

Many thanks to Shiva Bhowmik, Jiyuan Ke, and Jeffrey Bolin for providing crystal structures. This project greatly benefited from your contributions. I would also like to thank Victor Snieckus for providing the precursors to the substrates used in this study.

I would also like to thank family and friends for their support and friendship. And of course, thank you Becky for your kind encouragement, understanding, and support.

## Chapter One: INTRODUCTION

### 1.1 Aromatic compounds in nature

Aromatic compounds, such as benzene, are planar cyclic molecules containing a fully conjugated system that obeys Hückel's rule (1). The resulting resonance has been estimated to impart an extra  $\sim 150$  kJ/mol of stability to benzene, relative to the sum of three isolated double bonds of cyclohexene (2). The ubiquity of aromatic compounds in nature is exemplified by lignin, a heterogeneous polymer of phenolic compounds that constitutes 18 – 35% of the dry weight of plant woody tissues (3), making it one of the most abundant polymers on Earth. Considering that an estimated  $1.5 \times 10^{10}$  tons of atmospheric carbon is annually sequestered into lignin, microbial enzymes that degrade aromatic compounds clearly play a critical role in maintaining the carbon cycle (3).

### 1.2 Microbial degradation of aromatic compounds

Microorganisms use a variety of aerobic and anaerobic strategies to degrade aromatic compounds. In spite of this catabolic diversity, all known pathways employ a common catalytic logic of ring activation and subsequent cleavage. Anaerobically, ring activation of benzene yields key intermediates such as benzoyl-CoA, resorcinol, phloroglucinol, and hydroxyhydroquinone, which may then undergo reductive dearomatization (4, 5). Aerobic microbial degradation uses oxygenases for both activation and ring cleavage, although the latter may occur hydrolytically in hybrid aryl-CoA pathways (6-8). Oxygenases such as Rieske non-heme iron oxygenases activate the aromatic ring by incorporating oxygen-containing substituents (9, 10) to generate 1,2-dihydroxylated aromatic metabolites such as catechols, or 1,4-dihydroxylated aromatics

such as gentisates and hydroquinones. Ring-cleaving dioxygenases open the substituted aromatic ring in either an extradiol (*meta*-cleavage) or intradiol (*ortho*-cleavage) fashion, defined according to the location of the broken C-C bond in relation to the hydroxyl groups (11, 12). Examples of this aerobic degradation strategy are summarized in Figure 1, which illustrates how a wide variety of aromatic compounds are transformed to central intermediates via a relatively limited number of dihydroxylated metabolites.

### 1.3 Microbial *meta*-cleavage of aromatic compounds

Although microbes use a variety of aerobic pathways to degrade aromatic compounds, the biphenyl (Bph) pathway (section 1.3.1) exemplifies the catalytic logic of *meta*-cleavage, whereby a catechol ring is opened in an extradiol (or *meta*) fashion to afford a *meta*-cleavage product (MCP). The latter is cleaved by an MCP hydrolase to yield a 2-hydroxydienoic acid and a carboxylic acid. The dienoate is further metabolized to pyruvate and acetaldehyde, which may enter the tricarboxylic acid cycle as acetyl-CoA (3).

#### 1.3.1 The biphenyl (Bph) pathway

The upper Bph pathway (Figure 2) consists of four sequentially acting Bph enzymes. Biphenyl degradation is initiated by biphenyl dioxygenase (BPDO), a Rieske-type enzyme consisting of an oxygenase, ferredoxin, and ferridoxin reductase (9). The latter two proteins facilitate electron transport from NADH to the mononuclear iron center of the oxygenase, where addition of O<sub>2</sub> to biphenyl produces *cis*-2,3-dihydro-2,3-dihydroxybiphenyl. A reductase, BphB, catalyzes NAD<sup>+</sup>-dependent dehydrogenation of the *cis*-diol to generate the catecholic intermediate, 2,3-dihydroxybiphenyl (DHB), which undergoes BphC-catalyzed *meta*-cleavage to yield 2-hydroxy-6-oxo-6-phenylhexa-2,4-

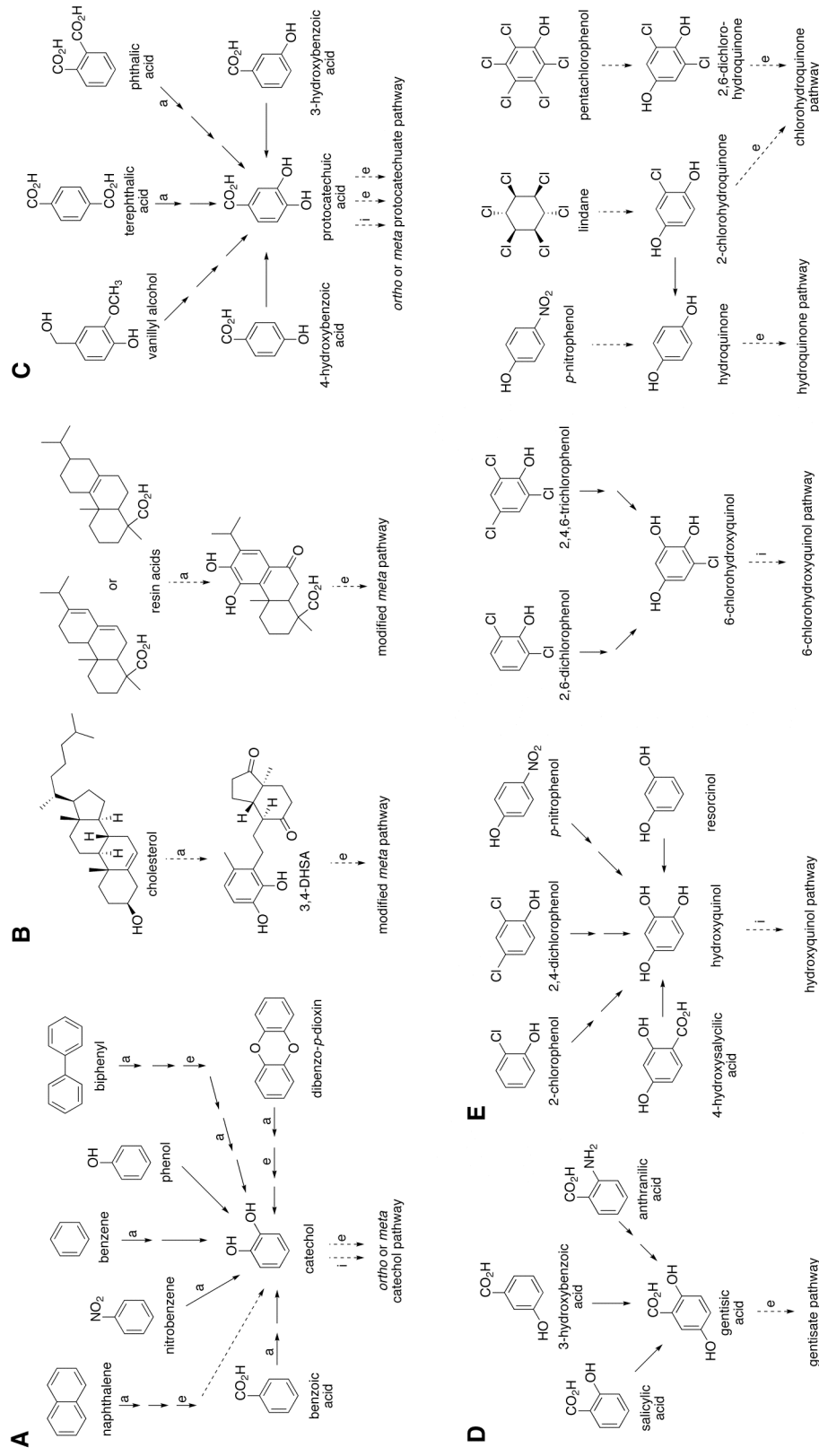


**Figure 1.** Representative aerobic microbial catabolic pathways funnel diverse aromatic compounds to one of four central intermediates: A. catechol; B. cryptic aromatic catabolism via a substituted catechol; C. protocatechuic acid; D. gentisic acid; E. (chloro)hydroxyquinol and (chloro)hydroquinone. All pathways employ oxygenases to incorporate oxygen for both activation and subsequent cleavage of the aromatic ring. Solid arrows indicate a single enzymatic reaction, while dotted arrows represent multiple steps. Letter labels designate catalysis via the following enzymes: “a” = Reiske non-heme iron oxygenase; “i” = intradiol dioxygenase; “e” = extradiol dioxygenase. Adapted from (11).

dienoic acid (HOPDA). Finally, HOPDA is degraded by an MCP hydrolase, BphD, which adds water across a C-C bond to afford 2-hydroxypenta-2,4-dienoate (HPD) and benzoic acid.

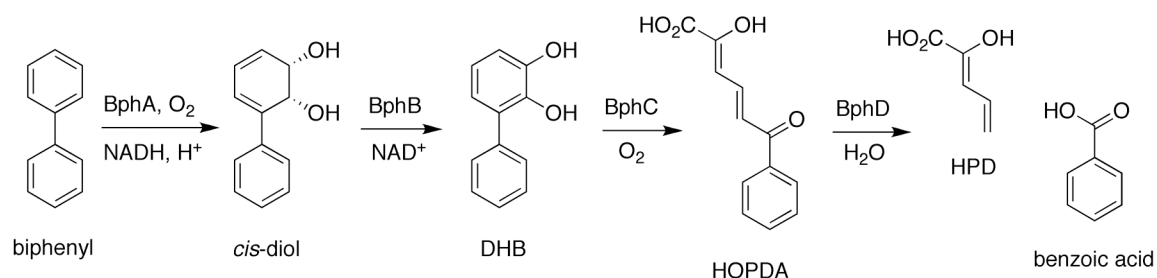


**Figure 2.** The Bph pathway.

### 1.3.2 The Bph pathway can transform polychlorinated biphenyls (PCBs)

PCBs are produced by chlorination of biphenyl to generate commercial mixtures that typically contained 20-60 (mostly tri-hexachlorinated) of the 209 possible congeners. These non-flammable, chemically stable, non-volatile, and electrical insulating compounds were used extensively for applications such as heat transfer, hydraulics, plasticizers, and in the dielectric fluid of transformers (13). About  $2 \times 10^9$  kg of PCBs were produced from the late 1920s until production was banned in the 1970s due to concerns over toxicity (14). Indeed, subsequent investigations have linked PCBs to cancer (15, 16), childhood neurodevelopmental deficits resulting from prenatal exposure (17-19), and a host of other effects attributed to endocrine disruption (20-22).

Unfortunately, the industrially useful stability of PCBs is the very property that ensures their persistence in the environment. As a result of spills and poor waste disposal methods, it has been estimated that  $2 \times 10^8$  kg remain in “mobile environmental reservoirs” (14). Moreover, these lipophilic compounds tend to accumulate in higher trophic organisms (14). The effects in aquatic environments are of particular concern

(23), prompting reviews of human fish consumption practices (24, 25). However, removing PCBs from the environment is challenging and costly. For instance, the remediation of military radar stations in the Canadian Arctic typically involves excavation and shipment of heavily contaminated soil to PCB treatment facilities in the south (26).

The discovery that the Bph pathway can transform many PCBs has fuelled interest in using microbes as an alternative means of remediating contaminated sites (27). Although the range of congeners degraded is highly strain-dependent and most strains degrade only lightly chlorinated biphenyls, some good PCB-degraders have been isolated (28-31). For example, one of the best degraders, *Burkholderia xenovorans* LB400, was isolated from a PCB-contaminated site and can transform up to hexachlorinated congeners (28, 29, 32-35). However, even LB400 is unable to transform or effectively mineralize many congeners.

Optimizing microbial catabolic activities for PCB biodegradation requires characterization of the catalytic abilities of Bph enzymes to transform chlorinated substrates. To this end, the first pathway enzyme, BPDO, has been most intensely studied, and the spectrum of congeners degraded by a given strain is governed to a large extent by the substrate specificity of this enzyme (27). Indeed, sequence-specificity data from divergent BPDOs was used to guide protein engineering efforts that yielded variants with improved activity towards certain congeners (36-38). However, even if the initial transformation occurs, the resulting metabolites may block downstream enzymes. For instance, the strong inhibition of BphC by 2',6'-diCl DHB represents a bottleneck in the Bph pathway (39). Similarly, 2,2',5,5'-tetraCl biphenyl is transformed by LB400 to the corresponding 3,4-dihydroxybiphenyl dead-end metabolite, for which a degrading

enzyme has recently been engineered (40).

### 1.3.2.1 BphD as a determinant of PCB degradation

The final enzyme in the pathway, BphD, has also been implicated as a key determinant of PCB degradation. It was initially observed that HOPDAs accumulate when microbial strains are incubated with certain PCB congeners (30). Subsequent analysis of the substrate specificity of BphD from *B. xenovorans* LB400 (BphD<sub>LB400</sub>) revealed that dienoate-substituted monochlorinated HOPDAs (3-, 4-, and 5-Cl HOPDAs) are poor substrates, but chlorine substituents on the phenyl ring have little effect on catalysis (41). Specifically, 5-chlorination reduced the maximal rate for HOPDA hydrolysis by BphD<sub>LB400</sub> by 3-fold, and chlorination at the 3 or 4 positions reduced the maximal rate by  $\sim 10^3$  and  $\sim 10^4$ -fold, respectively.

Although 4-Cl HOPDA is the least efficiently transformed monochlorinated HOPDA, 3-Cl HOPDAs probably represent a more significant roadblock to PCB biodegradation. Firstly, 3-Cl HOPDA ( $t_{1/2} \sim 500$  h) is more stable than 4-Cl HOPDA, which undergoes a non-enzymatic transformation to 4-OH HOPDA ( $t_{1/2} = 2.8$  h) followed by degradation to products including acetophenone ( $t_{1/2} \sim 180$  h) (41). Moreover, BphD<sub>LB400</sub> is more potently inhibited by 3-Cl HOPDA ( $K_{ic} = 0.57$   $\mu$ M) than 4-Cl HOPDA ( $K_{ic} = 3.6$   $\mu$ M) or 4-OH HOPDA ( $K_{ic} = 0.95$   $\mu$ M) (41). The high stability of 3-Cl HOPDA together with its relatively strong inhibition of BphD<sub>LB400</sub> suggests that 3-Cl HOPDAs can block the Bph pathway and hence the mineralization of all PCB congeners. This is consistent with the observation that HOPDAs accumulated when congeners such as 4,4'-diCl, 2,4,4'-triCl, and 2,4',5-triCl biphenyls were incubated with several strains, including LB400 (28, 30, 31). This further implicates 3-Cl HOPDAs in PCB degradation because these congeners are predicted to generate 3,10-diCl, 3,8,10-triCl, and 3,8,11-triCl

HOPDA, respectively (Figure 3). Notably, 3-Cl HOPDA itself is not expected to occur *in vivo* because BphA<sub>LB400</sub> preferentially dihydroxylates the non-chlorinated ring of 4-Cl biphenyl (31). However, the physiologically relevant substrate 3,9,11-triCl-HOPDA exhibits similar steady-state kinetic behaviour to 3-Cl HOPDA (42), confirming the utility of the latter for studying BphD inhibition.

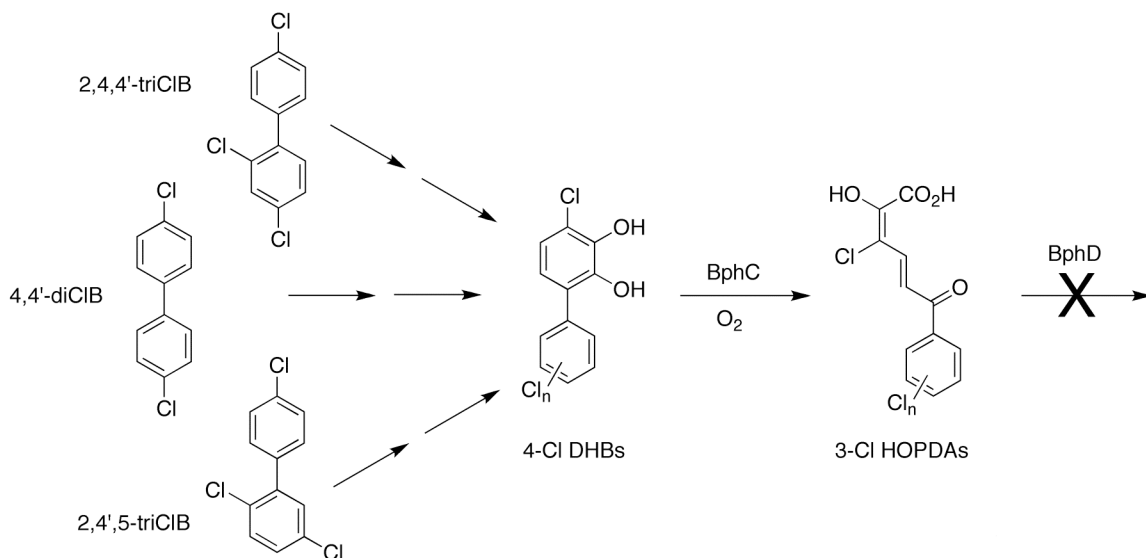


**Figure 3.** 3-Cl HOPDAs generated from a range of 4-Cl biphenyls inhibit BphD and therefore block the Bph pathway.

Recent studies suggest that the inhibition of BphD by 3-Cl HOPDAs may be overcome. For instance, divergent MCP hydrolases BphD<sub>LB400</sub>, BphD from *Rhodococcus globerulus* P6 (BphD<sub>P6</sub>) and DxnB2 from *Sphingomonas wittichii* RW1 (DxnB2<sub>RW1</sub>) exhibit different specificities for chlorinated HOPDAs (42, 43). Most significantly, DxnB2<sub>RW1</sub> has ~13-fold higher specificity for 3-Cl HOPDA than BphD<sub>LB400</sub> (42). Secondly, 3-Cl and 5-Cl HOPDAs are dehalogenated, albeit with relatively low specificities, by BphK, a glutathione-*S*-transferase present in the *bph* gene cluster of some organisms (44). However, it is not yet clear if PCB-degrading capabilities are enhanced in strains containing BphK.

## 1.4 The MCP hydrolases

BphD belongs to a family of enzymes that catalyze carbon-carbon bond hydrolysis of the products arising from the *meta*-cleavage of catechols. While these so-called MCP hydrolases have been identified in catabolic pathways that degrade a wide variety of aromatic compounds, all MCPs share a common 2,6-dioxo-2,4-dienoate core (Figure 4). Because the *meta*-cleavage pathways have been studied primarily with a view to harnessing the catabolic potential of soil bacteria for degrading pollutants, most characterized MCP hydrolases reflect this bias, transforming MCPs from the degradation of aromatics such as biphenyl, carbazole, dibenzofuran, and xylenes. However, genes encoding *meta*-cleavage pathway enzymes were recently shown to be critical for survival of *Mycobacterium tuberculosis*, the causative agent of tuberculosis, in the macrophage (45). Originally annotated as *bph* genes, they are now known to encode cholesterol catabolism (46). This new finding further motivates studies of the mechanisms of catalysis and inhibition of MCP hydrolases.

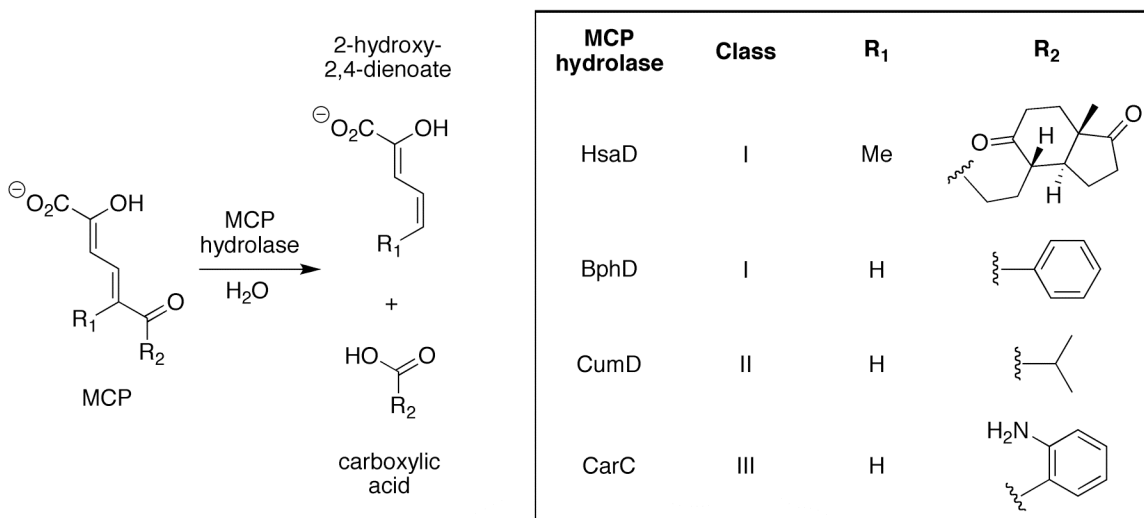


**Figure 4.** Representative reactions catalyzed by MCP hydrolases. See section 1.4.1 for a description of classes.

### 1.4.1 Classification of MCP hydrolases

Phylogenetic analysis of sequence alignments performed using structural information (section 1.6) identified at least three major classes of MCP hydrolases (42) (Figure 5). This classification is generally consistent with substrate specificity, and representative substrates of each class are shown in Figure 4. Class I enzymes are involved primarily in the degradation of biphenyl and steroids, although the well-characterized hydrolase MhpC from the phenylpropionate pathway of *E. coli* is also included (47). The tightly clustered class II enzymes hydrolyze alkylbenzene-derived MCPs containing uncharged alkyl substituents at C6. Class III enzymes were recently identified to be involved in the hydrolysis of *ortho*-substituted HOPDAs arising from the angular dioxygenation of compounds such as dibenzofuran and carbazole (42).

Sequence alignments also identify unique features of the MCP hydrolases (Figure 6). For instance, Gly43, Asn51, Ser112, Asn111, Asp237, Arg190, His265, and Trp266 (BphD<sub>LB400</sub> numbering) are strictly conserved across all classes. When the alignment is extended beyond the MCP hydrolase family to include enzymes with high sequence similarity, other features become evident. For example, Gly43, Asn51, Asn111, Arg190, and Trp266 appear to be unique to the MCP hydrolases. The remaining residues – Ser112, Asp237, His265 – typically constitute the catalytic triad of hydrolytic enzymes such as esterases and proteases. Moreover, the consensus sequence Gly-X-Ser-X-Gly containing Ser112 suggests the MCP hydrolases are members of the  $\alpha/\beta$ -hydrolase superfamily (section 1.4.2).

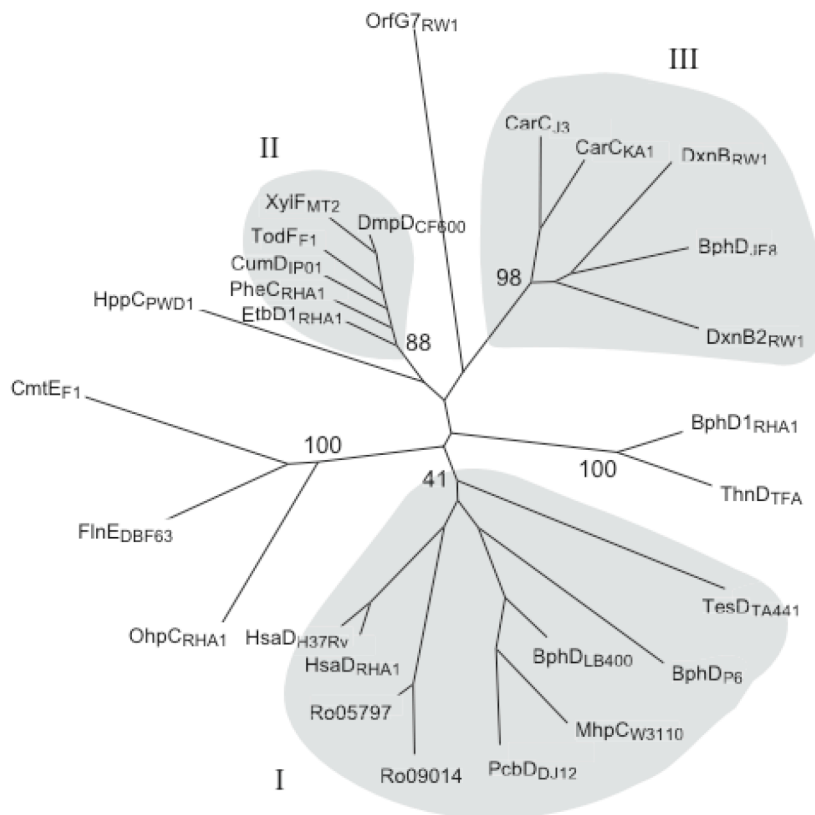


**Figure 5.** Dendrogram obtained from alignment of 27 MCP hydrolases. The sequences not in Figure 6 are as follows (with Genbank accession numbers in parentheses): CarC<sub>KA1</sub>, CarC from *Sphingomonas* sp. KA1 (BAC56762); BphD<sub>JF8</sub>, BphD from *Bacillus* sp. JF8 (BAC79225); BphD<sub>P6</sub>, BphD from *Rhodococcus globerulus* P6 (AAB17100); TodF<sub>F1</sub>, TodF from *Pseudomonas putida* F1 (P23133); XylF<sub>MT2</sub>, XylF from *Pseudomonas putida* MT2 (CAC86804); DmpD<sub>CF600</sub>, DmpD from *Pseudomonas* sp. CF600 (P19076); PheC<sub>RHA1</sub>, EtbD1<sub>RHA1</sub>, HsaD<sub>RHA1</sub>, ro05797<sub>RHA1</sub>, ro09014<sub>RHA1</sub>, OhpC<sub>RHA1</sub>, MCP hydrolases from *Rhodococcus* sp. RHA1 (ABG99128, BAA31163, BAA98136, ABG97574, ABH00058, ABG92355); ThnD<sub>TFA</sub>, ThnD from *Sphingopyxis macrogoltabida* TFA (AAG18490); HppC<sub>PWD1</sub>, HppC from *R. globerulus* PWD1 (AAB81313); TesD<sub>TA441</sub>, TesD from *Pandoraea pnomenusa* TA441 (BAC67693); PcbD<sub>DJ12</sub>, PcbD from *Pseudomonas* sp. DJ12 (BAA07955); CmtE<sub>F1</sub>, CmtE from *Pseudomonas putida* F1 (BAB17778); FlnE<sub>DBF63</sub>, FlnE from *Terrabacter* sp. DBF63 (BAE45094); OrfG7<sub>RW1</sub>, putative hydrolase from *S. wittichii* RW1 (CAA11193). Taken from (42).

**Figure 6.** Structure-based sequence alignment of MCP hydrolases. Sequences are grouped according to class (see Figure 5). Class III: DxnB2\_RW1, DxnB2<sub>RW1</sub> from *S. wittichii* RW1 (DQ975235); DxnB\_RW1, DxnB<sub>RW1</sub> from *S. wittichii* RW1 (CAA51367); and CarC\_J3, CarC<sub>J3</sub> from *Janthinobacterium* sp. strain J3 (BAC56745). Class I: BphD\_LB400, BphD<sub>LB400</sub> from *B. xenovorans* LB400 (P47229); MhpC\_W3110, MhpC<sub>W3110</sub> from *E. coli* W3110 (BAA13054); and HsaD\_H37Rv, HsaD<sub>H37Rv</sub> from *M. tuberculosis* H37Rv (NP\_218086); Class II: CumD\_IP01, CumD<sub>IP01</sub> from *Pseudomonas fluorescens* IP01 (BAA12150). BphD1\_RHA1, BphD<sub>RHA1</sub> from *Rhodococcus* sp. strain RHA1 (BAC92715). CarC<sub>J3</sub>, BphD<sub>LB400</sub>, MhpC<sub>W3110</sub>, CumD<sub>IP01</sub>, and BphD<sub>RHA1</sub> have known structures. Conserved residues are shaded gray. Catalytic triad residues (Ser112, His265 and Asp237 in BphD<sub>LB400</sub>) are white on a black background. Open arrowheads denote oxyanion hole residues. Filled arrowheads indicate NP sub-site residues (see section 1.6 for description), which interact with the substrate's R<sub>2</sub> substituent (Figure 4). The secondary structure for CarC<sub>J3</sub> is noted underneath the alignment with black and light gray representing the core domain and lid domain, respectively. Genbank accession numbers are provided in parentheses. Taken from (42).



### 1.4.2 The $\alpha/\beta$ -hydrolase superfamily

In the early 1990s, crystal structures of several apparently unrelated hydrolytic enzymes revealed a common fold consisting of a mostly parallel  $\alpha/\beta$  structure, characterized by a highly twisted  $\beta$ -sheet (48). This so-called  $\alpha/\beta$ -hydrolase fold has since been recognized as a feature of a large family of proteins performing a wide variety of functions (49-52). Such functional diversity may be a consequence of the structural plasticity of the fold, which tolerates large loop insertions to yield proteins ranging from 19 – 65 kDa (51, 53). Foremost among these insertions is a “lid” domain that often serves to define the properties and accessibility of the substrate-binding site. The functional contribution of the lid domain is exemplified by the interfacial activation of lipases, whereby the lid domain must open to generate a catalytically active enzyme at a lipid-water interface (51, 54).

All  $\alpha/\beta$ -hydrolases contain a nucleophile-His-acid catalytic triad reminiscent of the serine proteases. In the “classical” hydrolytic mechanism (Figure 7) of the proteases (55, 56), the acid-His dyad activates the nucleophile to attack the substrate carbonyl, generating a tetrahedral oxyanion intermediate stabilized by hydrogen bonding from the “oxyanion hole” residues. Collapse of the tetrahedral intermediate generates an acyl-enzyme, and His-mediated hydrolysis liberates the acid via a second tetrahedral intermediate. In contrast to the conserved Ser-His-Asp triad of the trypsin and subtilisin proteases, only the His is invariant in the  $\alpha/\beta$ -hydrolases: Ser, Cys, or Asp may be nucleophiles, and the acidic residue may be Asp, Glu, or as recently discovered in enterobactin hydrolase, completely absent (57). Moreover, comparison of the spatial arrangement of the catalytic triad and oxyanion hole reveals a mirror image relationship between the  $\alpha/\beta$ -hydrolase and serine protease families (48).

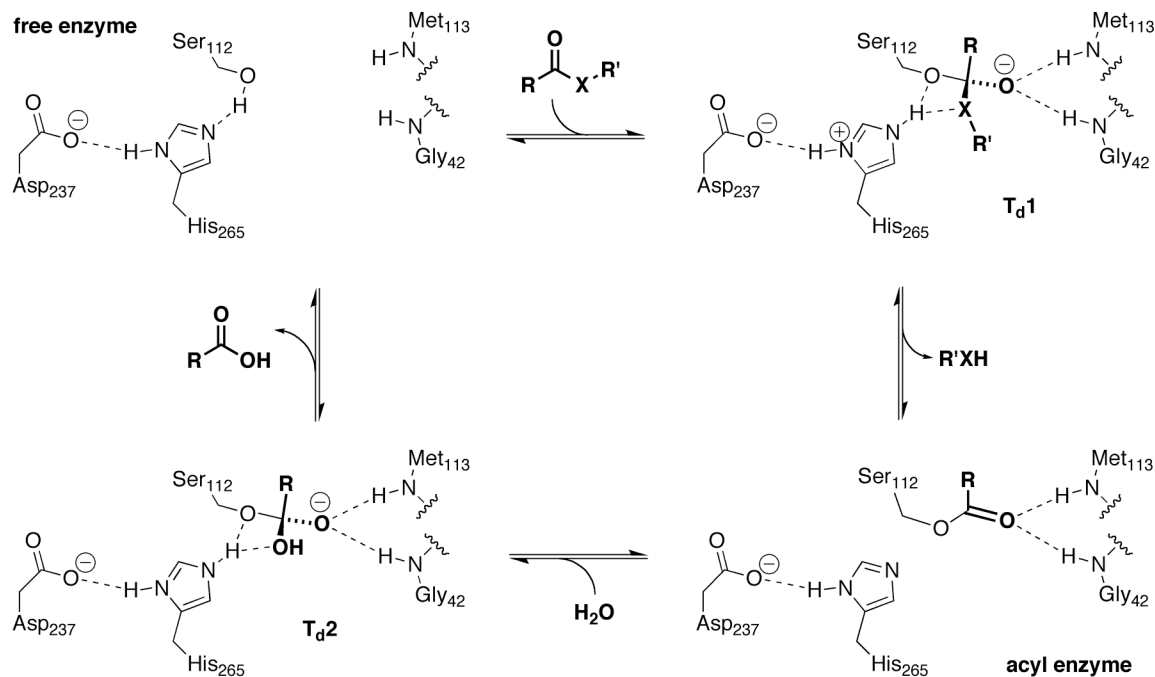


**Figure 7.** The “classical” nucleophilic mechanism of serine hydrolases. Possible substrates include peptides (X = NH), esters (X = O), and thioesters (X = S). Residue numbering corresponds to BphD<sub>LB400</sub>. Adapted from (58).

Because the nucleophilic mechanism has been well-established in the serine proteases (55, 56), the catalytic triad is thought to function similarly in the  $\alpha/\beta$ -hydrolases. Early work demonstrated acylation with highly reactive substrates such as *p*-nitrophenyl acetate in porcine pancreatic lipase (59) and cutinase (60). Less reactive, natural substrates have since been shown to acylate acetylcholinesterase (61), LuxD thioesterase (62) and homoserine transacetylase (63). Such findings support the generality of nucleophilic catalysis in hydrolytic reactions by members of the  $\alpha/\beta$ -hydrolase family.

Additional features of the  $\alpha/\beta$ -hydrolase fold suggest it is suited to nucleophilic catalysis. The nucleophilic residue is embedded in a Sm-X<sub>1</sub>-Nu-X<sub>2</sub>-Sm consensus sequence, where Sm is a small residue (usually Gly), X is any residue, and Nu is the nucleophile. As a structural consequence of the sequence, the nucleophilic residue is at

the tip of a tight turn called the nucleophilic elbow. The geometry of the elbow effectively presents the nucleophile for attack of the substrate, and positions the main chain amide of the following residue in the oxyanion hole.

The structural plasticity of the  $\alpha/\beta$ -hydrolase fold is mirrored by a vast functional diversity, which is documented in the ESTHER database (64). In addition to catalysis, family members have been implicated in non-catalytic roles such as hormone precursors (65), virulence factors (66), pathogenic proteins (67), adhesion proteins (68), and a regulatory factor involved in T cell activation (69).

Catalytic diversity within the family is largely dependent upon the nucleophilic elbow. Indeed, most enzymes employ nucleophilic catalysis via a covalent intermediate (Figure 7) to effect hydrolysis or acyl transfer involving the bond between a heteroatom and a carbonyl carbon (Figure 8a-d,f,g). Such enzymes include acetylcholine esterase (70), thioesterase (71), carboxypeptidase (72), perhydrolase (73), lactamase (74), mycolyl transferase (75), and homoserine transacetylase (63). The catalytic nucleophile also effects dehalogenation (76, 77) and epoxide opening (78).

In contrast, a nucleophilic mechanism does not appear to operate in the three types of  $\alpha/\beta$ -hydrolases that break carbon-carbon bonds (Figure 8e,j): hydroxynitrile lyases, cofactor-less 2,4-dioxygenases, and C-C hydrolases (including MCP hydrolases). Crystal structures of hydroxynitrile lyase suggest that the “nucleophilic” serine deprotonates the cyanohydrin hydroxyl to promote C-C cleavage (79, 80). In the cofactor-less 2,4-dioxygenases (81), 8% of activity is retained without the catalytic triad serine residue (82, 83), suggesting the reaction proceeds via general-base catalysis involving the catalytic histidine (84). Finally, the MCP hydrolases are also not believed to use nucleophilic catalysis (see section 1.5.3).

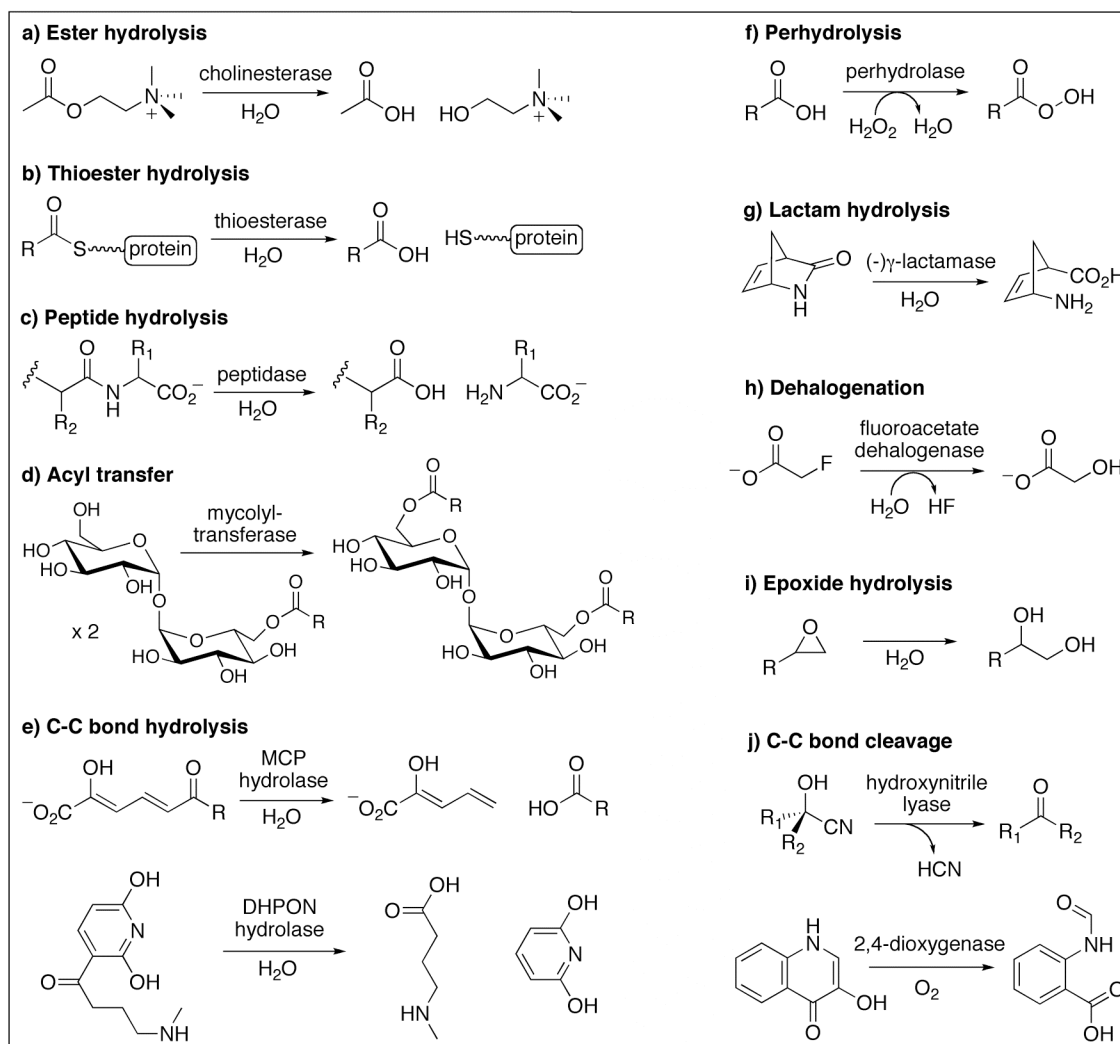


**Figure 8.** Reactions catalyzed by  $\alpha/\beta$ -hydrolases. Adapted from (51).

## 1.5 Mechanistic aspects of MCP hydrolase catalysis

### 1.5.1 Nature's strategies for C-C bond hydrolysis

The MCP hydrolases catalyze the relatively unusual hydrolysis of a carbon-carbon bond. Most known hydrolases act on carbon-heteroatom bonds by direct protonation of the leaving heteroatom, thereby generating a positively charged electron sink. Because

the neutral leaving group is less basic than the nucleophile, its expulsion is energetically favourable (85) (Figure 9a). In contrast, a C-C hydrolase reaction cannot access such an electron sink because the leaving carbon cannot be protonated (Figure 9b). The resulting carbanion is highly unstable unless the charge is delocalized. Indeed, a formidable energetic barrier of  $\sim 200$  kJ/mol can be estimated from the difference in conjugate acid  $pK_a$  values for the attacking hydroxide nucleophile ( $pK_a = 15.7$ ) and the departing carbanion ( $pK_a \sim 50$ ) (85, 86). Because the typical barrier for an MCP hydrolase ( $k_{\text{cat}} \sim 10 \text{ s}^{-1}$ ) reaction is  $\sim 67$  kJ/mol at 298 K, the enzyme must stabilize the carbanion by  $>130$  kJ/mol – a near impossible task considering that a typical hydrogen bond provides 4–12 kJ/mol (56). Clearly, an alternative catalytic strategy is required, although it is noted that some non-hydrolytic enzymes such as orotidine monophosphate decarboxylase may avoid carbanion formation by direct protonation of the fragmenting C-C bond (87).

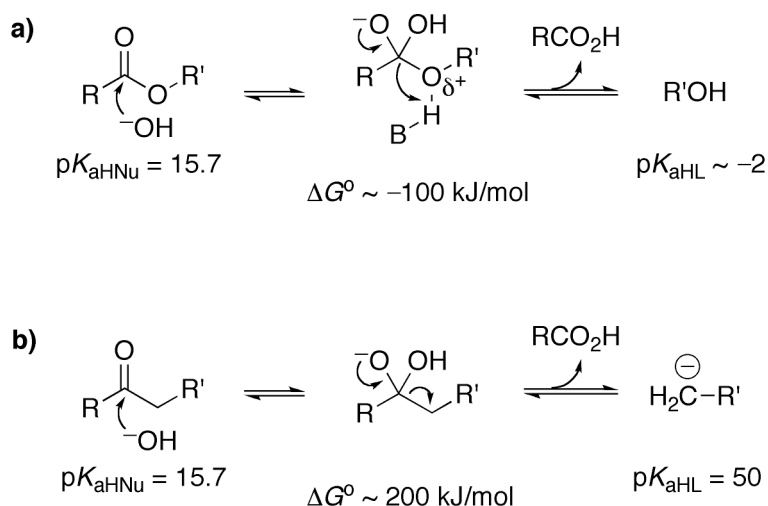
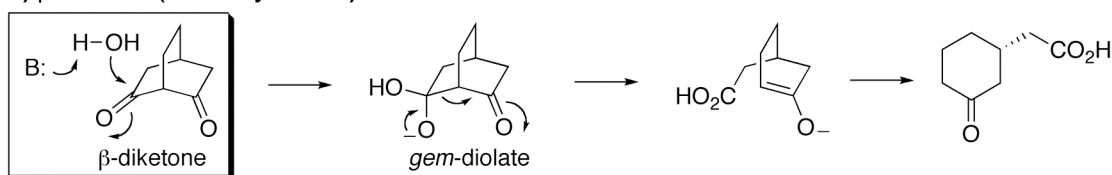


**Figure 9.** The reaction catalyzed by an esterase (a) is energetically more favourable than the reaction catalyzed by a C-C hydrolase (b). The subscripts accompanying  $pK_a$  refer to the conjugate acid of the nucleophile (HNu) or leaving group (HL).

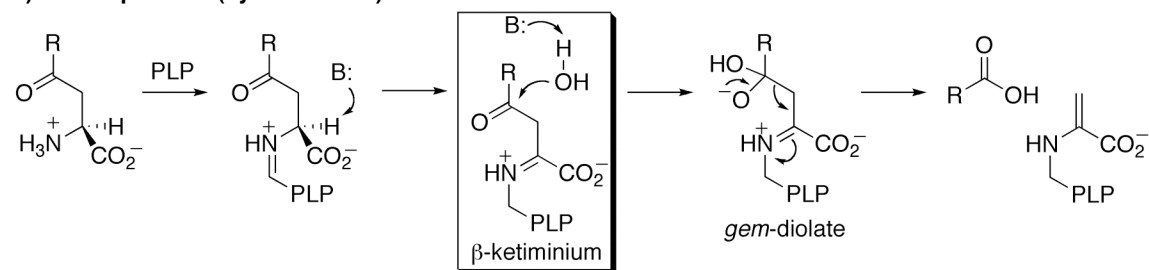
To overcome the difficulty associated with hydrolyzing C-C bonds, enzymes must

provide an electron sink for the leaving carbanion. This may be achieved via one of three very similar catalytic strategies that exploit a diketone-like functionality. The  $\beta$ -ketolase enzymes (Figure 10a) transform substrates with a good electron sink in the form of a  $\beta$ -diketone, allowing hydrolysis to proceed in the absence of cofactors (88-92). In the second group, the absence of  $\beta$ -diketo chemistry necessitates the recruitment of cofactors. For example, kynureninase uses pyridoxal 5'-phosphate (PLP) to hydrolyze the unactivated C-C bond of kynurenine (Figure 10b). In this reaction, the enzyme generates a  $\beta$ -ketiminium electron sink, which facilitates C-C hydrolysis in a fashion analogous to the  $\beta$ -ketolases (93, 94).

**a)  $\beta$ -ketolase (ABDH hydrolase)**



**b) PLP-dependent (kynureninase)**



**c) Tautomerase-hydrolase (MCP hydrolase)**

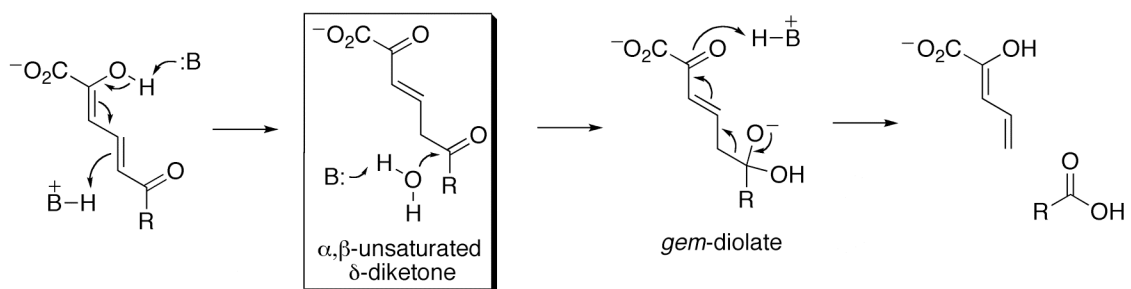


**Figure 10.** Examples of representative enzymes for each of the three general enzymatic strategies for hydrolytic cleavage of C-C bonds.

In contrast to the two C-C hydrolytic strategies mentioned above, the third group of enzymes benefits from neither a suitable leaving group nor the use of a cofactor (Figure 10c). This group includes the MCP hydrolases, as well as the polyketide shortening enzyme *Ayg1p* (90), 2,6-dihydroxy-*pseudo*-oxynicotine (DHPON) hydrolase (95, 96) and phloretin hydrolase (97, 98). Only the latter enzyme is not an  $\alpha/\beta$ -hydrolase. These enzymes encounter a common catalytic challenge of hydrolysis at a carbonyl carbon in an  $\alpha,\beta$ -unsaturated system, and have been proposed to solve this problem via enol-keto tautomerization prior to hydrolysis (95, 99). Because they are thought to employ both tautomerization and hydrolysis, they may be described as “tautomerase-hydrolase” enzymes.

### 1.5.2 The tautomerization reaction

Evidence supporting a tautomerization reaction in the MCP hydrolases was first obtained from both deuterium exchange and transient kinetic studies of MhpC. The former demonstrated that the overall reaction proceeded with retention of stereochemistry (*i.e.* a proton incorporated into the H5<sub>E</sub> position of HPD), and that the enzyme catalyzed additional exchange into H5 of the substrate, suggesting that a ketonized intermediate was formed and partially released into solution (99, 100). Transient kinetic analysis of MhpC at acidic pH showed a biphasic disappearance of substrate, with the second phase matching the monophasic formation of HPD (101). This behaviour was interpreted as a rapid ketonization followed by slower C-C cleavage and product release. Moreover, a kinetic model including partial release of the keto-intermediate could most satisfactorily describe the data, thereby supporting the release observed by deuterium exchange. This model also predicts that the keto-intermediate should accumulate to detectable levels in solution.

Some of the amino acid residues that are conserved among MCP hydrolases have been mutated to assess their catalytic contributions. As expected, the residues of the catalytic triad are essential, particularly His265 and Ser112 (BphD<sub>LB400</sub> numbering), for which mutation causes at least a 10<sup>3</sup>-fold loss in activity (102-105). Other conserved residues such as Arg190, Asn111, Trp266, Phe175 play important but less crucial roles (106). For example, substitution of Arg190 in both MhpC and a polyhistidine-tagged BphD<sub>LB400</sub> (Ht-BphD<sub>LB400</sub>) leads to ~700-fold reductions in  $k_{\text{cat}}$ , and transient kinetic analysis suggested that this residue correctly positions the substrate for tautomerization. Interestingly, substitution of His265 dramatically impairs the rate of an event proposed to represent ketonization. Hence, the catalytic histidine may transfer a substrate proton from the 2-hydroxyl to C5 (104, 105).

### 1.5.3 The hydrolytic reaction

Surprisingly, no evidence for nucleophilic catalysis has been obtained in the MCP hydrolases. Attempts to detect an acyl-enzyme by quenching the reaction of MhpC with a <sup>14</sup>C-labelled substrate yielded only very low stoichiometries (<1%) of covalently modified enzyme (107, 108). In the presence of H<sub>2</sub><sup>18</sup>O, the enzyme incorporated two <sup>18</sup>O atoms into ~5% of the acid product, and also catalyzed isotope exchange at the carbonyl of a non-hydrolysable substrate analog. These results were interpreted as evidence for a general base mechanism involving direct attack of water to form a *gem*-diolate intermediate (Figure 10c).

Subsequent studies have provided additional support for the *gem*-diolate mechanism. Hammett analysis of the BphD<sub>LB400</sub>-catalyzed hydrolysis a series of *para*-substituted HOPDAs revealed a negative correlation ( $\rho = -0.71$ ) between electron

withdrawing *para*-substituents and  $k_{\text{cat}}$  (109, 110). Because a positive correlation is observed in serine proteases (111, 112), this further differentiates MhpC from the classical nucleophilic mechanism of the serine hydrolases. The observed retro-aldol cleavage of a 6-hydroxy analog of HOPDA was also considered to support a general base mechanism (109). Finally, the absence of a clearly discernable burst upon hydrolysis of *p*-nitrophenyl acetate by Ht-BphD<sub>LB400</sub> was interpreted as evidence against acylation, although the authors note that the rate of *p*-nitrophenol production was faster than turnover (113).

The most direct evidence for the *gem*-diolate hypothesis has come from the observation of a <sup>13</sup>C NMR signal with the expected chemical shift (105). This intermediate was detected during steady-state turnover of C6 labelled HOPDA by His265Ala or Ser112Ala variants of Ht-BphD<sub>LB400</sub>, as well as by a His114Ala variant of MhpC. The *gem*-diol signal was also observed in the absence of enzyme, but line broadening in the presence of enzyme indicated that the intermediate was enzyme-bound. Nevertheless, it is not known if the intermediate is relevant to catalysis in the wild type enzyme.

These results challenge the accepted paradigm for serine hydrolase catalysis, and raise interesting questions concerning the role of the “nucleophilic” residue in the  $\alpha/\beta$ -hydrolase fold. The MCP hydrolase catalytic serine has been proposed to contribute a stabilizing hydrogen bond to the *gem*-diolate (104) (Figure 11). Although general base-catalyzed formation of *gem*-diolate intermediates is proposed to arise in C-C hydrolases that lack appropriate nucleophiles such as  $\beta$ -ketolases (88) (Figure 10a), kynureninase (93) (Figure 10b), and fumarylacetoacetate hydrolase (91), it is not apparent why this should be so in the  $\alpha/\beta$ -hydrolases. Indeed, a preference for covalent catalysis over

direct attack of water can be expected on the basis of several concepts. First, the “nucleophilic elbow” of the structural fold presumably predisposes the serine to nucleophilic catalysis (51). Moreover, the canonical oxyanion hole obviates the requirement for an additional hydrogen bond from serine. Second, because alkoxides are stronger nucleophiles than hydroxides (55, 56), the catalytic serine is predicted to react more readily than water with the substrate carbonyl. Third, the attack of serine on the substrate is intramolecular and therefore entropically favoured over the bimolecular attack of water (55, 56). Finally, if non-covalent interactions are insufficient, covalent catalysis may be required to assist binding (56). In summary, the question of covalent versus non-covalent catalysis in the MCP hydrolases awaits definitive resolution.

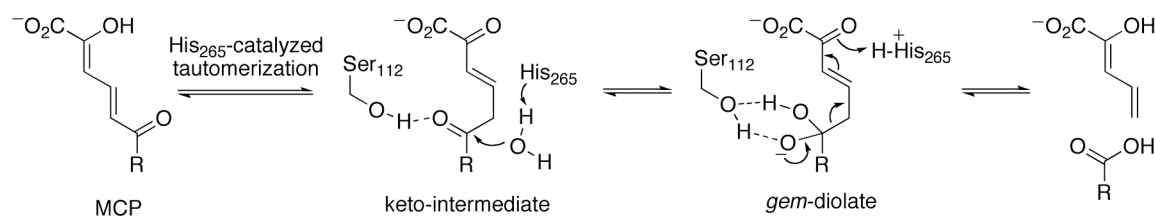


**Figure 11.** The role of the catalytic serine in MCP hydrolases proposed in reference (104).

### 1.6 Structural aspects of MCP hydrolases

Crystal structures of five MCP hydrolases have been solved: BphD<sub>RHA1</sub> (114), CumD<sub>IP01</sub> (103), Ht-CarC<sub>J3</sub> (115), MhpC (47, 106), and BphD<sub>LB400</sub> (116). The enzymes have a core α/β-hydrolase domain consisting of a highly twisted eight-stranded β sheet flanked by two α-helices on one side and three on the other. A lid domain occurs as an insertion of several helices between strands 6 and 7 of the core domain. An overlay of these enzymes revealed that the core domains superpose with high fidelity, but the less well-conserved lid domains exhibit greater conformational variability (116). Moreover, all enzymes show a “back-to-back” dimer interaction involving anti-parallel pairing of β8

strands. This may represent a basic structural unit in the MCP hydrolase family from which some members – for example tetrameric BphD<sub>LB400</sub> and octameric BphD<sub>RHA1</sub> – may construct higher oligomers.

The active site is located between the lid and core domains and includes the conserved Ser112-His265-Asp237 (BphD<sub>LB400</sub> numbering) catalytic triad (Figure 12). Moreover, Ser112 is located on the nucleophilic elbow, the canonical tight turn of the  $\alpha/\beta$ -hydrolase fold (51). The catalytic serine demarcates the bisection of the active site into polar (P) and nonpolar (NP) subsites. Depending on the crystal structure, the active site entrance appears to be at the P subsite (BphD<sub>RHA1</sub> and CumD<sub>IP01</sub>), NP subsite (Ht-CarC<sub>J3</sub> and BphD<sub>LB400</sub>), or both (MhpC). However, the cumulative structural data suggests that conformational changes are required to permit substrate entry and product release. For example, neither MhpC opening is sufficiently large to accommodate the substrate. Moreover, the conserved residue Arg190 is pointed outwards from the active site in BphD<sub>RHA1</sub> and CumD<sub>IP01</sub>, but in the other enzymes it extends to the active site and effectively closes the P subsite entrance.

The partitioning of the active site into polar and nonpolar subsites reflects a similar partitioning of polarity in the MCP substrates. All MCPs consist of a 2-hydroxy dienoate moiety that matches the P subsite, and a nonpolar moiety (R group) matching the NP subsite (Figure 4). Moreover, the structural variability of the substrate R group mirrors the lack of conservation among residues lining the NP subsite, whereas the invariance of the MCP dienoate moiety matches the strict conservation of residues in the P subsite; namely Gly43, Asn51, Asn111, Arg190, and Trp266.

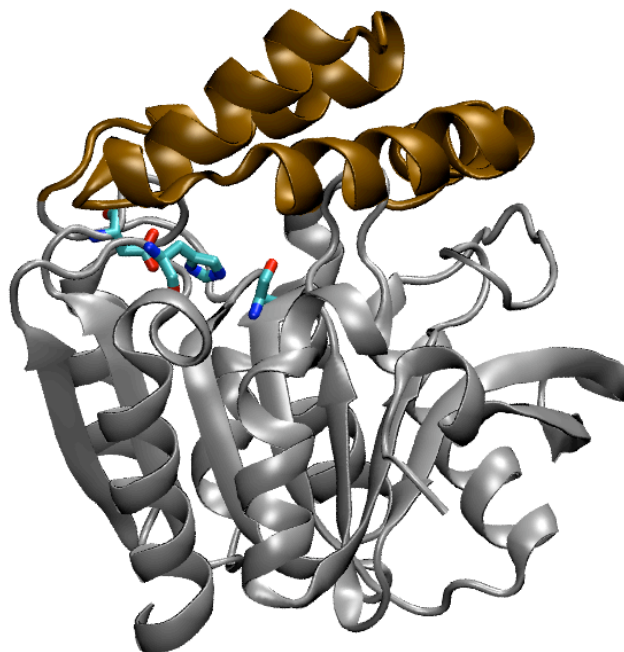


**Figure 12.** The structure of the BphD<sub>LB400</sub> monomer illustrates the lid domain (ochre, top) and the core domain (grey) of the  $\alpha/\beta$ -hydrolase fold. The residues of the active site catalytic triad are shown in stick representation. Figure prepared using VMD (117).

Enzyme-ligand structures suggest candidate active site residues that may catalyze the proposed enol-keto tautomerization. The most detailed picture has emerged from a 1.6 Å-resolution structure of the S112C variant of BphD<sub>LB400</sub> incubated with HOPDA (116). Although the phenyl ring was not satisfactorily accounted for, the electron density could be reasonably interpreted as a mixture of oxidized Cys112 and bound HPD product. This clear density for HPD enables the prediction of a series of hydrogen bonds between the enzyme and the substrate dienoate moiety (Figure 13). The substrate carboxylate interacts with Arg190, Gly43, Asn51, and Trp266, whereas the C2 oxygen may hydrogen bond to Asn111, Trp266, and His265. Although the latter interaction is rather long (3.3 Å), it implies that His265 can promote tautomerization via abstraction of the C2 hydroxyl proton. The crystal structure suggests that C5 may be protonated by either Ser112 or His265. Although His265 is somewhat farther away from C5 (3.8-4.5

Å), this residue's observed conformational flexibility (103, 116) suggests it may be sufficiently mobile to protonate C5. Indeed, least squares fitting of this structure to S112C and wild type BphD<sub>LB400</sub> in the absence of ligand indicated His265-to-C5 distances as low as 2.9 Å. Moreover, reasonable distances between His263 and C5 (3.9 Å) and C2-OH (3.2 Å) of a substrate analog were observed in MhpC. Interestingly, a role in tautomerization is consistent with the kinetic interpretations (104, 105) mentioned in section 1.5.2.

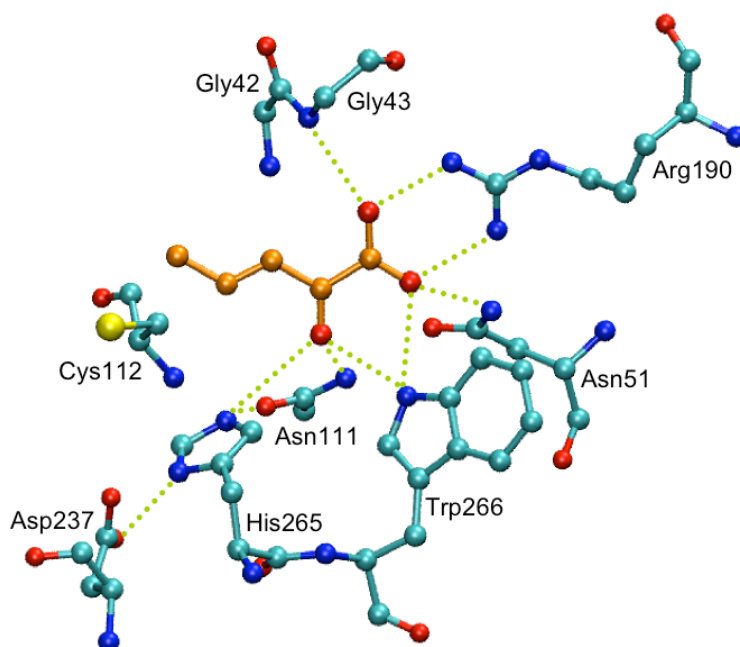


**Figure 13.** The structure of HPD in the active site of an S112C variant of BphD<sub>LB400</sub>. Carbon, nitrogen, oxygen and sulfur atoms are coloured cyan, blue, red, and yellow, respectively. HPD carbon atoms are coloured orange. Green dotted lines represent potential hydrogen bonds. Adapted from (116). Figure prepared using VMD (117).

Other active site structural features of mechanistic interest include the oxyanion hole and the catalytic triad. Although the oxyanion hole residues are appropriately positioned (main chain N-H of Met113 and Gly42) for nucleophilic catalysis, the crystallographically-observed arrangement of the catalytic triad suggests an alternative

use of these residues. Unlike other  $\alpha/\beta$ -hydrolases, the His-Ser hydrogen bond is either absent (BphD<sub>RHA1</sub>, Ht-CarC<sub>J3</sub>, BphD<sub>LB400</sub>) or longer (MhpC) in the MCP hydrolases. Although this may reflect the proposed non-nucleophilic role for the catalytic serine (Figure 11), it may also reflect the enhanced flexibility of histidine required for catalyzing tautomerization.

### 1.7 Aim of this study

As described in section 1.5.2, stopped-flow kinetic studies of MhpC and BphD have been performed at single wavelengths. However, such studies do not provide full spectra of intermediates, thereby leading to greater uncertainty when assigning absorbance changes to physical events. The first goal of this thesis was to obtain full spectra of transient reaction intermediates in the BphD<sub>LB400</sub>-catalyzed hydrolysis of HOPDA. This was accomplished using a stopped-flow apparatus equipped with a photodiode array detector. These results were supplemented by steady-state kinetics, deuterium exchange, and HPLC analyses.

The catalytic histidine of the MCP hydrolases has been proposed to mediate tautomerization and hydrolysis, while the catalytic serine is thought to promote hydrolysis. Thus, the second goal was to examine the effects of BphD<sub>LB400</sub> active site substitutions on the accumulation of intermediates. Full spectra of intermediates and their rates of formation were determined by stopped-flow spectrophotometry upon mixing HOPDA with S112A, H265A, and S112A/H265A enzyme variants. The resulting insights into the roles of active site residues in tautomerization were supplemented by measuring the abilities of variants to tautomerize the product, HPD. The results are discussed in terms of the crystal structures of intermediates trapped in the S112A and S112A/H265A variants.

The third goal of the thesis was to investigate the mechanistic basis for inhibition of BphD<sub>LB400</sub> by 3-Cl HOPDA. To determine if inhibition results from steric or electronic features of the additional chlorine atom, a series of 3-substituted HOPDAs were studied by steady-state kinetics. The absorption spectra of intermediates obtained in the previous section enabled stopped-flow spectrophotometric evaluation of the effects of 3-substituents on individual steps in the enzyme mechanism. The crystal structure of an S112A:3-Cl HOPDA binary complex is included in the interpretation of these results.

The final goal of the thesis was to further characterize the mechanism of hydrolysis of BphD<sub>LB400</sub>. As described in section 1.5.3, MCP hydrolase catalysis is believed to proceed via a *gem*-diolate intermediate instead of the prototypical acyl-enzyme. However, no definitive evidence for either mechanism has been produced. In an attempt to distinguish the two mechanisms in BphD<sub>LB400</sub>, the ratio of hydrolysis to competing methanolysis was compared for two substrates predicted to generate the same benzoyl-enzyme intermediate – HOPDA and *p*-nitrophenyl benzoate. The ratio of benzoate to methyl benzoate produced from each substrate was determined by HPLC, and together with kinetic analysis provided insight into the mechanism of hydrolysis.

## Chapter Two: MATERIALS AND METHODS

### 2.1 Chemicals

#### 2.1.1 Commercially and privately sourced

Protein sequencing grade trypsin, 3-methylcatechol, biphenyl, 4,4'-diF-biphenyl, and *p*-nitrophenyl benzoate were purchased from Aldrich (Mississauga, ON). 2,3-Dihydroxybiphenyl (DHB), 4-Cl-DHB, and 4-methyl-DHB were gifts from Victor Snieckus (Department of Chemistry, Queens University, Kingston, ON). Deuterium oxide was from Cambridge Isotope Laboratories (Andover, MA). Catechol 2,3-dioxygenase was used to prepare 2-hydroxy-6-oxo-2,4-heptadienoic acid from 3-methylcatechol as previously described (118). All other chemicals were of analytical grade and used without further purification.

#### 2.1.2 Preparation of 4,4'-difluoro-2,3-dihydroxybiphenyl (4,4'-diF DHB)

A plate of W medium (119) was streaked with frozen stock of *Pandoraea pnomenus* (formerly *Comamonas testosteroni*) B-356, and incubated with biphenyl crystals in the lid at 30 °C until colonies were visible (~5 days). Several colonies were added to 3 mL of W medium containing 1 mg biphenyl and incubated at 30 °C and 250 rpm until cloudy (~4 days). Alternatively, this step could be shortened to ~2 days if a 50 µL aliquot of frozen stock was used to inoculate the 3 mL culture. One litre of W medium containing 0.5 g biphenyl in a 2-litre flask was inoculated with 1 mL of starter culture and incubated as above. When the O.D. at 600 nm reached 1, the culture was carefully decanted to remove biphenyl crystals and then centrifuged for 10 min at 7000 x g. The pellet was washed two times with potassium phosphate buffer ( $I = 0.1$  M, pH 7.5)

to remove residual biphenyl and resuspended in 500 mL of buffer supplemented with 100 mg of 4,4'-diF biphenyl and 7 mg 3-chlorocatechol. The latter was included to inactivate DHBD (120) and thereby prevent enzymatic transformation of the produced 4,4'-diF DHB. The culture was incubated as above and 50  $\mu$ L aliquots were analyzed by HPLC at 30 min intervals using a Prodigy ODS Prep column, (2.1 x 250 mm) (Phenomenex, Torrance, CA), operating at a flow rate of 1.5 mL/min. The mobile phase initially consisted of a 30:70 ratio of solvent A (0.5% aqueous H<sub>3</sub>PO<sub>4</sub>) to solvent B (methanol) for the first 5 min of the run, then a linear gradient was used to achieve 100% B at 10 min. The retention time of 3-chlorocatechol was 2.6 min, 4,4'-diF DHB eluted at 5.4 min, and 4,4'-diF biphenyl at 13 min. When the maximum concentration of 4,4'-diF DHB in the culture was reached as judged by HPLC (after ~3 h), the culture was filtered to remove unreacted insoluble starting material, and then extracted three times with ~200 mL of ethyl acetate. The pooled fractions were dried over anhydrous MgSO<sub>4</sub> and rotary evaporated to dryness. The crude extract was dissolved in an appropriate volume of mobile phase (20:80 A:B ratio) and purified by preparative HPLC using a Prodigy ODS Prep column, (21.2 x 250 mm) (Phenomenex, Torrance, CA, USA) operating at a flow rate of 8.5 ml/min. The 4,4'-diF DHB (retention time ~ 8 min) was collected, extracted into ethyl acetate, dried, and evaporated as above. The purity was estimated to be >95% by HPLC. The 4,4'-diF DHB was dissolved in 10% ethanol, 80% H<sub>2</sub>O, and 10% D<sub>2</sub>O in order to collect NMR spectra at 25 °C using a 600 MHz spectrometer at the Department of Chemistry, University of Rochester. The <sup>1</sup>H NMR reference compound was 100  $\mu$ M DSS (2,2-dimethyl-2-silapentane-5-sulfonate), and was used as an indirect reference for <sup>19</sup>F NMR. Found by <sup>19</sup>F{<sup>1</sup>H} NMR: -3.6 (s, 1F), -23.9 (s, 1F); <sup>1</sup>H NMR: 6.75-6.82 (m, 2H), 7.21 (t, 2H, *J* = 6 Hz), 7.52 (t, 2H, *J* = 6 Hz).

### 2.1.3 Preparation of HOPDAs

HOPDA was enzymatically generated from DHB using DHBD. Briefly, ~50 mg DHB in 500 mL buffer (potassium phosphate,  $I = 100$  mM, pH 7.5) was quantitatively converted to HOPDA by DHBD. The HOPDA solution was acidified to pH 2-3 using 2 N HCl and extracted 3 times with 0.5 volumes of ethyl acetate. The organic extract was dried over anhydrous  $MgSO_4$  and rotary evaporated to dryness. If necessary, the HOPDA was purified by HPLC from a methanol:water (0.5%  $H_3PO_4$ ) mixture (80:20) using a Waters 2695 separation module fitted with a Prodigy 10- $\mu$ m ODS-Prep column (21.2 x 250 mm) (Phenomenex, Torrance, CA). HOPDA was eluted in the same methanol/water (0.5%  $H_3PO_4$ ) mixture at a flow rate of 7 mL/min. The HOPDA-containing fractions were pooled, extracted into ethyl acetate, dried, and evaporated as described above, yielding the purified HOPDA as a powder. Similarly, 3-Cl HOPDA, 3-Me HOPDA, and 3,10-diF HOPDA were generated from 4-Cl DHB, 4-Me DHB, and 4,4'-diF DHB, respectively.

### 2.2 Mutagenesis, protein production and purification

BphD variants were generated using pSS184, a broad host range expression plasmid carrying the *bphD* gene as previously described (118). The Ser112Cys (116) and Ser112Ala (121) variants were constructed by Dr. Stephen Seah to generate pSS184SC and pSS184SA constructs, respectively. Substitution of His265 with alanine (H265A) was performed using a 5'-phosphorylated primer (H265A: CTCCAAGTGCGGCGCTTGGGCGCAATGG-3') and the QuikChange Multi site-directed mutagenesis kit (Stratagene, La Jolla, CA). Genes encoding the single (H265A) and double (S112A/H265A) variants were generated using pSS184 and pSS184SA,

respectively, yielding pSS184HA and pSS184SAHA. The nucleotide sequences of variants were confirmed using an ABI 373 Stretch (Applied Biosystems, Foster City, CA) and Big-Dye v3.1 terminators.

Although protein could be produced using the pSS314 construct, it was too large (>11 kb) to be used for mutagenesis by the QuikChange method. Hence the smaller pSS184 constructs were used for protein production by freshly transforming the appropriate plasmid construct into *Escherichia coli* DH5 $\alpha$ . One millilitre of LB (100  $\mu$ g/mL ampicillin) was inoculated with a single transformant and incubated overnight at 37 °C and 250 rpm, and 0.5 mL was then used to inoculate 100 mL of medium, which was incubated overnight at 30 °C and 250 rpm. Four 2-litre flasks, each containing 1 litre of pre-warmed medium, were each inoculated with 10 mL of overnight culture and incubated at 37 °C and 250 rpm. When the O.D. at 600 nm reached 0.4 – 0.6, the cultures were induced with 0.5 mM isopropyl-1-thio- $\beta$ -D-galactopyranoside and incubated for an additional 18 hours prior to harvesting.

BphD was purified using a modified version of a published protocol (118) using an ÄKTA Explorer system (GE Healthcare, Uppsala, Sweden). Buffers were made using water from a Barnstead NANOpure UV apparatus (Barnstead International, Dubuque, IA) purified to a resistivity of greater than 17 M $\Omega$ •cm. Buffer A was 20 mM HEPES, pH 7.5.

After centrifugation of the culture, the resulting cell pellet was resuspended in 15 mL of buffer A, to which was added 1 mg DNase I (Roche Diagnostics, Laval, QC), 1 mM MgCl<sub>2</sub>, and 1 mM CaCl<sub>2</sub>. The cells were lysed by three passages through a Emulsiflex C-5 cell disrupter (ATA Scientific, Sutherland, Australia) operating at a pressure of 15,000 psi. The cell debris was removed by ultracentrifugation at 120,000 x g

for 60 min. The supernatant was removed and filtered through a 0.45  $\mu\text{m}$  Minisart cellulose filter (Sartorius, Epsom, UK) to yield  $\sim 20$  mL of raw extract.

The raw extract was loaded onto 28 mL of Source 15Q anion exchange resin (GE Healthcare) packed in an AP-2 column (Waters Corp., Milford, MA) that had been equilibrated with buffer A containing 50 mM NaCl. The column was operated at a flow rate of 10 mL/min using a linear gradient of 50 to 200 mM NaCl over 15 column volumes. BphD eluted at 130 mM NaCl. Fractions of 5-10 mL were collected, and those containing enzyme activity were pooled and concentrated to  $\sim 3$  mL using an Amicon stirred cell concentrator housing a YM10 ultrafiltration membrane (Millipore, Billerica, MA). The BphD-containing solution was brought to 0.53 M  $(\text{NH}_4)_2\text{SO}_4$ , and the sample was briefly (2 min) centrifuged at maximum speed in a bench top microcentrifuge to remove any precipitate. The supernatant was loaded onto 23 mL of Source 15PHE resin (GE Healthcare) in an AP-2 column (Waters Corp.) operating at a flow rate of 10 mL/min using 0.53 M  $(\text{NH}_4)_2\text{SO}_4$  in buffer A. In contrast to the protein's behaviour on phenylsepharose resin (*118*) where it eluted at 0.34 M  $(\text{NH}_4)_2\text{SO}_4$ , BphD eluted after 2 column volumes of isocratic flow using Source 15PHE. BphD-containing fractions were exchanged into buffer A and concentrated by ultrafiltration. For protein samples used for crystallography, an additional gel filtration step was performed whereby the concentrated sample ( $\sim 3$  mL) was loaded onto a HiLoad 26/60 Superdex 200 column (GE Healthcare) that had been equilibrated with buffer A containing 150 mM NaCl. BphD eluted in the same buffer and fractions were combined, exchanged into buffer A and concentrated to  $>10$  mg/mL by ultrafiltration. Protein droplets were flash frozen in liquid nitrogen and the resulting beads were stored at  $-80$   $^\circ\text{C}$ .

## 2.3 Protein analysis

The BioRad MiniPROTEAN II apparatus was used for SDS-PAGE analysis, and the gels were stained with Coomassie Blue according to standard procedures (122). Concentration of protein in impure protein preparations (e.g. raw extract) was determined using the Bradford method (123). Concentration of pure protein preparations was determined colorimetrically using the molar absorptivity of BphD at 280 nm ( $\epsilon_{280} = 55.4 \text{ mM}^{-1} \text{ cm}^{-1}$ ). The latter was determined from the absorbance at 280 nm of a protein sample whose concentration was determined by amino acid analysis at the Advanced Protein Technology Centre (Hospital for Sick Children, Toronto, ON).

## 2.4 Steady-state kinetic experiments

### 2.4.1 Standard spectrophotometric assay

Spectrophotometric measurements of BphD hydrolytic activity were performed by monitoring absorbance on a Varian Cary 1E spectrophotometer equipped with a thermostatted cuvette holder (Varian Canada, Mississauga, ON) maintained at  $5 \pm 3 \text{ }^\circ\text{C}$ , or  $25 \pm 1 \text{ }^\circ\text{C}$  controlled by Cary WinUV software version 2.00. Some experiments were performed using a Varian Cary 5000 spectrophotometer maintained at  $25 \pm 0.5 \text{ }^\circ\text{C}$  controlled by Cary WinUV software version 3.00. For low temperature readings on the Cary 1E, the cuvette holder was modified to deliver a stream of nitrogen gas over each side of the quartz cuvette to minimize condensation. Unless otherwise noted, experiments were performed in the standard buffer of potassium phosphate ( $I = 0.1 \text{ M}$ ), pH 7.5. Typically, reactions were initiated by adding 5 – 10  $\mu\text{L}$  of appropriately diluted enzyme to a substrate solution to make a total volume of 1.0 mL. Initial velocities were determined from the slope of the linear progress curves using the Cary WinUV software. For HOPDA, the reaction was monitored at the absorbance maximum of 434 nm, at

which the molar absorptivity is  $25.7 \text{ mM}^{-1} \text{ cm}^{-1}$  (41). The molar absorptivity of 3,10-diF-HOPDA ( $\epsilon_{438} = 37.9 \text{ mM}^{-1} \text{ cm}^{-1}$ ) was calculated from its absorption spectrum after quantification by measuring the amount of dioxygen consumed in the ring-opening reaction of 4,4'-diF DHB catalyzed by DHBD. Dioxygen consumption was measured using a Clark-type polarographic oxygen electrode (Yellow Springs Instruments model 5301, Yellow Springs, OH) as previously described for other HOPDAs (118). The molar absorptivity of 3-Me HOPDA ( $\epsilon_{430} = 18.7 \text{ mM}^{-1} \text{ cm}^{-1}$ ) was determined by recording the absorption spectrum of a known quantity of 4-Me DHB immediately after cleavage by DHBD. At the absorbance maximum of 400 nm, the molar absorptivity of *p*-nitrophenol was  $12.8 \text{ mM}^{-1} \text{ cm}^{-1}$ . One unit of enzyme activity was defined as the quantity of enzyme required to consume 1  $\mu\text{mol}$  of substrate. The Michaelis-Menten equation was fit to the data using the LEONORA program (124).

#### 2.4.2 Product inhibition

For HPD inhibition experiments, HPD was generated *in situ* from TodF-catalyzed hydrolysis of freshly prepared 2-hydroxy-6-oxo-2,4-heptadienoate; the concentration of the latter was calculated from the previously determined molar absorptivity (118). Sufficient TodF enzyme was added to ensure complete formation of HPD in approximately 2 min, after which time HOPDA and BphD<sub>LB400</sub> were immediately added, and the BphD<sub>LB400</sub>-catalyzed hydrolysis of HOPDA was spectrophotometrically monitored at 434 nm. The decay of HPD was not greatly accelerated by TodF: ~10% loss of HPD occurred over the course of the 5 min measurement. BphD<sub>LB400</sub>-catalyzed HOPDA hydrolysis was not affected by the presence of the TodF enzyme or by the presence of acetate (~100  $\mu\text{M}$ ). Steady-state rate equations describing competitive, uncompetitive, or mixed inhibition were fit to data using the program LEONORA (124).

### 2.4.3 BphD<sub>LB400</sub>-catalyzed HPD ketonization

HPD was generated together with benzoic acid by BphD<sub>LB400</sub>-catalyzed hydrolysis of HOPDA. Immediately after the reaction was complete (as monitored by absorbance at 434 nm), the solution was acidified to pH ~3 with 2 N HCl and extracted three times with ethyl acetate (0.3 volumes each extraction), dried over anhydrous MgSO<sub>4</sub>, and evaporated to dryness. The HPD/benzoic acid mixture was dissolved in ethanol and a small volume (< 0.5%) was added to buffer. The decay of HPD at 270 nm was monitored before and after addition of enzyme. Activity was calculated using the previously reported molar absorptivity,  $\epsilon_{270} = 19.2 \text{ mM}^{-1} \text{ cm}^{-1}$  (125).

### 2.5 Stopped-flow kinetic experiments

Experiments were conducted using an SX.18MV stopped-flow reaction analyzer (Applied Photophysics Ltd., Leatherhead, UK) equipped with a photodiode array detector. The temperature of the drive syringe chamber and optical cell was controlled by circulating water. For wavelengths below 350 nm, a deuterium lamp was employed to improve the signal-to-noise ratio, while a Xe lamp was used for wavelengths above 350 nm. Concentrations of reactants and buffer conditions were varied as described in Results. For each experiment, the data are averages of three replicates, and each replicate was generated by averaging at least five shots of the stopped-flow drive syringe. Single, double, or treble exponential equations were fit to the averaged time courses for single wavelength data using the SX18MV software running on the system's Acorn A5000 computer and the RISC OS 3.7 operating system. These fits provided reciprocal relaxation times ( $1/\tau$ ) and amplitudes; good fits are characterized by random variation in the fit residuals. Multiple wavelength data from the time courses of single turnover experiments were exported to Excel (Microsoft, Redmond, WA) and then averaged.

Selected single wavelengths of the averaged data were analyzed using the SX18MV software.

## 2.6 HPLC analysis of coupling

Separations were performed on a Waters 2695 system equipped with an ODS Hypersil C<sub>18</sub> column (5  $\mu$ m, 125 x 4 mm) (Hewlett Packard, Palo Alto, CA), operating at a flow rate of 1 mL/min. Sample injections of 95  $\mu$ L were eluted with 55% methanol and 45% water containing 0.5% phosphoric acid. Benzoic acid was quantified by comparing peak areas at 230 nm to those of standards containing known concentrations (5, 20, 100, and 250  $\mu$ M) of benzoic acid. Sufficient BphD<sub>LB400</sub> to permit complete transformation in 35 min was added to 4 mL of potassium phosphate buffer ( $I = 0.1$  M), pH 7.5 containing 95  $\mu$ M HOPDA (calculated using  $\epsilon_{434} = 25.7 \text{ mM}^{-1} \text{ cm}^{-1}$  (41)). The reaction was monitored spectrophotometrically at 434 nm, and a 200  $\mu$ L aliquot was removed at each increment of 10% conversion (judged by  $A_{434}$ ), and immediately quenched by adding 244  $\mu$ L methanol containing 0.41% phosphoric acid. The quenched reaction solutions were analyzed by HPLC as described above (retention times: HPD, 1.6 min; benzoic acid, 2.0 min; HOPDA, 2.9 min).

## 2.7 Deuterium incorporation

Deuterated buffer was prepared by evaporating 700  $\mu$ L of potassium phosphate buffer ( $I = 5$  mM), pH 7.5 and resuspending in the same volume of deuterium oxide. To 700  $\mu$ L of deuterated or non-deuterated buffer was added a small volume of concentrated HOPDA dissolved in ethanol, such that the final HOPDA concentration was 1 mM, and the solution contained 2% ethanol. BphD<sub>LB400</sub> (8  $\mu$ L) was added and the reaction was followed spectrophotometrically at 434 nm until completion ( $< 4$  min). Immediately

upon reaction completion, 7  $\mu\text{L}$  of 2 N HCl was added, and the reaction was extracted 3 times with 0.5 volumes of ethyl acetate and then evaporated under a stream of nitrogen gas. The dried sample was redissolved in acetone- $d_6$  and transferred to an NMR tube for analysis using a Varian 500 MHz NMR spectrometer (Varian Inc., Mississauga, ON). A reaction was also quenched approximately 1 min after completion to allow observation of ketonized HPD ((*E*)-2-oxo-3-pentenoic acid). Found for HPD:  $^1\text{H}$  NMR (acetone- $d_6$ , 500 MHz)  $\delta$  5.18 (1H, dd,  $J_{4,5E} = 10.3$  Hz,  $J_{5Z,5E} = 1.9$  Hz, H-5<sub>E</sub>), 5.39 (1H, dd,  $J_{4,5Z} = 17.2$  Hz,  $J_{5Z,5E} = 1.9$  Hz, H-5<sub>Z</sub>), 6.21 (1H, d,  $J_{3,4} = 11.0$  Hz, H-3), 6.77 (1H, dt,  $J_{4,5Z} = 17.0$  Hz,  $J_{3,4} = 10.7$  Hz,  $J_{4,5E} = 10.7$  Hz, H-4); for (*E*)-2-oxo-3-pentenoic acid:  $^1\text{H}$  NMR (acetone- $d_6$ , 500 MHz)  $\delta$  6.59 (1H, d,  $J_{3,4} = 15.6$  Hz, H-3), 7.15 (1H, dq,  $J_{3,4} = 15.8$  Hz,  $J_{4,5} = 6.7$  Hz, H-4). The acetone signal obscured the signal from H-5 of the latter compound (expected at 2.15 ppm). Nevertheless, the H-3 and H-4 chemical shifts and coupling constants agreed with a previous report (126).

## 2.8 HPLC analysis of product ratios from nucleophile partitioning

The ratio of BphD-catalyzed substrate hydrolysis versus methanolysis was measured by HPLC quantification of the ratio of benzoate to methyl benzoate products, respectively. The ratio was measured for both HOPDA and *p*-nitrophenyl benzoate (pNPB). The reaction was initiated by adding BphD (final concentration, 11 nM) to a quartz cuvette containing potassium phosphate buffer ( $I = 0.1$  M, pH 7.5, 25  $^\circ\text{C}$ ), 0.1% (v/v) methanol, 0.1% (v/v) acetone, and substrate (10 – 15  $\mu\text{M}$ ). The progress of the reaction was monitored at 434 nm for disappearance of HOPDA or 400 nm for the production of *p*-nitrophenol. Upon completion, the reaction was quenched with an equal volume of methanol (containing 0.5%  $\text{H}_3\text{PO}_4$ ), and 50  $\mu\text{L}$  was analyzed on a Waters 2695 system equipped with a Hewlett Packard ODS Hypersil C<sub>18</sub> column (5  $\mu\text{m}$ , 125 x 4 mm)

operated at a flow rate of 1 mL/min. Solvent A was 0.5% aqueous  $\text{H}_3\text{PO}_4$ , and solvent B was methanol. The sample was eluted using the following solvent gradients: (i) 10 – 20% B from 0 - 20 min, (ii) 20 – 40% B from 20 – 30 min, (iii) 40 – 100% B from 30 – 32 min. Product elution times: HPD, 5.2 min; *p*-nitrophenol, 12.5 min; benzoic acid, 14.9 min; methyl benzoate, 30.5 min. Peak areas were obtained using the Millennium software (Waters Corp.).

## Chapter Three: RESULTS

### 3.1 Mechanistic analysis of wild type BphD<sub>LB400</sub>

#### 3.1.1 Stopped-flow spectrophotometry

Stopped-flow experiments were performed using a diode array detector to resolve and spectrophotometrically characterize intermediates during a single catalytic cycle. Figure 14 presents data from an experiment performed under ‘slow’ conditions ( $T = 3.2$  °C, 20% glycerol). Using a 2:1 ratio of enzyme (8  $\mu\text{M}$ ) to substrate (4  $\mu\text{M}$ ), the HOPDA enolate absorbance band ( $\lambda_{\text{max}} = 434$  nm) was rapidly transformed to a red-shifted species (E:S<sup>red</sup>) with maxima at 473 and 492 nm (Figure 14A). At 25 °C the transformation was approximately 50% complete within the dead time of the instrument (1.2 ms), indicating a process occurring with reciprocal relaxation time,  $1/\tau_1 \sim 500$  s<sup>-1</sup> (127).<sup>1</sup> The E:S<sup>red</sup> intermediate decayed in a biphasic manner (at 25 °C,  $1/\tau_2 = 54 \pm 4$  s<sup>-1</sup>,  $1/\tau_3 = 5.8 \pm 0.9$  s<sup>-1</sup>), with similar phase amplitudes (Figure 14B, Table 1), and  $1/\tau_3$  similar to  $k_{\text{cat}}$  (41, 43, 105, 118). Concurrent with E:S<sup>red</sup> decay, a biphasic increase occurred at 270 nm, the absorbance maximum of HPD (at 25 °C,  $1/\tau_2 = 48 \pm 12$  s<sup>-1</sup>,  $1/\tau_3 = 8.3 \pm 0.7$  s<sup>-1</sup>), followed by a slower single exponential decay (Figure 14C). Thus, decay of the E:S<sup>red</sup> intermediate appears to be coupled to HPD formation.

---

<sup>1</sup> For an instrument dead time of 1.2 ms, only ~50% of a reaction with  $1/\tau = 500$  s<sup>-1</sup> may be observed. The observable fraction of the reaction ( $f_{\text{obs}}$ ) can be determined from the instrument dead time ( $t_d$ ) and the half-life of the reaction ( $t_{1/2}$ ) as follows:  $f_{\text{obs}} = (1/2)^{(t_d/t_{1/2})}$ . See reference (127).

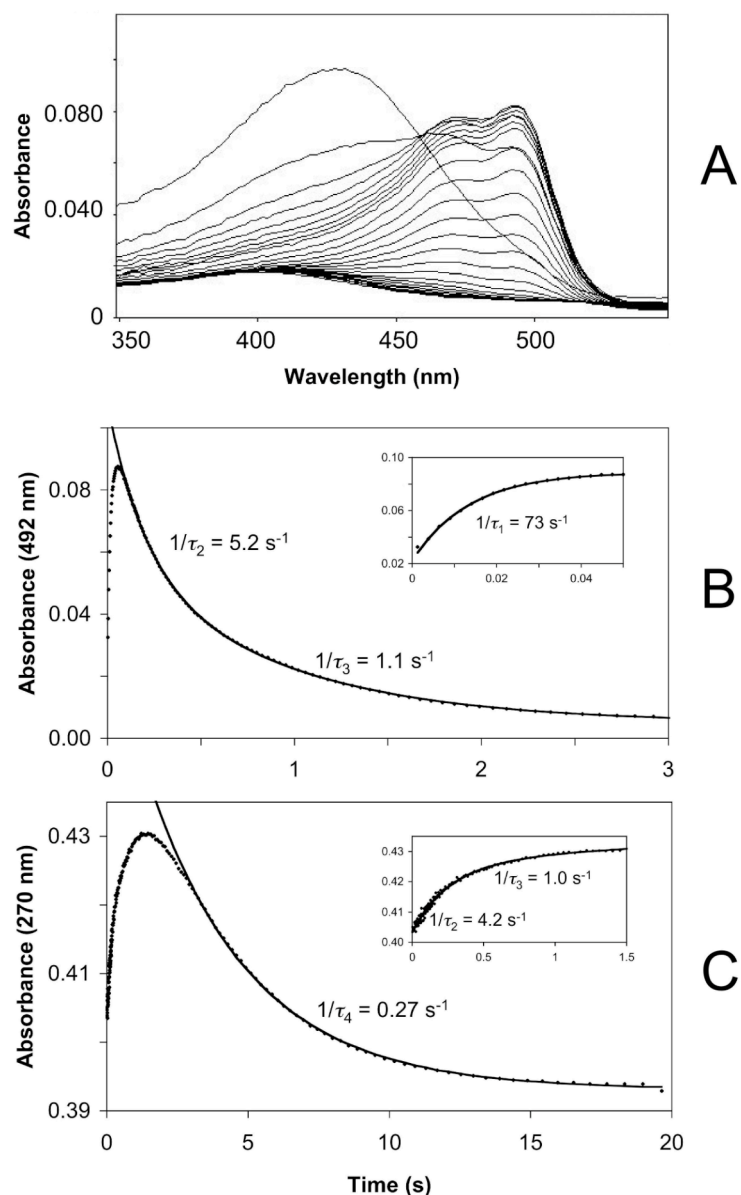


**Figure 14.** A representative stopped-flow experiment illustrating a single turnover of HOPDA (4  $\mu\text{M}$ ) by BphD<sub>LB400</sub> (8  $\mu\text{M}$ ) at 3.2 °C in potassium phosphate buffer supplemented with 20% glycerol ( $I = 0.1 \text{ M}$ ), pH 7.5. A) Time-resolved spectral changes show free HOPDA ( $\lambda_{\text{max}} = 434 \text{ nm}$ ) transformed to an enzyme-bound form with a red-shifted absorbance, E:S<sup>red</sup> ( $\lambda_{\text{max}} = 492 \text{ nm}$ ). B) Absorbance at 492 nm versus time shows the decay of the E:S<sup>red</sup> intermediate. The solid line denotes the double exponential fit. The inset shows the single exponential fit for the formation of the E:S<sup>red</sup> intermediate. C) Absorbance at 270 nm versus time for the formation/decay of the HPD product. Data points are shown together with the fit of a single exponential (solid line) describing HPD decay. Inset shows the formation of HPD and its fit to a double exponential.

**Table 1.** Reciprocal relaxation times and amplitudes for single turnover reactions.

| T<br>(° C)      | Glycerol<br>(% v/v) | Wavelength<br>(nm)        | Phase 1 <sup>a</sup> | Phase 2 <sup>b</sup><br>(% total amplitude) | Phase 3<br>(% total amplitude) | Phase 4 <sup>c</sup> |
|-----------------|---------------------|---------------------------|----------------------|---|--------------------------------|----------------------|
| 25              | 0                   | 270 (HPD)                 | -                    | 48 ± 12 (89)                                | 8.3 ± 0.7 (11)                 | 0.59 ± 0.04          |
|                 |                     | 492 (E:S <sup>red</sup> ) | ~500                 | 54 ± 4 (68)                                 | 5.8 ± 0.9 (32)                 | -                    |
| 3.2             | 20                  | 270 (HPD)                 | -                    | 34 ± 2 (51)                                 | 5.3 ± 0.3 (49)                 | 0.71 ± 0.01          |
|                 |                     | 492 (E:S <sup>red</sup> ) | ~200                 | 33 ± 2 (66)                                 | 5.5 ± 0.4 (34)                 | -                    |
| 3.2             | 0                   | 270 (HPD)                 | -                    | 12 ± 2 (51)                                 | 2.3 ± 0.6 (49)                 | 0.22 ± 0.01          |
|                 |                     | 492 (E:S <sup>red</sup> ) | ~200                 | 8.7 ± 0.3 (49)                              | 1.3 ± 0.2 (51)                 | -                    |
| 20              | 20                  | 270 (HPD)                 | -                    | 3.8 ± 0.4 (68)                              | 1.0 ± 0.1 (32)                 | 0.25 ± 0.03          |
|                 |                     | 492 (E:S <sup>red</sup> ) | 66 ± 6               | 4.5 ± 0.8 (49)                              | 1.2 ± 0.1 (51)                 | -                    |
| 20 <sup>d</sup> | 20                  | 270 (HPD)                 | -                    | 4.0   | -                              | 0.41                 |
|                 |                     | 492 (E:S <sup>red</sup> ) | ~130                 | 4.4 (45)                                    | 1.1 (55)                       | -                    |

Units are s<sup>-1</sup>. Errors are reported as the standard deviation of 3 measurements.

<sup>a</sup>Phase 1 represents the rapid formation of E:S<sup>red</sup>.

<sup>b</sup>The amplitudes are reported as a percentage of the total amplitude of phase 2 and phase 3 combined.

<sup>c</sup>Represents the enzyme-catalyzed ketonization of HPD.

<sup>d</sup>Experiment performed with 6:1 ratio of enzyme (20 μM) to substrate (4 μM).

The decay of HPD is due to tautomerization to the more stable  $\alpha/\beta$ -unsaturated ketone, a process which occurs non-enzymatically on a timescale of minutes (125). The faster HPD decay observed in this experiment is due to enzyme-catalyzed ketonization, as observed with MhpC (125). In contrast to the relatively equal distribution of phase amplitudes for  $1/\tau_2$  and  $1/\tau_3$  at 492 nm, the amplitude of  $1/\tau_3$  at 270 nm was only  $\sim 10\%$  of the total absorbance change (Table 1). This may be attributed to enzyme-catalyzed decay of HPD, which reduces the amplitude associated with phase 3, and thereby makes  $1/\tau_2$  and  $1/\tau_3$  difficult to resolve at 270 nm. Performing the experiment at 3.2 °C better resolved the two phases at 270 nm. Steady-state analysis revealed that while  $K_m$  was essentially unaffected ( $0.30 \pm 0.08 \mu\text{M}$ ), the lower temperature reduced  $k_{\text{cat}}$  6-fold to  $0.98 \pm 0.06 \text{ s}^{-1}$ . This experiment generated values of  $1/\tau_2$  ( $\sim 10 \text{ s}^{-1}$ ) and  $1/\tau_3$  ( $\sim 1.5 \text{ s}^{-1}$ ) with corresponding amplitudes at 270 nm that matched those at 492 nm (Table 1).

Kinetic experiments were performed in the presence of 20% glycerol to help assign relaxations to bimolecular events. Specifically, increasing solvent viscosity should slow diffusive events that reflect association/dissociation from the enzyme. The presence of glycerol did not affect the steady state kinetic parameters. In contrast, glycerol slowed two of the observed relaxations at 3.2 °C:  $1/\tau_1$ , the rate of formation of  $\text{E:S}^{\text{red}}$ , was reduced from  $\sim 200 \text{ s}^{-1}$  to  $66 \pm 6 \text{ s}^{-1}$ , and  $1/\tau_2$  was reduced by  $\sim 50\%$  at both 270 and 492 nm (Table 1). Even at the decreased rate, the formation of  $\text{E:S}^{\text{red}}$  occurred with an isosbestic point at  $\sim 460 \text{ nm}$ , implying a single step transformation from HOPDA (Figure 14A). Although the reduction in  $1/\tau_2$  may reflect the diffusive release of HPD from the enzyme, it may also arise from the decrease in  $1/\tau_1$ ,<sup>2</sup> and/or possible movement of the

---

<sup>2</sup> The observed relaxations are composed of multiple rate constants, and therefore  $1/\tau_2$  may be influenced by the rate constants for binding. For example, for a two-step reversible reaction,  $1/\tau_1 = (p + q)/2$ ;  $1/\tau_2 = (p - q)/2$ ; where  $p = k_1 + k_{-1} + k_2 + k_{-2}$ ; and  $q = [p^2 - 4(k_1k_2 + k_{-1}k_{-2} + k_1k_{-2})]^{1/2}$  (55).

enzyme ‘lid’ domain, although evidence for the latter has not been obtained. The inverse relationship of solvent viscosity and rate of diffusive product release from an enzyme has been documented. For example, viscosity effects on  $k_{\text{cat}}$  have been used to demonstrate the rate-determining dissociation of the ADP product from protein kinases (128, 129). Finally,  $1/\tau_3$  was not affected by viscosity, suggesting that this relaxation reflects an intramolecular event such as hydrolysis rather than diffusive product release.

Early studies had suggested that the ketonized intermediate may be partially released in MhpC (99, 101), and that this “leakiness” could be related to the half-site occupation observed crystallographically (47). Thus, it is possible that such ‘leakiness’, were it to occur in BphD, could account for the biphasic disappearance of  $\text{E:S}^{\text{red}}$ . Indeed, it has been proposed that the enzyme may bind the substrate in a strained, non-planar conformation to promote ketonization (101). Thus, if  $\text{E:S}^{\text{red}}$  represents either a ketonized or readily ketonizable substrate, it is possible that  $1/\tau_2$  reflects partial dissociation of ketonized HOPDA ( $\text{S}^{\text{k}}$ ) from the enzyme (Figure 15). In such a scenario,  $\text{S}^{\text{k}}$  dissociation and hydrolysis would have similar rate constants ( $k_2 \sim k_3 \sim 25 \text{ s}^{-1}$  at 25 °C), such that 50% of  $\text{E:S}^{\text{red}}$  is turned over to product while 50% is released as  $\text{S}^{\text{k}}$ . Thus, re-enolization of the released  $\text{S}^{\text{k}}$  ( $k_4 \sim 6 \text{ s}^{-1}$ ) would limit the rate of hydrolysis of 50% of the substrate such that  $1/\tau_3 \sim 6 \text{ s}^{-1}$  would comprise 50% of the amplitude of  $\text{E:S}^{\text{red}}$  decay. However,  $1/\tau_2$  exhibits similar behaviour at both 492 nm ( $\text{E:S}^{\text{red}}$  decay) and 270 nm (HPD formation), suggesting that  $\text{E:S}^{\text{red}}$  processing is directly coupled to HPD formation. If  $\text{S}^{\text{k}}$  release occurs,  $\text{E:S}^{\text{red}}$  decay should be faster ( $k_2 + k_3$ ) than HPD formation ( $k_2$ ). Although this suggests that release of  $\text{S}^{\text{k}}$  does not satisfactorily account for the biphasic relaxation, it is also possible that  $\text{S}^{\text{k}}$  absorbs at 270 nm. Thus, other potential origins of the biphasic kinetics, including  $\text{S}^{\text{k}}$  release, were examined as described below.



rate-limiting re-enolization of  $S^k$  in solution may account for the biphasic kinetics observed in the single-turnover stopped-flow experiments, even though it was not supported by the apparent coupling of  $E:S^{\text{red}}$  decay (492 nm) and HPD formation (270 nm) (see above). Significantly, this model predicts a considerable steady state population of  $S^k$ . In an attempt to detect  $S^k$  accumulation during turnover of  $\text{BphD}_{\text{LB400}}$ , HOPDA consumption and benzoate production were monitored in a reaction performed at 25 °C ( $I = 0.1$  M potassium phosphate buffer, pH 7.5). More specifically, HOPDA consumption was monitored by absorbance at 434 nm. As the reaction proceeded, aliquots were removed at intervals corresponding to increments of 10% completion, quenched in acidic solution, and benzoate was quantified by HPLC analysis. At all intervals, the amount of benzoate detected corresponded to the amount of HOPDA consumed within the margin of error ( $\pm 5\%$ ; data not shown). These results indicate that significant amounts of  $S^k$  did not accumulate in solution during turnover. Failure to detect significant quantities of  $S^k$  in solution during turnover suggests two possibilities: (1)  $S^k$  is not released from the enzyme, or (2) the re-enolization of  $S^k$  in solution is faster than release, in which case it could not be responsible for the biphasic kinetics.

### 3.1.3 Deuterium incorporation into HPD

To further investigate the possibility of  $S^k$  release during catalytic turnover and to confirm the stereochemical course of the reaction with native enzyme, the incorporation of deuterium from  $D_2O$  into HPD during the  $\text{BphD}_{\text{LB400}}$ -catalyzed hydrolysis of HOPDA was analyzed. Studies using  $\text{Ht-BphD}_{\text{LB400}}$  (*I30*) have demonstrated that the enzyme stereospecifically incorporates deuterium into the  $H5_E$  position of HPD, but 31% exchange of the  $H5_Z$  hydrogen may be attributable to  $S^k$  release. To minimize non-specific exchange at  $H5_Z$  of HOPDA that might occur via phosphate-catalyzed

ketonization similar to that reported for 2-hydroxymuconate (131), the phosphate buffer concentration was lowered to  $I = 5$  mM. Under these conditions, deuterium exchange at H5 of HOPDA occurred with a half-life of  $\sim 10$  min, which was about twice as fast as exchange into H3. These rates were approximately one-third as fast as at  $I = 100$  mM phosphate. Moreover, sufficient amounts of BphD<sub>LB400</sub> were added to ensure HOPDA hydrolysis was complete in less than 4 min.

Figure 16 shows the <sup>1</sup>H NMR spectrum of HPD from a reaction performed in D<sub>2</sub>O. Peak integration revealed that  $\sim 10\%$  signal loss occurred at H5<sub>Z</sub> during the course of an enzyme-catalyzed reaction. This small amount of deuterium incorporation corresponded to what was observed over a similar time period in the absence of BphD<sub>LB400</sub>. By contrast, almost complete deuterium incorporation occurred at H5<sub>E</sub>, as predicted.<sup>3</sup> Hence the enzyme stereospecifically incorporates a proton at H5<sub>E</sub>, and the non-specific incorporation at H5<sub>Z</sub> can be explained by non-enzymatic exchange prior to enzymatic hydrolysis. If the reaction was allowed to continue after the complete conversion of HOPDA, ketonized HPD ((*E*)-2-oxo-3-pentenoate) appeared in the NMR spectrum (data not shown). Indeed, addition of BphD<sub>LB400</sub> to a solution of HPD confirmed that the enzyme catalyzes ketonization of HPD (section 3.2.3), as reported for MhpC (125).

In summary, three independent experiments indicate that S<sup>k</sup> is not released from the enzyme in significant amounts: (1) single turnover stopped-flow showed matching biphasic behaviour for both HPD formation and E:S<sup>red</sup> decay; (2) the amount of benzoate

---

<sup>3</sup> The reaction contained 1% water (from addition of aqueous BphD), and 2% ethanol (from addition of concentrated HOPDA), thereby causing a small signal from H5<sub>E</sub>.

produced in steady state assays corresponded to the amount of HOPDA hydrolyzed; and (3) deuterium was not incorporated into HPD at H5<sub>Z</sub> above background levels. These results suggest that the BphD<sub>LB400</sub>-catalyzed hydrolysis of HOPDA proceeds via a linear model as opposed to the branched model involving S<sup>k</sup> release initially proposed for MhpC (101).

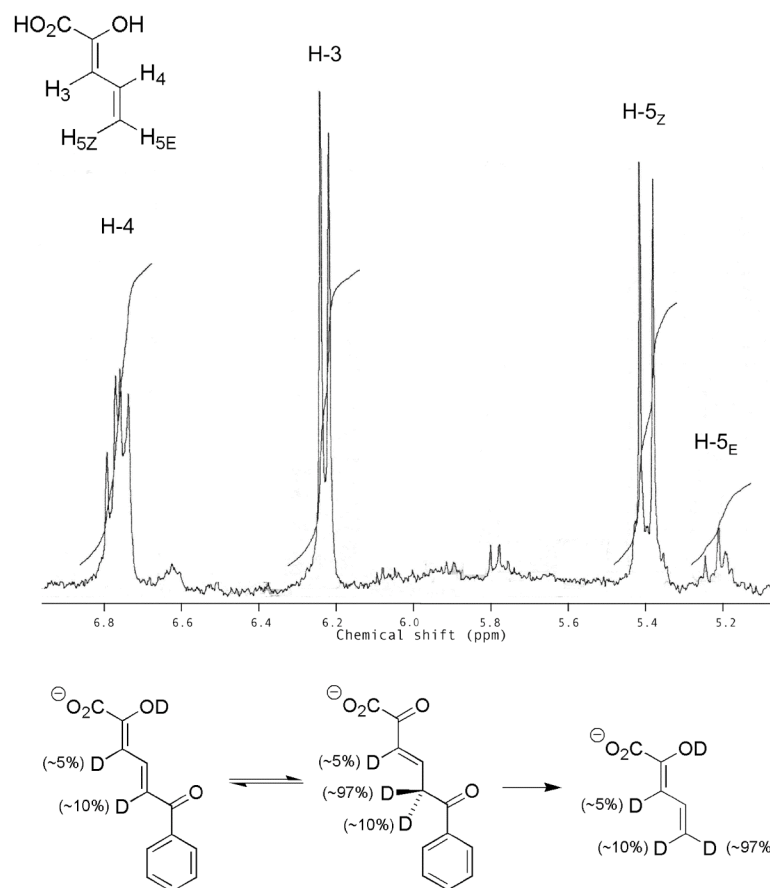


**Figure 16.** *Top:* The <sup>1</sup>H NMR spectrum of HPD generated from BphD<sub>LB400</sub>-catalyzed hydrolysis of HOPDA in 97% D<sub>2</sub>O (potassium phosphate, pD = 7.5, I = 5 mM). Peak integration demonstrates ~10% deuterium incorporation into H5<sub>Z</sub> and almost complete incorporation into H5<sub>E</sub>. *Bottom:* The ~10% non-specific deuterium incorporation into H5<sub>Z</sub> is consistent with non-enzymatic exchange prior to enzymatic catalysis.

### 3.1.4 Product inhibition studies

To help interpret transient state kinetic data, product inhibition studies were performed (potassium phosphate buffer ( $I = 0.1$  M), pH 7.5) under two conditions representative of those used for the single turnover experiments: 1)  $25 \pm 1$  °C, and 2)  $5 \pm 3$  °C, 20% glycerol. In these experiments, inhibition by each product (benzoate and HPD) was examined by steady-state kinetics so as to probe the order of product release. At 25 °C, benzoate was found to competitively inhibit BphD<sub>LB400</sub>-catalyzed hydrolysis of HOPDA with  $K_{ic} = 165 \pm 20$  μM (data not shown). Under these conditions, however, HPD was not sufficiently stable to reliably characterize inhibition. At 5 °C in the presence of 20% glycerol, benzoate also competitively inhibited the BphD<sub>LB400</sub>-catalyzed hydrolysis of HOPDA with  $K_{ic} = 220 \pm 30$  μM (Figure 17A). This result indicates that benzoate competes for the active site of free enzyme, and therefore may be the last product released from the enzyme. Under these same conditions, HPD inhibited the BphD<sub>LB400</sub>-catalyzed hydrolysis of HOPDA in a mixed fashion with  $K_{ic} = 84 \pm 41$  μM,  $K_{iu} = 120 \pm 30$  μM (Figure 17B). This indicates that HPD is released in a step that generates an enzyme species other than that which binds free substrate (132). The competitive component of the mixed inhibition suggests that HPD may also bind to the free enzyme. Consistent with this hypothesis, BphD<sub>LB400</sub> catalyzed the ketonization of HPD (see sections 3.1.1 and 3.2.3). The results should be regarded with some caution as there will inevitably be some ketonized HPD present in the reaction even at low temperature. However, the product inhibition experiments are consistent with a mechanism in which HPD is released prior to benzoate, but the former may re-associate with the free enzyme to undergo ketonization.

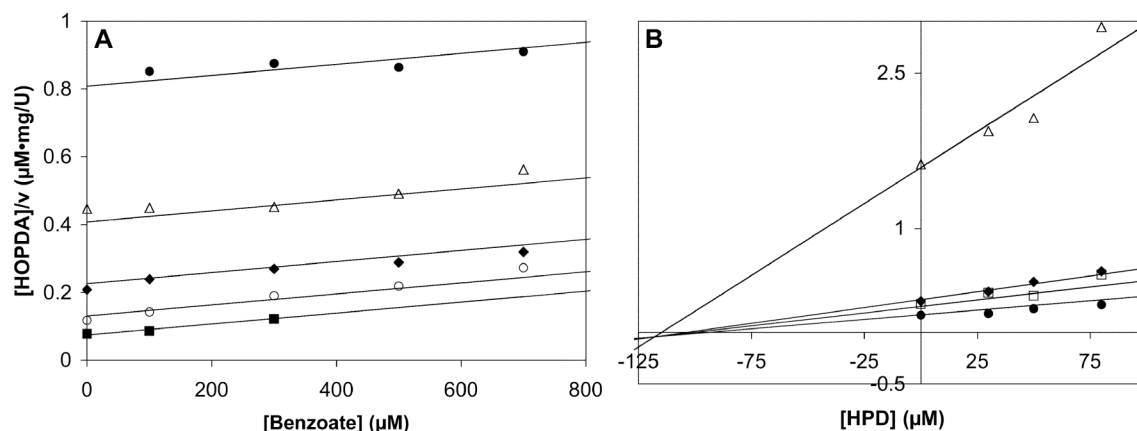


**Figure 17.** Cornish-Bowden plots (132) illustrating the type of inhibition of the BphD<sub>LB400</sub>-catalyzed hydrolysis of HOPDA by reaction products. (A) Inhibition by benzoate described by competitive inhibition ( $K_{ic} = 220 \pm 30 \mu\text{M}$ ;  $K_m = 0.21 \pm 0.02 \mu\text{M}$ ;  $V = 5.9 \pm 0.2 \text{ U/mg}$ ). Reaction rates determined using 0.24 ( $\blacksquare$ ), 0.57 (O), 1.1 ( $\blacklozenge$ ), 2.2 ( $\triangle$ ), and 4.6  $\mu\text{M}$  ( $\bullet$ ) HOPDA. (B) Inhibition by HPD described by mixed inhibition ( $K_{ic} = 84 \pm 41 \mu\text{M}$ ;  $K_{iu} = 120 \pm 30 \mu\text{M}$ ;  $K_m = 0.45 \pm 0.08 \mu\text{M}$ ;  $V = 4.0 \pm 0.2 \text{ U/mg}$ ). Reaction rates were measured using 0.23 ( $\bullet$ ), 0.56 ( $\square$ ), 0.82 ( $\blacklozenge$ ), and 5.9  $\mu\text{M}$  ( $\triangle$ ) HOPDA. Equations describing competitive, uncompetitive, and mixed inhibition were each fit to the data using the least squares, dynamic weighting options of the LEONORA program, and the type of inhibition determined by comparing the quality of fit based on non-random trends in the residuals. The solid lines represent the best fit parameters of the global fit at each HOPDA concentration. Conditions: potassium phosphate buffer ( $I = 0.1 \text{ M}$ ), 20% glycerol, pH 7.5,  $5 \pm 3 \text{ }^\circ\text{C}$ .

## 3.2 Characterization of BphD<sub>LB400</sub> variants

### 3.2.1 General kinetic analysis

Catalytic triad residues His265 and Ser112 were substituted to construct four variants: S112A, S112C, H265A, and S112A/H265A. The extremely low activity of the S112A and S112A/H265A variants, as measured by absorbance at 434 nm, prevented steady-state kinetic measurements. Attempts to measure steady-state kinetic parameters for the S112C variant were confounded by the non-linearity of the progress curves,

indicative of strong product inhibition or enzyme inactivation. The inclusion of 1 mM DTT did not affect the non-linearity, suggesting that the latter was not due to oxidation of Cys112. Nevertheless, estimates of initial velocities at 25 °C generate  $k_{\text{cat}} = 0.27 \pm 0.02 \text{ s}^{-1}$ , and  $K_m = 2.8 \pm 0.6 \text{ }\mu\text{M}$ , and a specificity constant ( $k_{\text{cat}}/K_m = 9.5 \pm 2.2 \times 10^4 \text{ M}^{-1} \text{ s}^{-1}$ ) approximately 240-fold lower than wild type enzyme.

Transformation of HOPDA by H265A could only be detected using large quantities of enzyme ( $\sim 1 \text{ }\mu\text{M}$ ), and the progress curve was biphasic. In an experiment in which 4  $\mu\text{M}$  HOPDA was mixed with 1.3  $\mu\text{M}$  H265A, the first phase could be described by a single exponential decay with a rate constant of  $5.8 (\pm 0.4) \times 10^{-3} \text{ s}^{-1}$ . In Table 2 this is presented as the third rate of decay, or reciprocal relaxation time ( $1/\tau_3$ ), because it is preceded by two events observed by stopped-flow spectrophotometry (section 3.2.2). The slope of the linear second phase approximately doubled upon increasing the H265A concentration to 2.6  $\mu\text{M}$ , consistent with this phase representing steady-state turnover. By contrast, doubling enzyme concentration did not affect the value of  $1/\tau_3$ , but doubled its amplitude. This apparent burst is consistent with first order decay of an E:S complex followed by steady-state turnover. Curiously, the amplitude of the first phase corresponded to only  $9 (\pm 3) \%$  of the total enzyme added, suggesting only this fraction of the H265A active sites were functional. Similar behaviour was observed in stopped-flow experiments (section 3.2.2). Correcting for the active fraction of enzyme provides a rate of  $(9 \pm 2) \times 10^{-4} \text{ s}^{-1}$  for the steady state phase, which is about half of the  $k_{\text{cat}}$  measured for the H265A variant of Ht-BphD<sub>LB400</sub> (105). This is in reasonable agreement considering the current experiments were performed using a substrate concentration below the  $K_m$  of 37  $\mu\text{M}$  measured for Ht-BphD<sub>LB400</sub>.

### 3.2.2 Stopped-flow kinetic analysis

To better characterize the catalytic impairment of the variants, stopped-flow spectrophotometry was employed under single turnover conditions ( $E = 8 \mu\text{M}$ ,  $S = 4 \mu\text{M}$ ) at  $25 \text{ }^\circ\text{C}$ . The S112A variant generated an  $E:S^{\text{red}}$  intermediate with a spectrum similar to that of the transiently observed  $E:S^{\text{red}}$  intermediate in wild type (WT) BphD<sub>LB400</sub>. The spectrum of  $E:S^{\text{red}}$  was even more red-shifted and more intense in S112A ( $\lambda_{\text{max}} = 506 \text{ nm}$ ; Figure 18A) than in WT ( $\lambda_{\text{max}} = 492 \text{ nm}$ , Figure 18D), but maintained the same spectral shape featuring two prominent absorption maxima (506 and 483 nm). In the S112A variant, the free HOPDA enolate band (434 nm) was transformed directly to  $E:S^{\text{red}}$ , as indicated by the isosbestic point at 461 nm, in three phases (Table 2). Most of this transformation (85% of the amplitude) occurred very rapidly ( $1/\tau_1 \sim 500 \text{ s}^{-1}$ ), and was followed by two slower relaxations (76 and  $0.92 \text{ s}^{-1}$ ) of smaller amplitude. The latter events may reflect subtle conformational changes that facilitate more complete formation of  $E:S^{\text{red}}$ , or perhaps binding of other isomers of HOPDA from solution. Moreover,  $E:S^{\text{red}}$  decayed extremely slowly in S112A, and was effectively trapped as an orange-coloured complex (Figure 18C). The half-life of this complex (S112A =  $25 \mu\text{M}$ , HOPDA =  $5 \mu\text{M}$ ), determined by monitoring its absorbance at 506 nm, was 4.4 h at  $25 \text{ }^\circ\text{C}$ . In summary, the S112A variant generates  $E:S^{\text{red}}$  at a similar rate to WT enzyme, indicating that Ser112 does not catalyze the formation of this intermediate.

In contrast to S112A, neither H265A nor S112A/H265A accumulated the  $E:S^{\text{red}}$  intermediate, implying that His265 is required for its formation. Attempts to rescue  $E:S^{\text{red}}$  formation in the double variant with imidazole (1 – 5 mM) were unsuccessful. Instead, the free HOPDA enolate band ( $\lambda_{\text{max}} = 434 \text{ nm}$ ) underwent an increase in intensity and a slight blue shift ( $\lambda_{\text{max}} = 432 \text{ nm}$ ; Figure 18B). Because the 2-OH moiety of HOPDA has a  $pK_a$  of 7.3, the substrate exists as a mixture of enol ( $\lambda_{\text{max}} = 341 \text{ nm}$ ) and

enolate ( $\lambda_{\max} = 434$  nm) forms in solution at pH 7.5. Thus, the new species ( $\lambda_{\max} = 432$  nm) formed in the H265A variants may be most reasonably assigned as an enzyme-bound HOPDA enolate (E:S<sup>e</sup>). Indeed, in S112A/H265A, the molar absorptivity of E:S<sup>e</sup> was comparable to that of fully deprotonated HOPDA in solution.<sup>4</sup> For this mutant, E:S<sup>e</sup> was formed in three phases (Table 2), with the first and largest (69% of the amplitude) occurring most rapidly ( $1/\tau_1 = 220$  s<sup>-1</sup>), followed by two smaller and slower phases ( $1/\tau_2 = 22$  s<sup>-1</sup>,  $1/\tau_3 = 0.34$  s<sup>-1</sup>). As in S112A, the multiphasic formation of this intermediate may reflect conformational changes or delayed binding of different forms of HOPDA in solution. Although subsequent decay of E:S<sup>e</sup> was not observed on the time scale of the stopped-flow experiment, the half-life was estimated to be ~220 h by spectrophotometrically monitoring E:S<sup>e</sup> decay over a 24 h period.

In comparison to the apparently complete formation of E:S<sup>e</sup> by S112A/H265A, the H265A variant only partially formed this bound HOPDA enolate under these conditions: when [H265A] = 8  $\mu$ M and [HOPDA] = 4  $\mu$ M, the amplitude of the total absorbance increase at 434 nm was only 25% of the same signal observed using S112A/H265A. No absorbance increase was observed at the wavelengths corresponding to the expected enol absorption band (~340 nm), suggesting that the enzyme does not bind the enol. Increasing the concentration of H265A to 32  $\mu$ M (4  $\mu$ M HOPDA) resulted in the same spectrum as observed in S112A/H265A, suggesting that only ~12% of the active sites in H265A generated the enolate, as observed in the experiments described in section 3.2.1. This phenomenon was observed in two different preparations of H265A. With 32  $\mu$ M H265A, the formation of E:S<sup>e</sup> was biphasic (Table 2), and again the first

---

<sup>4</sup> The HOPDA enol has a pK<sub>a</sub> of 7.3 (1). Hence the >99% deprotonated form at pH 9.5 (50 mM Na-CHES, 25 °C) has a molar absorptivity of 40.1 mM<sup>-1</sup> cm<sup>-1</sup> at 434 nm.

phase was much larger (82%) and more rapid ( $1/\tau_1 = 78 \text{ s}^{-1}$ ) than the second phase ( $1/\tau_2 = 1.3 \text{ s}^{-1}$ ). The initial phase is probably slower in H265A than S112A/H265A because fewer active sites are apparently present in the former (*i.e.*  $32 \mu\text{M} \times \sim 12\%$  active sites =  $\sim 4 \mu\text{M}$  H265A, compared with  $8 \mu\text{M}$  S112A/H265A). As described in section 3.2.1, the E:S<sup>e</sup> intermediate slowly decayed ( $1/\tau_3 = 0.0058 \text{ s}^{-1}$ ) prior to an apparent steady-state phase ( $0.0009 \text{ s}^{-1}$ ).

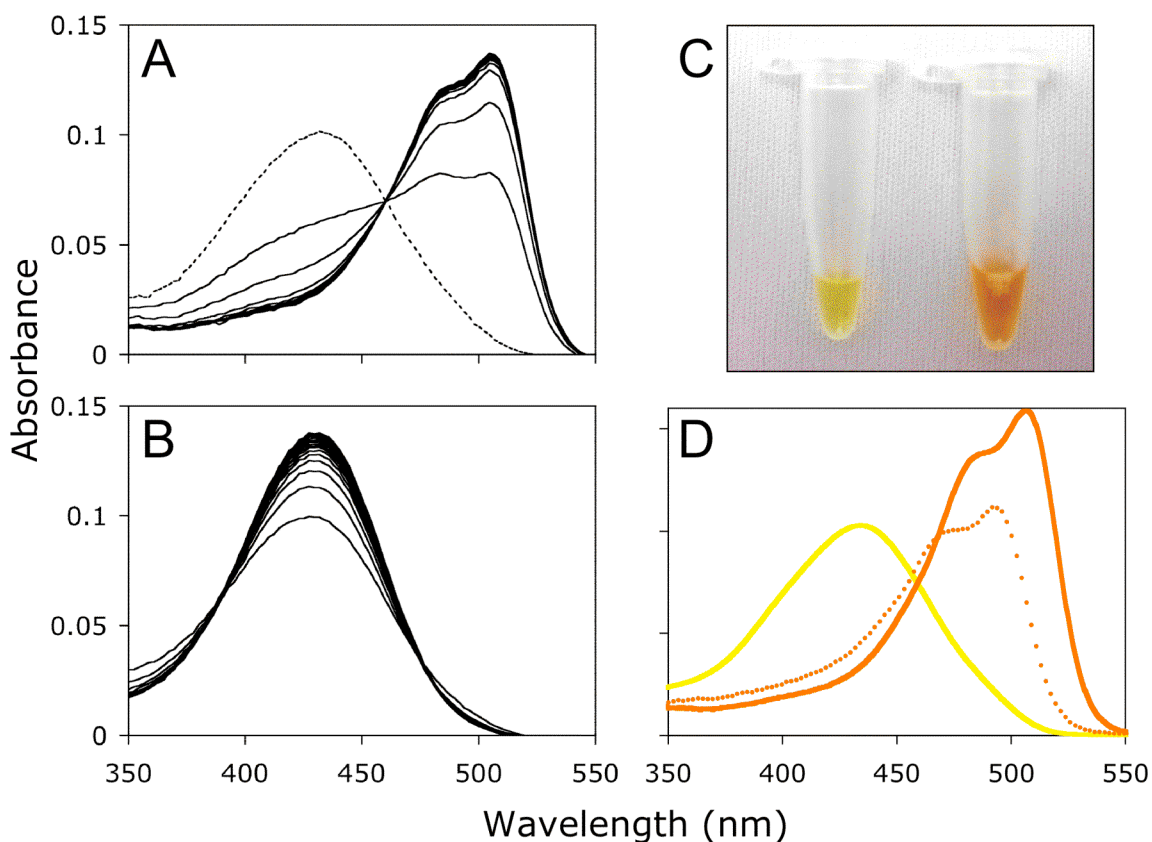


**Figure 18.** Absorption spectra of intermediates arising during the hydrolysis of HOPDA by BphD<sub>LB400</sub> variants. A) Spectra observed upon mixing 3.9 μM HOPDA (dashed line overlay) with 8 μM S112A. Spectra were recorded 1.1, 3.7, 8.8, 11, 14, 17, 19, 32, and 50 ms after mixing. The isosbestic point occurs at 461 nm. B) Spectra observed upon mixing 3.4 μM HOPDA with 8 μM S112A/H265A. Spectra were recorded 3.7, 6.2, 8.8, 11, 14, and every ~3 ms thereafter to 58 ms after mixing. C) Eppendorf tubes containing HOPDA (140 μM) mixed with 150 μM of either S112A/H265A (left, yellow) or S112A (right, orange). D) Spectral comparison of 4 μM HOPDA (solid yellow line), the S112A:HOPDA complex (solid orange line) and the E:S<sup>red</sup> intermediate (dotted orange line) observed ~20 ms after mixing 8 μM wild type BphD with 4 μM HOPDA at 3.2 °C. Spectral intensities of the complexes were corrected based on  $K_d$  or rate constants. Spectra were recorded using potassium phosphate buffer ( $I = 0.1$  M, pH 7.5) at 25 °C unless otherwise noted.

**Table 2.** Kinetic data for BphD<sub>LB400</sub> alanine variants<sup>a</sup>

| BphD <sub>LB400</sub> Variant | 1/ $\tau_1$                 | 1/ $\tau_2$               | 1/ $\tau_3$                                 |
|-------------------------------|-----------------------------|---------------------------|---|
| S112A/H265A                   | 220 s <sup>-1</sup> (69%)   | 22 s <sup>-1</sup> (22%)  | 0.34 s <sup>-1</sup> (9%)                   |
| H265A                         | 78 s <sup>-1</sup> (82%)    | 1.3 s <sup>-1</sup> (18%) | 0.0058 s <sup>-1</sup> (-100%) <sup>b</sup> |
| S112A                         | ~500 s <sup>-1</sup> (-85%) | 76 s <sup>-1</sup> (-11%) | 0.92 s <sup>-1</sup> (-4%)                  |

<sup>a</sup>Stopped-flow data at 434 nm are reported as reciprocal relaxation times for each of the 3 phases (1/ $\tau_n$ ), except H265A, in which only the first two phases were studied by stopped-flow. Concentrations: [S112A], [S112A/H265A] = 8  $\mu$ M; [H265A] = 32  $\mu$ M; HOPDA = 4  $\mu$ M. Values in parentheses for stopped-flow data represent the percent of the total absorbance change (amplitude) in either the positive (absorbance increase) or negative (absorbance decrease) direction. Standard errors are no greater than 20%.

<sup>b</sup>Measured using a Cary 5000 spectrophotometer as an exponential decay in absorbance at 434 nm.

### 3.2.3 Tautomerization of HPD by variant enzymes

To probe the ability of the BphD<sub>LB400</sub> variants to catalyze tautomerization, their respective abilities to catalyze the transformation of HPD to (*E*)-2-oxo-3-pentenoate were investigated. The tautomerization of HPD is observed as decay in absorbance at 270 nm and occurs non-enzymatically in aqueous solution at a low rate. Wild-type and S112A catalyzed the tautomerization of HPD (~14  $\mu$ M) with specific activities of  $0.47 \pm 0.01$  U/mg and  $0.082 \pm 0.013$  U/mg respectively. The slower S112A reaction was detectable (0.0067  $\mu$ mol/min) over background HPD decay (0.0011  $\mu$ mol/min). By contrast, neither H265A nor S112A/H265A detectably catalyzed this tautomerization. Thus, His265 is apparently necessary for catalyzing tautomerization of HPD, and Ser112 plays a less crucial role (Figure 19), although it is possible that HPD does not bind to H265A variants.

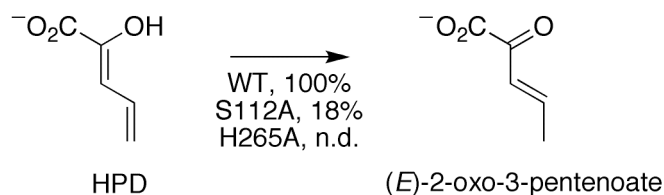


**Figure 19.** The catalytic triad residue His265 of BphD<sub>LB400</sub> is required for HPD tautomerization.

### 3.3 The basis for inhibition by 3-Cl HOPDA

#### 3.3.1 Steady-state kinetics

To assess the basis of the inhibition of BphD<sub>LB400</sub> by 3-Cl HOPDA, the enzyme-catalyzed hydrolysis of 3,10-diF HOPDA and 3-Me HOPDA were studied using steady-state kinetics. The 10-fluoro substituent is not expected to greatly affect catalysis, because HOPDAs with small, electron-withdrawing substituents (e.g. -Cl, -CF<sub>3</sub>) at this position are hydrolyzed by BphD<sub>LB400</sub> with  $k_{\text{cat}}$  values within 25% of that for HOPDA (41, 110). Significantly, reduction of the volume of the electronegative 3-substituent by 40% upon chlorine-to-fluorine substitution resulted in a 150-fold increase in  $k_{\text{cat}}$  (Table 3), indicating that larger 3-substituents interfere with catalysis. This conclusion was supported by the observation that the substrate with the largest 3-substituent, 3-Me HOPDA, had the lowest apparent  $k_{\text{cat}}$  (Table 3). Although a  $K_{\text{m}}$  value was reported for 3-Cl HOPDA (41),  $K_{\text{m}}$  was not determined for 3-Me HOPDA due to a combination of lower activity, lower molar absorptivity, and higher background decay rates, which together prevented reliable initial rate measurements at low substrate concentrations. Finally, the stability of HOPDAs in the enzyme reaction buffer (Table 3) revealed no obvious correlation between either the electronic effects of the substituents and the

nonenzymatic decomposition, or between the nonenzymatic and enzymatic reactions. In conclusion,  $k_{\text{cat}}$  was strongly anticorrelated with the volume of the substituent at C3 and uncorrelated with electronegativity over the series of HOPDAs studied, suggesting that turnover is largely dictated by steric, not electronic, factors.

**Table 3.** Properties of 3-substituted HOPDAs and the steady-state parameters for their hydrolysis by BphD<sub>LB400</sub>.<sup>a</sup>

| 3-X HOPDA<br>(X) | Half-life<br>(h) | Electro-<br>negativity <sup>b</sup> | Volume <sup>c</sup><br>(Å <sup>3</sup> ) | $k_{\text{cat}}$<br>(s <sup>-1</sup> ) | $K_{\text{m}}$<br>(μM) | $k_{\text{cat}}/K_{\text{m}}$<br>(μM <sup>-1</sup> s <sup>-1</sup> ) |
|------------------|------------------|-------------------------------------|--|--|------------------------|--|
| H                | 58 <sup>d</sup>  | 2.2                                 | 7.2                                      | 6.5                                    | 0.2                    | 32   |
| F                | 11               | 4.1                                 | 13.3                                     | 1.4                                    | 4.8                    | 0.29   |
| Cl <sup>d</sup>  | 504              | 2.8                                 | 22.5                                     | 0.0089                                 | 0.54                   | 0.016  |
| Me               | 30               | 2.3 <sup>e</sup>                    | 28.4                                     | 0.0036 <sup>f</sup>                    | ND                     | ND   |

<sup>a</sup> Standard errors are less than 15%.

<sup>b</sup> From reference (1)

<sup>c</sup> From reference (133).

<sup>d</sup> From reference (41).

<sup>e</sup> From reference (134)

<sup>f</sup> Estimated from initial rate measurements at high substrate concentrations ( $[S] \gg K_{\text{m}}$ ).  
ND = not determined.

### 3.3.2 Stopped-flow kinetics

To better elucidate the influence of 3-substituents on catalysis, stopped-flow spectrophotometric studies were conducted to resolve individual catalytic steps. In contrast to the BphD<sub>LB400</sub>:HOPDA reaction, E:S<sup>red</sup> did not accumulate when 3-Cl HOPDA was used as a substrate (Figure 20A). Under single turnover conditions ( $[\text{BphD}_{\text{LB400}}] = 8 \mu\text{M}$ ,  $[\text{3-Cl HOPDA}] = 4 \mu\text{M}$ ), an initial decrease ( $1/\tau_1 = 15 \text{ s}^{-1}$ ) occurred

at the absorbance maximum of 3-Cl HOPDA (432 nm) (Table 4). This decay corresponded to a ~20% loss in absorbance, and occurred together with a slight blue shift to 427 nm. The similarity of this  $\lambda_{\text{max}}$  to that of the 3-Cl HOPDA enolate band in solution suggests that this initial event may correspond to formation of an initial enzyme-bound HOPDA enolate, E:S<sup>e</sup>. However, in contrast to the absorbance increase assigned to E:S<sup>e</sup> formation during the reaction of HOPDA with H265A variants (section 3.2.2), the molar absorptivity of 3-Cl HOPDA decreases upon binding to the enzyme. Because 3-Cl HOPDA exists primarily as the enolate in solution ( $\text{p}K_{\text{a}} = 6.3$ ), there is little absorbance increase available from deprotonation, implying that the observed absorbance decrease reflects binding to the enzyme. This E:S<sup>e</sup> species very slowly ( $1/\tau_2 = 0.0077 \text{ s}^{-1}$ ) decayed at a rate that matches the previously measured  $k_{\text{cat}}$  value (Table 3).

**Table 4.** Reciprocal relaxation times and amplitudes for single turnover reactions monitored by stopped-flow spectrophotometry at the substrate absorption maxima.<sup>a</sup>

| Substrate      | BphD <sub>LB400</sub> Variant | Phase 1 (amplitude)        | Phase 2 (amplitude)           | Phase 3 (amplitude)         |
|----------------|-------------------------------|----------------------------|-------------------------------|-----------------------------|
| 3-Cl HOPDA     | WT                            | 15 s <sup>-1</sup> (0.031) | 0.0077 s <sup>-1</sup> (0.13) |                             |
|                | S112A                         | 26 s <sup>-1</sup> (0.026) | 0.55 s <sup>-1</sup> (-0.001) |                             |
| 3,10-diF HOPDA | WT                            | 51 s <sup>-1</sup> (0.051) | 7.6 s <sup>-1</sup> (0.028)   | 1.3 s <sup>-1</sup> (0.070) |
|                | S112A                         | 88 s <sup>-1</sup> (0.055) | 1.1 s <sup>-1</sup> (-0.001)  |                             |

<sup>a</sup>The 3-Cl HOPDA reaction was monitored at 432 nm; 3,10-diF HOPDA at 438 nm. Standard errors are no more than 15%.

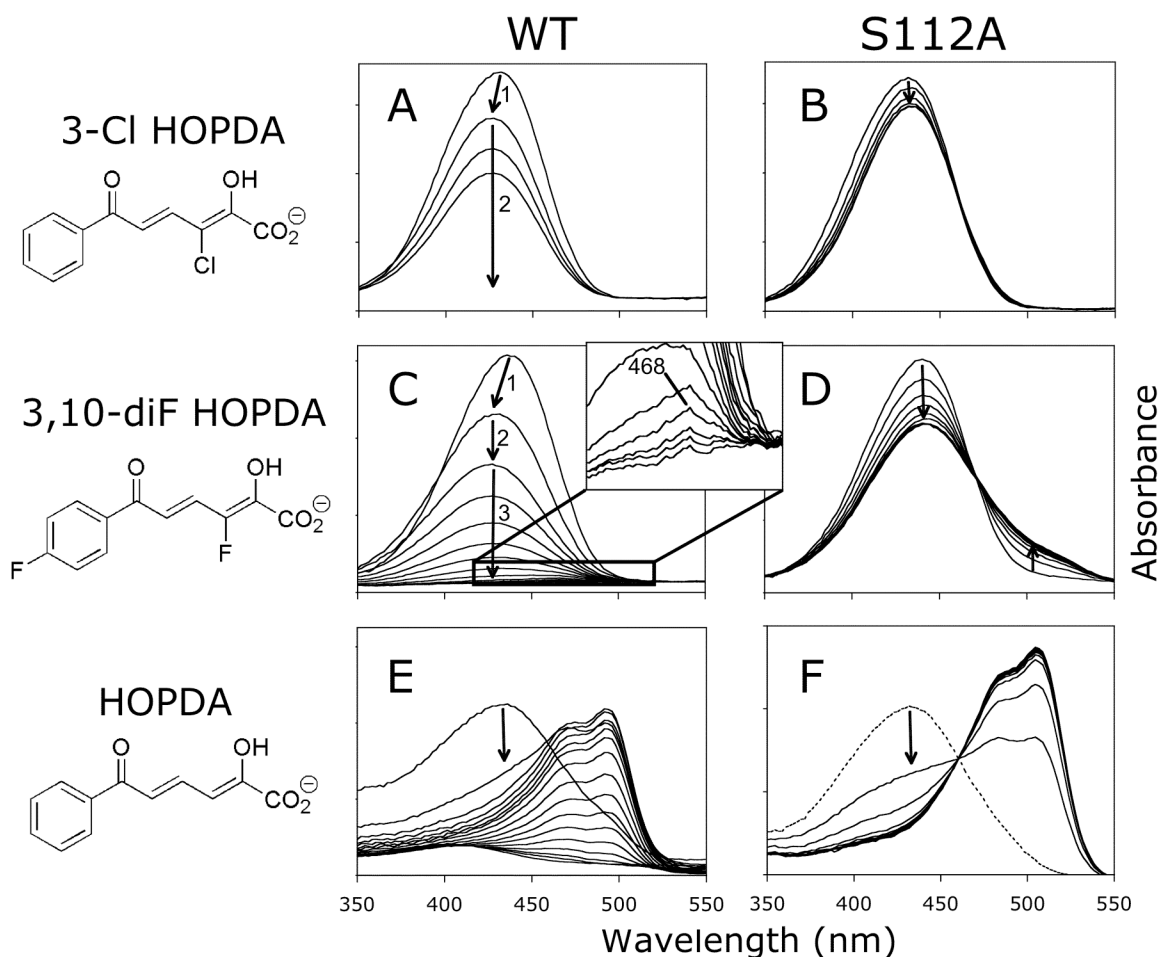


**Figure 20.** Time-resolved spectra from single turnover (E = 8  $\mu$ M; S = 4  $\mu$ M) stopped-flow spectrophotometry show that increasing the size of the HOPDA 3-substituent limits accumulation of the high wavelength-absorbing E:S<sup>red</sup> intermediate. Reactions are shown for wild type BphD<sub>LB400</sub> (WT, left panels) and S112A (right panels) with 3-Cl HOPDA (top), 3,10-diF HOPDA (middle), and HOPDA (bottom). (A) Wild type + 3-Cl HOPDA; (B) S112A + 3-Cl HOPDA; (C) wild type + 3,10-diF HOPDA; (D) S112A + 3,10-diF HOPDA; (E) wild type + HOPDA, from section 3.1.1; and (F) S112A + HOPDA, from section 3.2.2. Arrows indicate the direction of absorbance changes with time. Separate relaxations are indicated by numbered arrows, and correspond to the phases described in Table 4.

In an attempt to observe E:S<sup>red</sup> accumulation for 3-Cl HOPDA, the S112A variant was used. This variant catalyzes E:S<sup>red</sup> formation at the same rate as WT BphD, but possesses severely impaired turnover (section 3.2). For 3-Cl HOPDA, E:S<sup>red</sup> did not detectably accumulate in this variant (Figure 20B). Similar to the behaviour of WT, S112A caused an initial decrease ( $1/\tau_1 = 26 \text{ s}^{-1}$ ) corresponding to ~15% loss in 3-Cl HOPDA absorbance (Table 4), albeit without a correlated blue shift. This was followed by a very small (<1% of total 3-Cl HOPDA absorbance) and relatively slow ( $1/\tau_2 = 0.55 \text{ s}^{-1}$ ) increase in absorbance at 432 nm. Subsequent decay was not detected on the time scale examined (<1 min). In summary, an E:S<sup>red</sup> species was not detected in either WT or S112A, suggesting that an E:S<sup>e</sup> complex is the predominant enzyme-bound species, and that catalysis is limited by formation of E:S<sup>red</sup>.

The improved turnover of 3,10-diF HOPDA compared to 3-Cl HOPDA (Table 3) implies that 3,10-diF HOPDA may more readily access the catalytically relevant E:S<sup>red</sup> intermediate. During the reaction of BphD with 3,10-diF HOPDA, a relatively weak signal was observed for an intermediate with a red-shifted absorption spectrum ( $\lambda_{\text{max}} \sim 468 \text{ nm}$ , Figure 20C) that may correspond to E:S<sup>red</sup>. The low intensity of this spectrum suggests that only a small amount of E:S<sup>red</sup> accumulates and thus its formation is only partially rate-limiting. Decay of the signal at the absorbance maximum of 3,10-diF HOPDA (438 nm) can be described by three phases (Table 4): (i) a loss in absorbance ( $1/\tau_1 = 51 \text{ s}^{-1}$ ) analogous to the initial decay in the 3-Cl HOPDA reaction, whereby a slightly blue-shifted feature ( $\lambda_{\text{max}} = 427 \text{ nm}$ ) was generated together with a ~30% loss in absorbance; (ii) a small (20% of total absorbance decrease) second decay ( $1/\tau_2 = 7.6 \text{ s}^{-1}$ ) during which E:S<sup>red</sup> was observed ( $\lambda_{\text{max}} \sim 468 \text{ nm}$ ), and (iii) a final phase,  $1/\tau_3 = 1.3 \text{ s}^{-1}$ .

Although an E:S<sup>red</sup> intermediate ( $\lambda_{\text{max}} \sim 517 \text{ nm}$ ) accumulated to a greater extent in S112A than in wild type, stoichiometric formation of this species was not observed

using 3,10-diF HOPDA (Figure 20D). The reaction proceeds quickly ( $1/\tau_1 = 90 \text{ s}^{-1}$ ), but consumes only ~35% of the substrate based on absorbance. This is followed by a minor relaxation of <1% total absorbance, which occurs as an increase at 438 nm ( $1/\tau_2 = 1.1 \text{ s}^{-1}$ ) and a corresponding decrease at 517 nm. The incomplete  $E:S^{\text{red}}$  formation suggests that the 3-fluoro substituent destabilizes  $E:S^{\text{red}}$  relative to the  $E:S^{\text{e}}$  complex and/or free substrate.

In summary, increasing the size of the 3-substituent appears to slow  $E:S^{\text{red}}$  formation. Fluoro-substitution apparently decreases turnover by similarly favouring  $E:S^{\text{red}}$  and a nonproductive  $E:S^{\text{e}}$  binding mode. In contrast, turnover is more severely impaired by chloro-substitution, which may preferentially adopt the  $E:S^{\text{e}}$  binding mode relative to  $E:S^{\text{red}}$ .

### 3.4 Characterization of the hydrolysis reaction

#### 3.4.1 BphD<sub>LB400</sub> catalyzes alcoholysis

To further probe the reaction mechanism of MCP hydrolases, the ability of BphD<sub>LB400</sub> to utilize small primary alcohols as exogenous nucleophiles was tested. Under standard conditions ( $I = 0.1 \text{ M}$  potassium phosphate, pH 7.5, 25 °C) in the presence of 1% (v/v) alcohol and 50  $\mu\text{M}$  HOPDA, the enzyme generated benzoyl esters from methanol, ethanol, and *n*-propanol (Figure 21).

#### 3.4.2 Different substrates generate a similar acid:ester product ratio

The competing alcoholysis of HOPDA provides an opportunity to distinguish nucleophilic and general base mechanisms for BphD<sub>LB400</sub>. The nucleophilic mechanism predicts that hydrolysis of an activated ester such as *p*-nitrophenyl benzoate (pNPB)

should proceed via the same benzoyl-enzyme intermediate as HOPDA. The presence of this common intermediate, irrespective of origin, should be detectable by its similar subsequent reactivity. Specifically, both substrates should generate the same acid-to-ester product ratio due to identical partitioning of the intermediate between water and methanol. In contrast, the absence of a common intermediate in the general base mechanism would not necessarily result in similar product ratios.

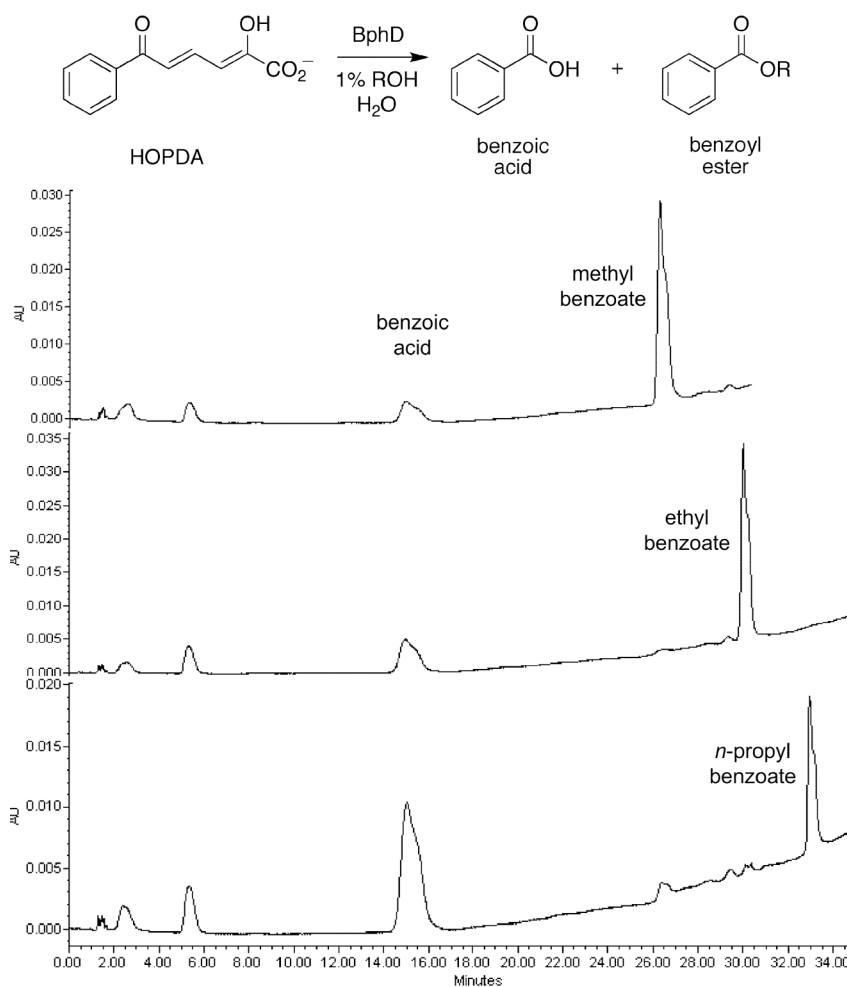


**Figure 21.** HPLC chromatograms of BphD<sub>LB400</sub>-catalyzed hydrolysis of HOPDA (50  $\mu$ M) in the presence of 1% (v/v) methanol, ethanol, or *n*-propanol.

Product ratios generated from each substrate were measured by HPLC analysis. As expected, BphD<sub>LB400</sub> hydrolyzed pNPB to yield *p*-nitrophenol and benzoate (Figure 22A). A peak corresponding to methyl benzoate appeared when the reaction was run in the presence of 25 mM methanol, and the ratio of peak areas of benzoic acid to methyl ester was  $0.80 \pm 0.04$  (Figure 22B). This is similar to the ratio ( $0.79 \pm 0.04$ ) found for the reaction with HOPDA (Figure 22C). The similar product ratios suggest that hydrolysis of each substrate proceeds via a common intermediate. Control reactions showed that BphD did not significantly catalyze either methyl benzoate hydrolysis or formation under the same experimental conditions. Methyl benzoate formation was not detectable when 10 – 300  $\mu$ M of benzoate were incubated with 0.1 – 5% methanol and 12 nM BphD for 1 min, the same timescale of the experiments with HOPDA or pNPB. Similarly, after a 1 min incubation of 10  $\mu$ M methyl benzoate with 12 nM BphD, ~1% of the substrate was hydrolyzed.

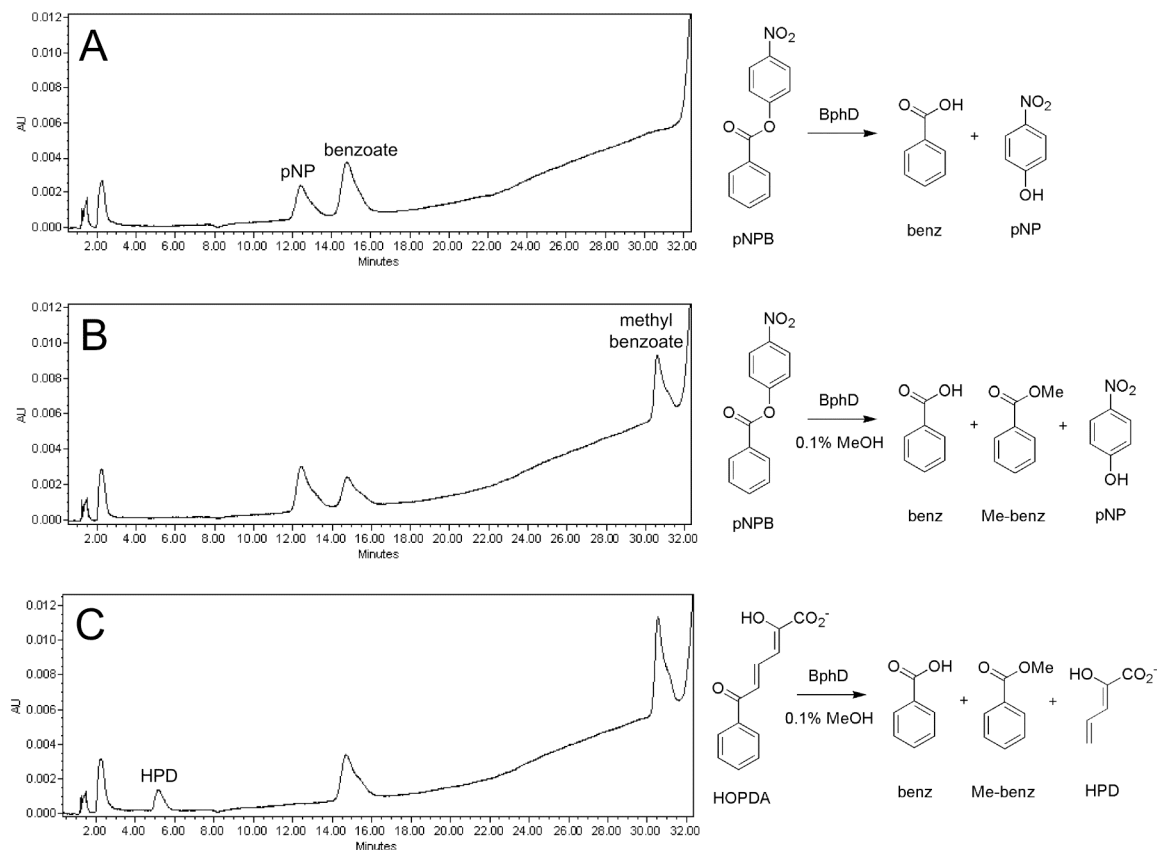


**Figure 22.** HPLC chromatograms illustrating the products of BphD<sub>LB400</sub>-catalyzed conversion of pNBP and HOPDA in the presence of methanol. A) pNBP ( $12 \pm 3 \mu\text{M}$ ) is hydrolyzed to pNP and benzoic acid by BphD<sub>LB400</sub>. B) In the presence of 0.1% (v/v) methanol, pNBP hydrolysis generates a similar ratio (0.8:1) of peak areas for benzoic acid and methyl benzoate. C) The same product ratio is observed for the hydrolysis of HOPDA ( $14 \pm 2 \mu\text{M}$ ) in the presence of methanol. All reactions included 0.1% acetone (solvent for pNBP), observed as a peak at 2.2 min.

### 3.4.3 HOPDA and pNBP are hydrolyzed with similar $k_{\text{cat}}$ values

To further investigate the role of a common intermediate in the BphD<sub>LB400</sub>-catalyzed hydrolysis of HOPDA and pNBP, the steady-state kinetic parameters of the latter were evaluated. At 25 °C in potassium phosphate buffer ( $I = 0.1 \text{ M}$ , pH 7.5, 0.2% acetone) the hydrolysis of pNBP obeyed Michaelis-Menten kinetics (Figure 23). A fit of

the Michaelis-Menten equation to the data yielded  $k_{\text{cat}} = 6.3 \pm 0.5 \text{ s}^{-1}$  and  $K_{\text{m}} = 0.34 \pm 0.02 \text{ }\mu\text{M}$ . The value for  $k_{\text{cat}}$  is similar to that of HOPDA ( $k_{\text{cat}} = 6.5 \pm 0.5 \text{ s}^{-1}$ ), implying that both substrates are hydrolyzed via a common intermediate whose breakdown is rate-determining.

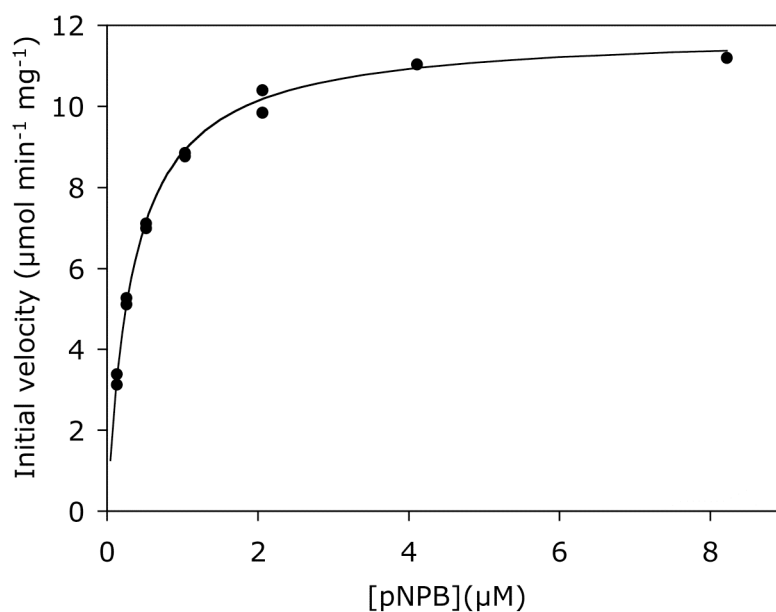


**Figure 23.** Steady-state hydrolysis of pNPB by BphD<sub>LB400</sub>. The line represents a best fit of the Michaelis-Menten equation to the data, yielding fitted parameters of  $V = 12 \pm 1 \text{ U/mg}$  and  $K_{\text{m}} = 0.34 \pm 0.02 \text{ }\mu\text{M}$ . Conditions: potassium phosphate ( $I = 0.1 \text{ M}$ , pH 7.5), 0.2% (v/v) acetone, 25 °C.

### 3.4.4 Steady-state kinetic analysis of nucleophile partitioning for HOPDA

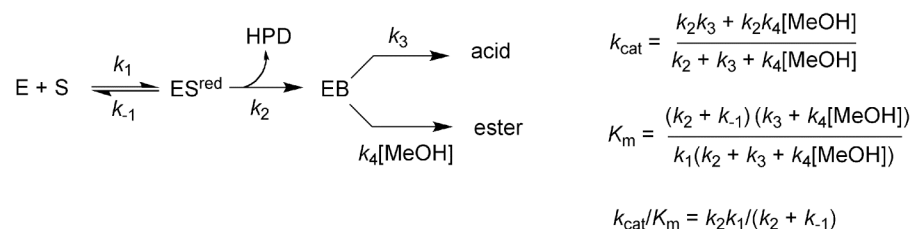
The mechanism may be further probed by examining the dependence of steady-state parameters on methanol concentration. The experimentally-determined values presented in Table 5 demonstrate that both  $k_{\text{cat}}$  and  $K_m$  increase with methanol concentration, but  $k_{\text{cat}}/K_m$  does not.

To evaluate the significance of this result with respect to distinguishing general base and nucleophilic mechanisms, the data can be compared to values predicted from kinetic models for each mechanism. In a nucleophilic mechanism (Figure 24A), the  $\text{E:S}^{\text{red}}$  intermediate may undergo one-step ketonization/acylation to yield the benzoyl-enzyme ( $\text{E:B}$ ), which then undergoes hydrolysis or methanolysis. In the general base mechanism (Figure 24B), the decay of  $\text{E:S}^{\text{red}}$  proceeds first to a discrete keto-intermediate ( $\text{E:S}^{\text{k}}$ ) prior to hydrolysis. Steady-state expressions have been derived for partitioning between methanol and water in both mechanisms (Figure 24).

For the nucleophilic mechanism, the equation for methanol-dependence of  $k_{\text{cat}}$  (Figure 24A) can be fit to the data, yielding  $k_2 = 28 \pm 2 \text{ s}^{-1}$ ,  $k_3 = 8.3 \pm 2.6 \text{ s}^{-1}$ , and  $k_4 = 230 \pm 80 \text{ M}^{-1} \text{ s}^{-1}$  (Figure 25). An essentially indistinguishable fit could be obtained for the general base mechanism with values of  $k_2 = 28 \pm 5 \text{ s}^{-1}$ ,  $k_{-2} = 11 \text{ s}^{-1}$ ,  $k_3 = 11 \text{ s}^{-1}$ , and  $k_4 = 310 \text{ M}^{-1} \text{ s}^{-1}$ . Indeed, the  $k_{\text{cat}}$  values calculated from either mechanism differ from one another by less than 0.3%. These rate constants enable calculation of  $k_{\text{cat}}$  values for both acid and ester formation, using the first and second terms of the  $k_{\text{cat}}$  equations of Figure 24, respectively. For example,  $k_{\text{cat}}$  for hydrolysis in the nucleophilic mechanism can be described by  $k_2 k_3 / (k_2 + k_3 + k_4 [\text{MeOH}])$ , and methanolysis by  $k_2 k_4 [\text{MeOH}] / (k_2 + k_3 + k_4 [\text{MeOH}])$ . The relative  $k_{\text{cat}}$  values for hydrolysis and methanolysis allow prediction of the expected product ratios at each methanol concentration (Table 5). For both models, at

25 mM methanol (0.1% v/v), BphD<sub>LB400</sub> is predicted to catalyze methanolysis 40% of the time, and 87% at 250 mM methanol. Although the product peaks were not quantified via a standard curve, respective values of 55% and 83% are obtained assuming the same molar absorptivity for benzoate and methyl benzoate (as expected with no extension of the chromophore (135)), which is in reasonable agreement with the predicted values. Thus, both models predict the same effect of methanol on  $k_{\text{cat}}$  and the observed product ratios.

**A) Nucleophilic mechanism (benzoyl-enzyme)**



**B) General base mechanism (*gem*-diol)**

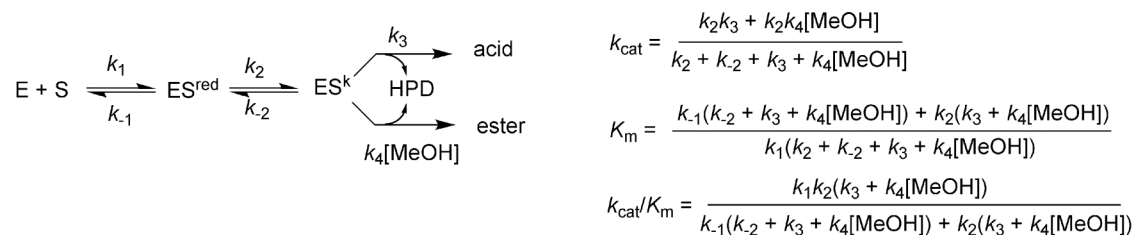


**Figure 24.** Kinetic schemes and steady-state expressions for A) nucleophilic and B) general base mechanisms of BphD<sub>LB400</sub>.

Similarly, the data do not distinguish the two mechanisms based on  $K_m$  or  $k_{\text{cat}}/K_m$  (Table 5). For the general base mechanism however, this requires that  $k_2 > k_{-1}$  in order

for  $k_{\text{cat}}/K_m$  to approach  $k_1$  and therefore minimize the hyperbolic increase in this parameter with methanol concentration. However, without knowledge of  $k_1$  and  $k_{-1}$ , the two mechanisms cannot be distinguished. In summary, both models can reasonably describe the partitioning results, and the increased  $k_{\text{cat}}$  with methanol concentration suggests that hydrolysis is rate determining.

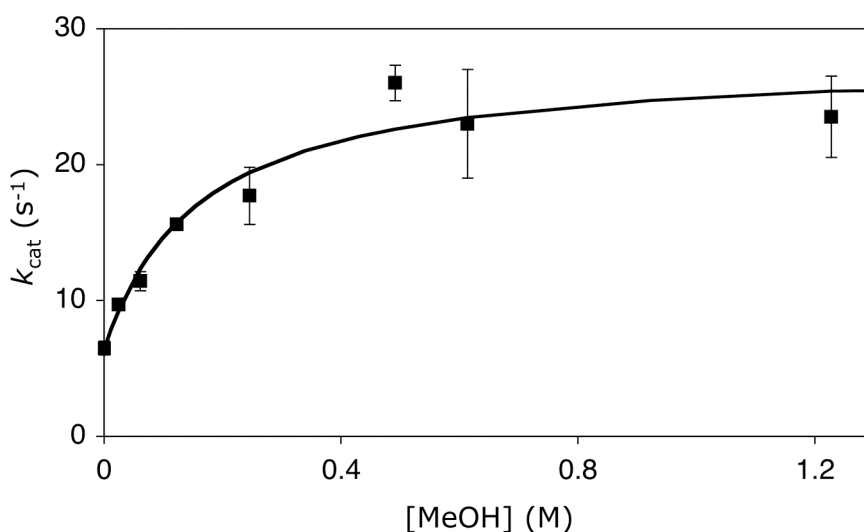


**Figure 25.** The dependence of  $k_{\text{cat}}$  on methanol concentration for the BphD<sub>LB400</sub>-catalyzed degradation of HOPDA. The experimentally-determined  $k_{\text{cat}}$  values (squares) with standard errors are shown with a fitted curve for either the nucleophilic mechanism using  $k_2 = 28 \text{ s}^{-1}$ ,  $k_3 = 8.3 \text{ s}^{-1}$ , and  $k_4 = 230 \text{ M}^{-1} \text{ s}^{-1}$ ; or the general base mechanism using  $k_2 = 28 \text{ s}^{-1}$ ,  $k_{-2} = 11 \text{ s}^{-1}$ ,  $k_3 = 11 \text{ s}^{-1}$ ,  $k_4 = 310 \text{ M}^{-1} \text{ s}^{-1}$ . The parameters were calculated by fitting the  $k_{\text{cat}}$  equations of Figure 24 to the data using the least-squares option of the SCIENTIST software program.

**Table 5.** Experimental steady-state parameters for the BphD<sub>1</sub>LB<sub>400</sub>-catalyzed transformation of HOPDA, compared with values calculated using the equations for either a nucleophilic or general base mechanism, in the presence of varying concentrations of methanol.

| Methanol<br>% (v/v) | Methanol<br>(M) | Experimental <sup>a</sup>           |            |   | Calculated <sup>b</sup>                |            |                      |                      |
|---------------------|-----------------|-------------------------------------|------------|---|--|------------|----------------------|----------------------|
|                     |                 | $k_{\text{cat}}$ (s <sup>-1</sup> ) | $K_m$ (μM) | $k_{\text{cat}}/K_m$<br>(μM <sup>-1</sup> s <sup>-1</sup> ) | $k_{\text{cat}}$<br>(s <sup>-1</sup> ) | $K_m$ (μM) | $k_{\text{cat}}/K_m$ | % methyl<br>benzoate |
| 0                   | 0               | 6.5                                 | 0.20       | 32  | 6.4                                    | 0.23       | 28                   | 0                    |
| 0.1                 | 0.025           | 9.7                                 | 0.35       | 27  | 9.3                                    | 0.33       | 28                   | 40                   |
| 0.25                | 0.061           | 11.4                                | 0.40       | 28  | 12.4                                   | 0.44       | 28                   | 63                   |
| 0.5                 | 0.12            | 15.6                                | 0.83       | 19  | 15.7                                   | 0.56       | 28                   | 77                   |
| 1                   | 0.25            | 17.7                                | 0.57       | 31  | 19.4                                   | 0.69       | 28                   | 87                   |
| 2                   | 0.49            | 26.0                                | 0.85       | 31  | 22.6                                   | 0.81       | 28                   | 93                   |
| 2.5                 | 0.61            | 23.0                                | 0.96       | 24  | 23.5                                   | 0.84       | 28                   | 94                   |
| 5                   | 1.2             | 23.5                                | 1.7        | 14  | 25.4                                   | 0.91       | 28                   | 97                   |

<sup>a</sup>Standard errors are less than 30%.

<sup>b</sup>Values calculated from equations for both nucleophilic and general base mechanisms of Figure 24 using the fitted parameter values described in the text. To prevent a hyperbolic increase in methanol dependence of  $k_{\text{cat}}/K_m$  for the general base mechanism, it was assumed that  $k_1 = 2.8 \times 10^7 \text{ M}^{-1} \text{ s}^{-1}$ , and  $k_{-1} = 0$ .

### 3.4.5 Detection of possible ‘burst’ kinetics for pNPB

The BphD-catalyzed hydrolysis of pNPB provides a convenient probe for burst kinetics, as the release of pNP may be monitored at 400 nm. As depicted in Figure 26, when 1  $\mu\text{M}$  of BphD was mixed with 4  $\mu\text{M}$  of pNPB, multiple phases were observed. A double exponential fit to the data yielded non-random trends in the residuals, suggesting that an alternate model was required to fit the data. Indeed, the first phase could be modeled by a single exponential ( $77\text{ s}^{-1}$ ) corresponding to approximately one turnover of the enzyme ( $\sim 0.7\text{ }\mu\text{M}$ ) followed by a steady-state phase ( $7.3\text{ s}^{-1}$ ) similar to  $k_{\text{cat}}$  which could account for the linearity of the data until  $\sim 0.13\text{ s}$ , when the reaction began to slow down as substrate was depleted. Although the shortness of the steady-state phase warrants cautious interpretation, the present data are consistent with burst kinetics for pNPB.

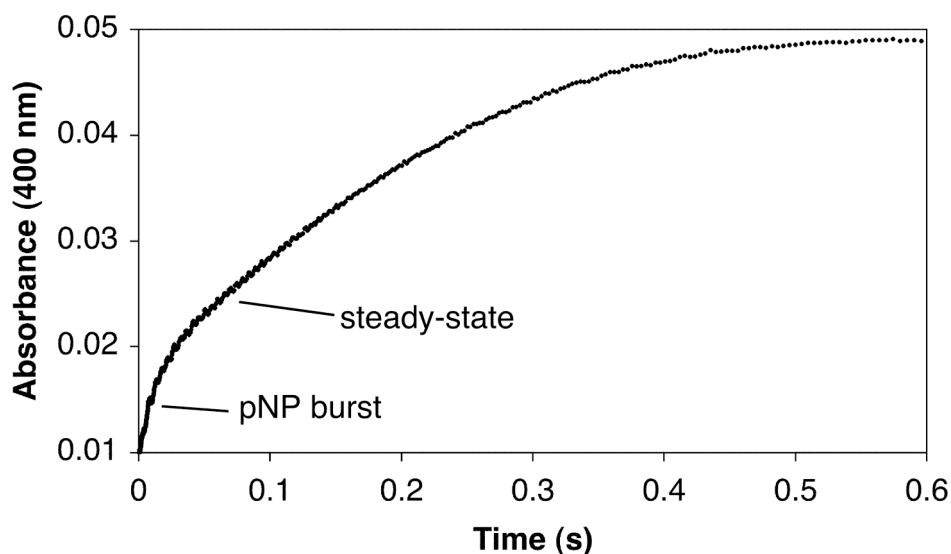


**Figure 26.** A multiple turnover stopped-flow experiment observing a burst of pNP formation upon mixing 1  $\mu\text{M}$  BphD<sub>LB400</sub> with 4  $\mu\text{M}$  pNPB (0.1 M potassium phosphate, pH 7.5, 25 °C).

## Chapter Four: DISCUSSION

### 4.1 Kinetic features of wild type BphD<sub>LB400</sub>

Prior studies have provided evidence for a mechanism involving enzyme-catalyzed tautomerization of MCP to the keto tautomer  $S^k$ , partial  $S^k$  release (99, 101), and hydrolytic C-C cleavage via a *gem*-diol intermediate (108). In the present work, single turnover stopped-flow analysis of BphD<sub>LB400</sub> showed rapid formation of  $E:S^{\text{red}}$  ( $1/\tau_1 \sim 500 \text{ s}^{-1}$ ), an intermediate having an electronic absorption maximum that is strongly red-shifted ( $\lambda_{\text{max}} = 492 \text{ nm}$ ) compared to the HOPDA enolate in aqueous solution ( $\lambda_{\text{max}} = 434 \text{ nm}$ ). This large red-shift suggests that a conformational change and/or enzyme-ligand interactions may perturb the spectrum of the HOPDA enolate. Biphasic decay of  $E:S^{\text{red}}$  ( $1/\tau_2 = 54 \text{ s}^{-1}$ ;  $1/\tau_3 = 6 \text{ s}^{-1}$ ) was coupled to a biphasic increase at 270 nm ( $1/\tau_2 = 48 \text{ s}^{-1}$ ;  $1/\tau_3 = 8 \text{ s}^{-1}$ ), the absorption maximum of the HPD product. The results of product inhibition experiments suggest that HPD may be released prior to benzoate.

#### 4.1.1 Biphasic kinetics cannot be explained by uncoupling

The biphasic decay of  $E:S^{\text{red}}$  (492 nm) and apparent HPD formation (270 nm), respectively, in single turnover stopped-flow experiments could not be satisfactorily explained by either  $S^k$  release or the absorbance of a product complex. Three independent approaches indicated that BphD<sub>LB00</sub> does not detectably release  $S^k$ : (1) HPD formation was apparently coupled to  $E:S^{\text{red}}$  depletion in single turnover stopped-flow experiments (section 3.1.1), suggesting that the first observed enzyme intermediate is quantitatively transformed to product; (2) HPLC analysis revealed no accumulation of  $S^k$  under steady-state conditions (section 3.1.2); and (3) levels of non-specific deuterium incorporation into HPD were low (section 3.1.3). This suggests that  $S^k$  may be released

only from MhpC as suggested by half-site occupation in structural studies (47). Other explanations for the biphasic kinetics must therefore be explored (Section 4.1.2).

#### 4.1.2 Interpretations of the kinetic data

To account for the biphasic decay of  $E:S^{\text{red}}$  in the stopped-flow experiments, two interpretations may be proposed for the wild type enzyme: (A) a mechanism involving reversible ketonization followed by hydrolysis, and (B) a two-conformation model involving ketonization/C-C cleavage followed by benzoate release. As described below, each of these alternatives most logically involves hydrolysis via a *gem*-diol and acyl-enzyme intermediate, respectively.

##### 4.1.2.1 Mechanism A: Discrete keto-intermediate (general base mechanism)

Formation of a discrete keto-intermediate (Figure 27) provides one rationalization for the biphasic decay of  $E:S^{\text{red}}$ . In this mechanism, the three phases observed by stopped-flow may be assigned to (i) rapid formation of  $E:S^{\text{red}}$ , (ii) reversible tautomerization to the keto-intermediate ( $E:S^{\text{k}}$ ), and (iii) hydrolysis of  $S^{\text{k}}$ . The reversibility of ketonization could account for the biphasic decay of  $E:S^{\text{red}}$ . To account for the biphasic increase at 270 nm, the first phase would likely arise from a species other than HPD. Thus, if only HPD absorbs at 270 nm, a lag phase would be observed prior to a monophasic increase as HPD is formed. The biphasic increase in absorbance at 270 nm therefore implies that  $E:S^{\text{k}}$  significantly absorbs at this wavelength. Thus, the first phase at 270 nm would reflect formation of  $E:S^{\text{k}}$ , and the second HPD formation. The rate constants obtained from steady-state analysis of methanol dependence ( $k_2 = 25 \text{ s}^{-1}$ ;  $k_{-2} =$

$11 \text{ s}^{-1}$ ;  $k_3 = 11 \text{ s}^{-1}$ ) predict reciprocal relaxation times ( $1/\tau_2 = 43 \text{ s}^{-1}$  and  $1/\tau_3 = 7 \text{ s}^{-1}$ ) very similar to those observed in the stopped-flow experiments.<sup>2</sup>

This mechanism is most consistent with hydrolysis occurring in one step via a *gem*-diol intermediate (general base mechanism). Although  $\text{E}:\text{S}^{\text{k}}$  breakdown ( $k_3$ ) could in principle occur via enzyme acylation, such  $\text{E}:\text{S}^{\text{k}}$  breakdown is apparently not much faster than  $k_{\text{cat}}$  as indicated by the value of  $1/\tau_3$  associated with HPD formation. Thus, a subsequent deacylation step would have to be much faster than acylation/HPD formation so as not to significantly lower  $k_{\text{cat}}$ . However, if deacylation was much faster than acylation, the observed increase in  $k_{\text{cat}}$  with methanol concentration would not be expected except in the unlikely event that methanol increased the rate of acylation.

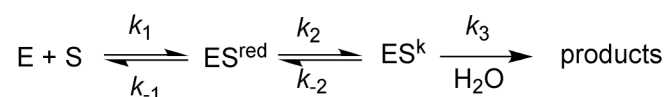


**Figure 27.** Mechanism A: a mechanism involving reversible ketonization and single step hydrolysis via a *gem*-diol intermediate.

#### 4.1.2.2 Mechanism B: Two-conformation model (nucleophilic mechanism)

The biphasic disappearance of  $\text{E}:\text{S}^{\text{red}}$  may also be interpreted as a consequence of two different enzyme forms. This two-conformation model (Figure 28) suggests that the biphasic decay of  $\text{E}:\text{S}^{\text{red}}$  results from two interconverting enzyme conformations: E and E', with only the former capable of catalyzing ketonization/C-C cleavage. C-C cleavage ( $k_2$ ) and benzoate release ( $k_3$ ) must occur in E (half the enzyme sites) before a conformational change converts E' (the other half of the active sites) to E, thereby allowing catalysis to proceed in the remaining 'stalled' active sites. Thus, each subunit cycles between E and E' conformations. The ordered product release in this mechanism

may be thought of in terms of a nucleophilic mechanism, whereby  $k_2$  represents ketonization/acylation, and  $k_3$  represents deacylation. The rate constants shown in Figure 28 would yield the same reciprocal relaxation times ( $1/\tau_2 \sim 50 \text{ s}^{-1}$  and  $1/\tau_3 \sim 8 \text{ s}^{-1}$ ), as expected for consecutive irreversible reactions.<sup>2</sup> Thus, both models A and B can describe the stopped-flow relaxations within the error of the present data.

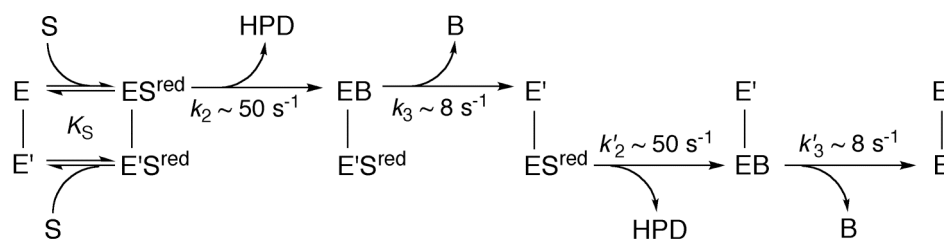


**Figure 28.** Model B: A two-conformation kinetic model accounting for biphasic decay of  $ES^{\text{red}}$ . B represents benzoic acid. The value for  $k_2$  is estimated from the apparent HPD burst observed by stopped-flow, and  $k_3$  is estimated from the final stopped-flow relaxation as well as from steady-state methanol partitioning experiments.

The two-conformation model is intriguing in light of crystal structures of MCP hydrolases. For instance, significant conformational differences are observed between the active sites of monomers A and B in several BphD<sub>LB400</sub> crystal structures (116). Moreover, in the S112C+HOPDA structure (116) obtained from soaking the crystal in substrate, the density for the substrate is less clear in monomer B than in monomer A. Although this low occupancy may reflect restricted access to the former, the crystal packing indicates that monomer B is open to a large solvent channel, while A subunits pack against one another and are further surrounded by B subunits (116). However, it is not obvious how these differences relate to the apparent communication between active sites. A potential means of communication was proposed for MhpC, in which binding of

a substrate analog to only one monomer in the dimer was proposed to reflect the release of keto-intermediate from half of the active sites (47). The authors noted that the catalytic histidine is only two residues away from the beginning of the  $\beta$ 8 strand of the dimer interface – a relationship also observed in BphD<sub>LB400</sub>. It is therefore possible that the movement of His265 accompanying benzoate release in one subunit of BphD<sub>LB400</sub> can translate to a conformational change in the other subunit to enable C-C cleavage. Thus, the different kinetic behaviour of each enzyme may be a consequence of different affinities for the ‘stalled’ E:S<sup>red</sup> intermediate: BphD<sub>LB400</sub> may retain E:S<sup>red</sup> until benzoate is released from the other subunit, while partial release may occur from a more loosely bound MhpC complex.

Structural data also suggest that a conformational change in BphD<sub>LB400</sub> may involve movement of the lid domain. Thus, some conformational differences in the lid domains observed among BphD<sub>LB400</sub> structures suggest that lid movement may occur as in other  $\alpha/\beta$ -hydrolases such as lipases (48, 51). More specifically, the side chains of Arg190 and Phe175 interact with the substrate and thereby apparently motivate two helices of the lid domain to close on the active site – although only small movements of backbone atoms ( $\leq 0.8$  Å) are revealed by a comparison of S112A:HOPDA and S112A:malonate structures (121). In BphD<sub>LB400</sub>, the lid domains make contacts dependent on the tetramer (i.e., the AB' dimer in Figure 29), suggesting that simultaneous product release from both subunits may be impaired. Consistent with a single step assigned to product release in MhpC (104), the MhpC dimer corresponds to the AB dimer of BphD<sub>LB400</sub>, in which the lid domains do not interact directly with each other (47). Alternatively, the conformational change could involve movement of Arg190 within the lid domain to facilitate HPD release. This residue is directed toward the solvent in some MCP hydrolase crystal structures, greatly increasing the solvent

accessibility of the P sub-site (103, 114). As Arg190 is part of the lid domain, it is possible that conformational changes in the lid domain movement and Arg190 occur together to facilitate HPD release.

The model also rationalizes the results of steady-state kinetic experiments in the presence of methanol. Specifically, a discrepancy exists between  $k_2$  (the apparent rate of acylation) obtained via single turnover experiments ( $\sim 50 \text{ s}^{-1}$ ) and that observed via steady-state measurements at high methanol concentrations ( $28 \text{ s}^{-1}$ ). While the former technique provides a direct measurement of  $k_2$ , it is inferred from the latter technique by a methanol-induced change in rate-determining step. At low methanol concentrations,  $k_{\text{cat}}$  primarily reflects rate-determining deacylation ( $\sim 8 \text{ s}^{-1}$ ), which becomes faster with increasing methanol concentration until acylation is rate-determining. In the simplified kinetic model of Figure 24A,  $k_{\text{cat}}$  should be similar to the acylation rate ( $\sim 50 \text{ s}^{-1}$ ) at high methanol concentrations ( $k_{\text{deacylation}} > k_{\text{acylation}}$ ). However, in the two-conformation model, each substrate molecule (after the first turnover) will remain enzyme-bound through two cycles. Thus, assuming  $k_{\text{deacylation}} > k_{\text{acylation}}$  at high methanol concentration, the sum of the transit times (reciprocal rates) for two acylation steps yields  $k_{\text{cat}} \sim 25 \text{ s}^{-1}$  ( $1/k_{\text{cat}} \sim 1/50 \text{ s}^{-1} + 1/50 \text{ s}^{-1}$ ), in reasonable agreement with the observed value of  $28 \text{ s}^{-1}$ .

In summary, evidence for a two-conformation model arises from the biphasic decay of  $\text{E:S}^{\text{red}}$ . Structural data suggests that cycling between E and E' enzyme states may reflect a His265 conformational change and/or movement of the lid domains.

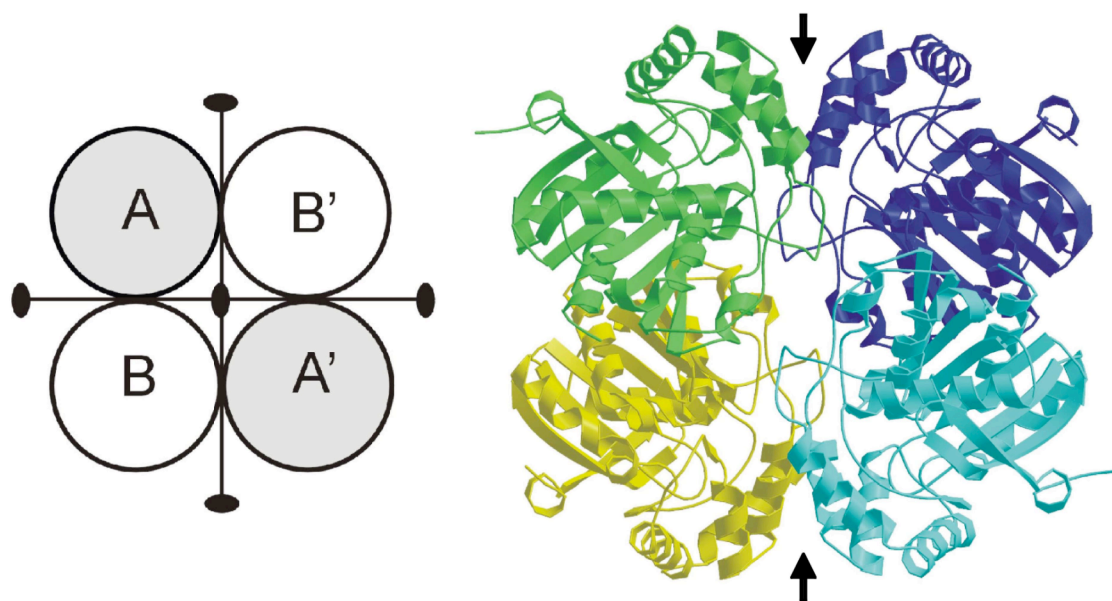


**Figure 29.** The BphD<sub>LB400</sub> tetramer. Left: Schematic diagram of the tetramer. The strong “back-to-back” dimer pairing proposed to represent the basic structural unit in the MCP hydrolase family (section 1.6) occurs at the AB and A'B' interfaces. Right: Ribbon diagram of the tetramer in which the four subunits are coloured green, yellow, cyan, and blue. The arrows highlight the close contacts between lid domains of A and B' (and A' and B) that result from the tetrameric structure of BphD<sub>LB400</sub>. Taken from reference (116).

#### 4.2 Behaviour of variant enzymes

To probe the catalytic roles of active site residues and to trap catalytically relevant intermediates, site-directed mutagenesis was employed. Characterization of alanine variants of active site residues Ser112 and His265 showed that the latter catalyzed E:S<sup>red</sup> formation, and the former catalyzed its decay. Furthermore, the E:S<sup>red</sup> intermediate was trapped in the S112A variant, while the HOPDA enolate (E:S<sup>c</sup>) was apparently trapped in the S112A/H265A double mutant, enabling crystallographic characterization of these species.

#### 4.2.1 An E:S<sup>red</sup> intermediate was trapped in the S112A variant

As in WT enzyme, stopped-flow analysis of the S112A variant revealed the accumulation of an E:S<sup>red</sup> intermediate with an absorption spectrum that was dramatically (>58 nm) red-shifted from that of the free HOPDA enolate band at 434 nm (Figure 18). However, the S112A-bound E:S<sup>red</sup> intermediate ( $\lambda_{\text{max}} = 506$  nm) possessed an absorbance maximum that was red-shifted by 14 nm from that of E:S<sup>red</sup> in WT ( $\lambda_{\text{max}} = 492$  nm).

Despite a 14 nm difference in  $\lambda_{\text{max}}$ , similar spectroscopic and kinetic features imply that a very similar E:S<sup>red</sup> intermediate occurs in both WT and S112A enzymes. Spectroscopically, the overall shapes of the two spectra are remarkably similar: both possess a strong shoulder ~20 nm lower than  $\lambda_{\text{max}}$ . The 14 nm difference may reflect changes in polarity and/or shape of the active site resulting from the substitution of Ser112 with Ala. Mutations are known to significantly change the absorption maxima of chromophores: for example, a Ser94Ala substitution produced a 14 nm blue shift in a visual pigment from newt retina (136). The E:S<sup>red</sup> intermediates in S112A and WT may also be linked kinetically, as similar apparent rates of formation ( $1/\tau \sim 500$  s<sup>-1</sup>) suggest that both enzymes generate a similar intermediate via a similar process.

In summary, the E:S<sup>red</sup> intermediate trapped in the S112A variant is probably very similar to the same intermediate transiently observed in WT. Thus, crystallographic characterization of the S112A:HOPDA complex may provide the structure of a catalytically relevant intermediate.

#### 4.2.1.1 The crystal structure of E:S<sup>red</sup> in the S112A:HOPDA complex

The crystal structure of the E:S<sup>red</sup> intermediate trapped in the S112A:HOPDA complex at 1.8 Å resolution revealed the first image of an entire substrate molecule bound to an MCP hydrolase (Figure 44 and Table 6, Appendix I) (121). Interestingly, the F<sub>o</sub>-F<sub>c</sub> electron density maps revealed non-planar electron density that was compatible with both (1) the keto tautomer of HOPDA, (*E*)-2,6-dioxo-6-phenylhex-3-enoate, and (2) the *cis*-enol(ate) tautomer, (2*Z*,4*Z*)-2-hydroxy-6-oxo-6-phenylhexa-2,4-dienoate (Figure 30). The results of refinements (Appendix I, Table 7) suggest that the keto tautomer **1** is most compatible with the data because it refined without deviation from planarity of the C3-C4 double bond, whereas the *cis*-enolate **2** refined with moderate deviations from planarity at both C2-C3 (5°) and C4-C5 (12°) double bonds (121). Finally, the resonance structure **3** of the HOPDA enolate, (3*E*,5*Z*)-2-oxo-6-oxido-6-phenylhexa-3,5-dienoate (Figure 30) was refined to indicate that the C5-C6 double bond was distorted 30° from planarity. Although the keto tautomer **1** is most compatible with the crystallographic data with respect to minimizing double bond strain, the red-shifted absorption spectrum favours the assignment of E:S<sup>red</sup> to a strained enolate, E:S<sup>se</sup> (Section 4.2.1.2).

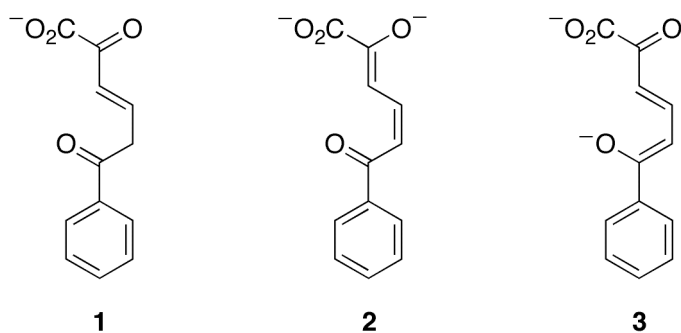


**Figure 30.** Different forms of HOPDA that were examined as possible interpretations of the S112A:HOPDA crystallographic data.

The crystal structure of the S112A:HOPDA complex refined with an  $R$ -value of 17% and root mean square deviations (r.m.s.d.) from ideal bond lengths and angles of 0.013 Å and 1.3°, respectively (Table 6, Appendix I) (121). Figure 31 illustrates the structure of the bound enol(ate) **2** together with key active site residues.

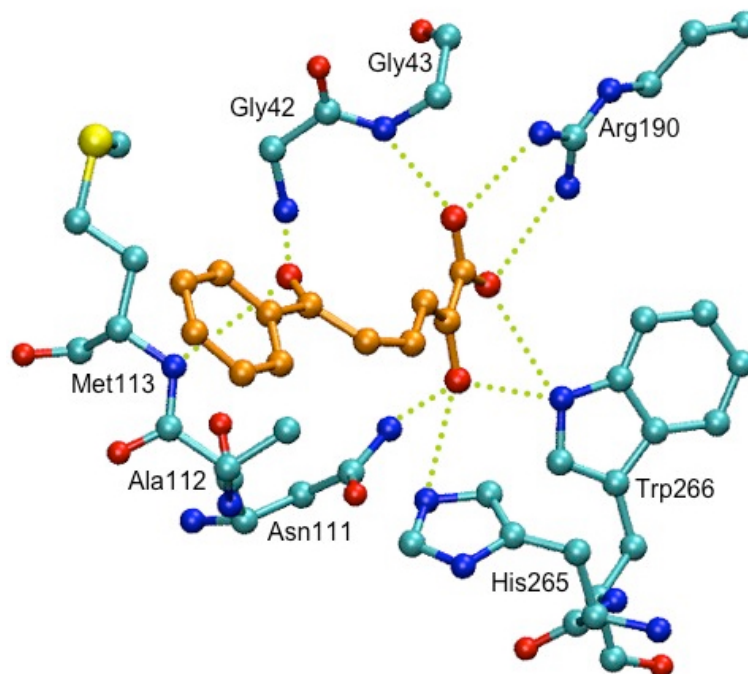


**Figure 31.** Crystal structure of the S112A:HOPDA complex illustrating the  $E:S^{\text{red}}$  intermediate as a strained enolate. Nitrogen, oxygen, and sulfur atoms are coloured blue, red, and yellow, respectively. Protein carbon atoms are coloured cyan, and substrate carbons are orange. Green dotted lines represent potential hydrogen bonds.

#### 4.2.1.2 Assignment of $E:S^{\text{red}}$ to a strained enolate, $E:S^{\text{se}}$

The non-planar conformation of  $E:S^{\text{red}}$  observed crystallographically in Section 4.2.1.1 identifies this intermediate as either the keto or enol(ate) tautomer of HOPDA. However, its red-shifted absorption spectrum disfavours the former assignment because ketonization disrupts HOPDA's double bond conjugation, yielding acetophenone and 2-

keto-3-enoate moieties. The  $\lambda_{\max}$  of both of these species, and therefore the keto-intermediate, should be  $<250$  nm (135), compared to  $\lambda_{\max} = 506$  nm for  $E:S^{\text{red}}$ . Similarly, the spectrum of this intermediate is more consistent with the enolate ( $\lambda_{\max} = 434$  nm) than enol ( $\lambda_{\max} = 341$  nm) form of HOPDA. Nevertheless, the 72 nm red shift in the spectrum of  $E:S^{\text{red}}$  indicates that the enzyme-bound form of the HOPDA enolate significantly differs from solution.

The distortion from planarity in the S112A:HOPDA crystal structure suggests that double bond strain in the HOPDA enolate may account for the red-shifted spectrum of  $E:S^{\text{red}}$ . Indeed, steric hindrance to coplanarity about a double bond raises the ground state energy level but not the excited state, resulting in a red shift (135). For example, twist about double bonds in the retinal chromophore of bacteriorhodopsin has been proposed to explain the red-shifted spectrum of the L photointermediate to  $\lambda_{\max} = 550$  nm from the expected value of  $\lambda_{\max} \sim 491$  nm (137), and this distortion has recently been observed crystallographically (138). Thus,  $E:S^{\text{red}}$  may reasonably be assigned to a non-planar, strained enolate ( $E:S^{\text{sc}}$ ).

#### 4.2.2 H265A variants generate a planar enolate, $E:S^{\text{e}}$

In contrast to S112A, the His265 variants (H265A and S112A/H265A) were unable to accumulate  $E:S^{\text{sc}}$ . Instead, the HOPDA enolate spectrum ( $\lambda_{\max} = 434$  nm) increased in intensity and shifted to  $\lambda_{\max} = 432$  nm, consistent with the formation of an enzyme-bound planar enolate ( $E:S^{\text{e}}$ ).  $E:S^{\text{e}}$  slowly decayed in the H265A variant ( $t_{1/2} \sim 2$  min) prior to a steady-state phase, but was effectively trapped in the S112A/H265A variant ( $t_{1/2} \sim 220$  h), enabling its crystallographic characterization.

#### 4.2.2.1 Crystal structure of E:S<sup>c</sup> trapped in the S112A/H265A:HOPDA complex

The S112A/H265A:HOPDA X-ray crystal structure was solved to 1.6 Å resolution, providing an image of the proposed planar enolate form of HOPDA, E:S<sup>c</sup> (Figure 32). The structure was modeled as the (2*E*,4*E*) isomer of HOPDA and refined to yield an *R*-factor of 18% with r.m.s.d.'s from ideal bond lengths and angles of 0.010 Å and 1.2°, respectively (Table 6, Appendix I). The refined structure possessed C2-C3 and C4-C5 double bond angles deviating from ideal (0/180°) by less than 5°, and with a 13° dihedral angle about the C3-C4 single bond. Thus, the (2*E*,4*E*) isomer of HOPDA is bound in the S112A/H265A complex, compared to the (2*Z*,4*Z*) isomer observed in S112A.

Further differences are observed between the S112A/H265A and S112A complexes with HOPDA. Overall, HOPDA takes on a more planar conformation in the S112A/H265A complex, in contrast to the non-planar orientation observed in S112A. Moreover, the plane of the dienolate moiety of HOPDA is oriented orthogonally to that of the S112A:HOPDA complex (Figure 32) (121). Consequently, the C2 oxygen substituent is moved by 4.1 Å, and the binding interactions of the carboxylate are altered. Whereas the substrate's two carboxylate oxygens hydrogen bond with N $\eta$ 1 and N $\eta$ 2 of Arg190 in the S112A complex, the S112A/H265A complex shows one carboxylate oxygen and the 2-hydroxy group hydrogen bonded to Arg190, and the second carboxylate oxygen interacts with the backbone NH of Gly43. In summary, the absence of His265 apparently leads to formation of the planar HOPDA enolate, which is unable to access the catalytically productive strained conformation of E:S<sup>sc</sup>.

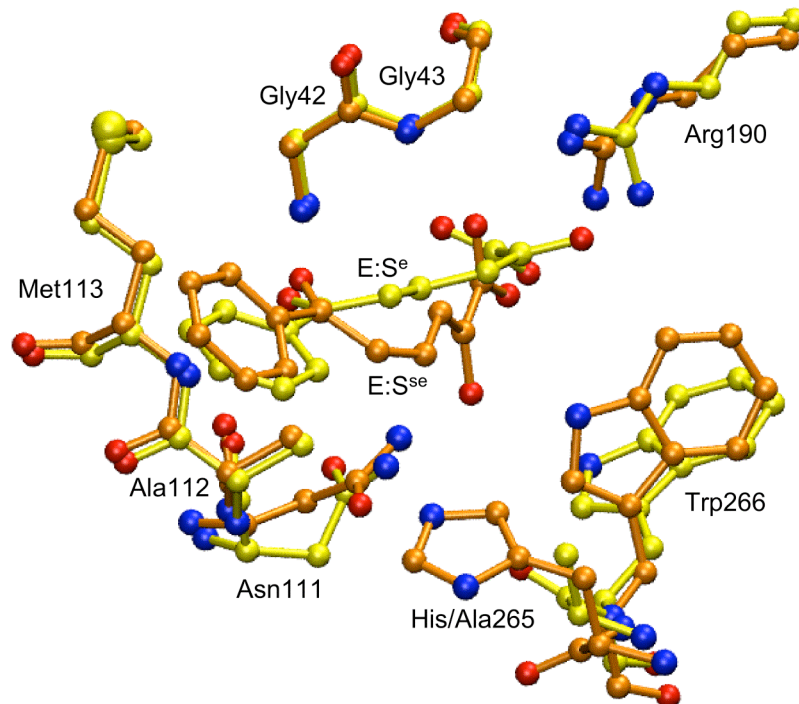


**Figure 32.** Crystal structures of the S112A:HOPDA complex (E:S<sup>sc</sup>, orange carbon atoms) overlaid with the S112A/H265A:HOPDA complex (E:S<sup>c</sup>, yellow carbon atoms, PDB code 2PUJ). Nitrogens and oxygens are coloured blue and red, respectively. Asn51 was removed for clarity. Figure prepared using VMD (117).

## 4.2.3 Mechanistic insights from enzyme:substrate complexes

### 4.2.3.1 His265-dependent formation of E:S<sup>sc</sup>

Because H265A variants do not accumulate E:S<sup>sc</sup>, His265 apparently plays an important role in generating this intermediate. The crystallographically observed orientation of His265 relative to HOPDA suggests that this residue may deprotonate the 2-hydroxyl of the substrate. This is consistent with the requirement for His265 in the ketonization of HPD (Section 3.2.3), which is expected to have a higher  $pK_a$  than

HOPDA. Moreover, abstraction of the 2-hydroxyl proton would yield a protonated His265 as an important proton donor in subsequent steps.

Although His265 may reasonably accomplish deprotonation of HOPDA, the possibility that the enzyme binds the dienolate substrate cannot be excluded. Indeed, both enol and enolate forms of HOPDA are readily available due to its low  $pK_a$  of 7.3 (41). Moreover, deprotonation apparently occurs in the absence of His265, because the absorption spectrum of HOPDA upon binding to H265A variants is consistent with formation of the dienolate ( $E:S^e$ ), albeit at a somewhat reduced rate ( $\sim 220\text{ s}^{-1}$ ) relative to  $E:S^{se}$  formation in WT and S112A ( $\sim 500\text{ s}^{-1}$ ). The formation of  $E:S^e$  in the absence of His265 may reflect the ability of the enzyme to stabilize negative charge on the substrate. If HOPDA binds to the enzyme as the enolate, it seems likely that His265 would be protonated in the resting enzyme in order to protonate C5 and/or the C2-oxygen of the leaving HPD moiety. However, the results of two experiments examining the pH-dependence of MhpC suggest that His265 is not protonated in the resting enzyme: a pH/rate profile revealed an inflexion at pH 6.5 (99), and a stopped-flow relaxation assigned to tautomerization was slower at acidic pH (104).

Finally, His265 may play a steric role in maintaining the twisted conformation of  $E:S^{se}$ . This is a particularly pertinent hypothesis should the enzyme bind the enolate substrate from solution. That is, if not catalyzing deprotonation, it is unclear why His265 would be required to generate  $E:S^{se}$ . The possibility that His265 helps shape the active site to stabilize the strained conformation of bound  $S^{se}$  would explain why this intermediate does not accumulate when the bulk of the sidechain is removed in the H265A variants. Future studies with the H265Q variant may help address the steric role of His265 in  $E:S^{se}$  formation.

Interestingly, the substrate may undergo a significant conformational change upon binding to the enzyme: the  $2Z,4Z$  conformation of  $E:S^{se}$  differs from the  $2Z,4E$  conformation of HOPDA that presumably predominates in solution (41).<sup>5</sup> Thus, if deprotonation is accompanied by rotation about the incipient C4-C5 single bond to afford the non-planar enolate (Figure 33), this conformational change may be allowed by the flexibility of the active site. Indeed, the enzyme's lid domain covers the active site (Figure 12), and its movement during binding could facilitate a conformational change in the substrate.

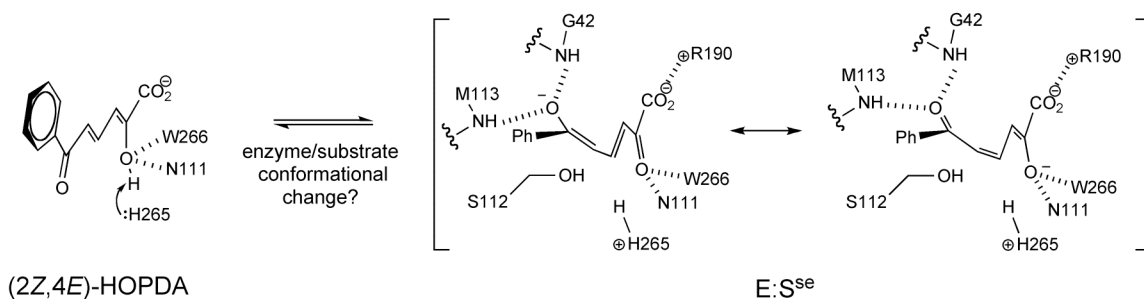


**Figure 33.** Proposed substrate conformational change upon formation of the  $E:S^{se}$  intermediate.

#### 4.2.3.2 Significance of the non-planar conformation of $E:S^{se}$

The non-planar conformation of the  $E:S^{se}$  intermediate may arise in part from the relative orientation of the oxyanion hole and the carboxylate binding site. The distance between these sites is appropriate for the non-planar  $2Z,4Z$  dienolate conformation seen in the  $E:S^{se}$  intermediate but not the fully extended, coplanar  $2Z,4E$  conformation of

<sup>5</sup> NMR studies indicate a *trans*, *transoid* conformation of HOPDA in solution ( $4E$  conformation), but the geometry about the C2-C3 double bond is unknown.

HOPDA that may predominate in solution. Notably, model building experiments suggest that the fully extended *2Z,4E* dienol configuration could associate with the active site, but it cannot do so and simultaneously occupy the carboxylate and oxyanion binding sites (121). Moreover, the enolate tautomer in the S112A/H265A:HOPDA crystal structure is not fully extended, but rather adopts the shortened *2E* conformation (Figure 32). Thus, the relative orientation of the oxyanion hole and the carboxylate binding site apparently contributes to the strained *2Z,4Z* conformation of HOPDA.

The non-planar conformation of  $E:S^{se}$  may be important for modulating the reactivity of this intermediate. Indeed, MhpC had been proposed to bind its substrate in a twisted conformation in order to promote ketonization (101). Double bond strain in the dienolate would decrease overlap among p orbitals in the conjugated  $\pi$  system and therefore increase its reactivity. Hence, the strained enolate intermediate may be required to promote protonation at C5, and such substrate destabilization may represent a general catalytic strategy in the MCP hydrolases.

The  $E:S^{se}$  conformation has additional significance with respect to the stereochemical course of the reaction. Specifically, deuterium incorporation into the  $H5_E$  position of HPD implies C5 protonation on the *si* face of the *cis* C4-C5 double bond followed by C5-C6 fragmentation onto the *re* face of the C3-C4 double bond of the keto-intermediate,  $E:S^k$  (Figure 34). Thus, the requisite pro-*S* protonation at C5 of  $E:S^{se}$  suggests that the proton must originate from ‘below’ the substrate, in the vicinity of Ser112 and His265 (Figure 31).

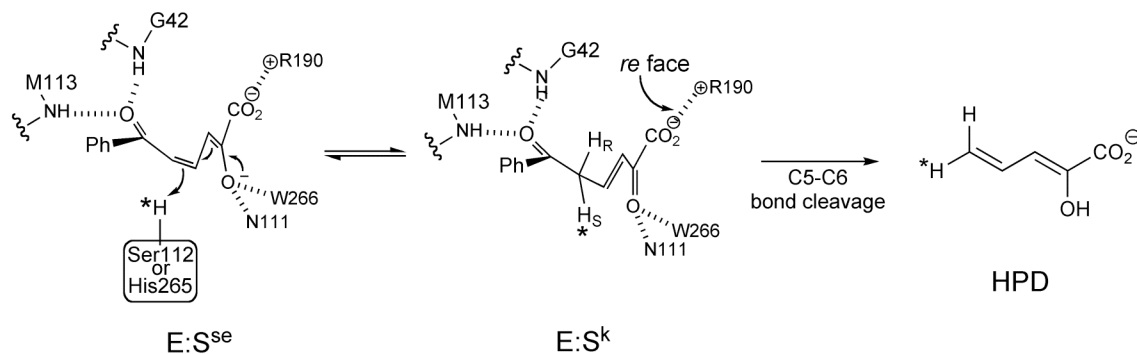


**Figure 34.** Stereochemical course of BphD.

The origin of the proton used to transform  $E:S^{se}$  is linked to the two mechanisms, A and B, which were invoked to rationalize the stopped-flow data at the outset of the Discussion (Section 4.1.2). As discussed below, C5 protonation by His265 is consistent with A: hydrolysis via a general base mechanism. By contrast, protonation by Ser112 is consistent with B: hydrolysis via a nucleophilic mechanism.

#### 4.2.3.3 Mechanism A: His265 protonates C5

The S112A:HOPDA crystal structure reveals that the His265 N $\epsilon$ 2 is 3.1 Å from the HOPDA C2 oxygen and 4.6 Å from C5. Although the latter distance is quite large, the conformational flexibility of His265 observed among different subunits and structures of BphD suggests that distances as low as 2.9 Å may be possible (116). However, the position and orientation of His265 relative to HOPDA suggests that a significant change in the position/conformation of either would be required for C5 protonation. Nevertheless, mechanism A (Figure 35) may be envisioned involving His265-mediated tautomerization followed by hydrolysis, as these two steps would correspond to those used to explain the biphasic increase at 270 nm (Section 4.1.2.1). As the slow step in this model is similar in magnitude to  $k_{cat}$ , it most logically reflects direct hydrolysis of  $E:S^k$

via a *gem*-diol intermediate. By contrast, His265-mediated protonation at C5 is unlikely to lead to hydrolysis via an acyl-enzyme because it generates a discrete keto-intermediate. Thus a two-step hydrolytic mechanism would require deacylation to be much faster than acylation, which is unlikely for the reasons mentioned in Section 4.1.2.1.

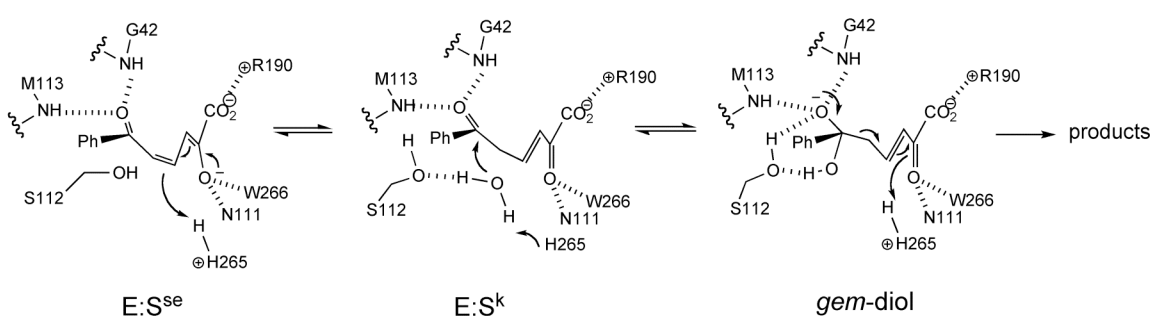


**Figure 35.** Mechanism A: His265-mediated tautomerization and hydrolysis via a *gem*-diolate intermediate.

#### 4.2.3.4 Mechanism B: Ser112 protonates C5

The structural data suggest that Ser112 is better positioned to protonate C5. In the S112A:HOPDA structure, the C $\beta$  atom of Ala112 is in contact with both C5 (3.3 Å) and C6 (3.4 Å) atoms of the enolate substrate. If Ser112 is modeled at this position, its sidechain can be orientated to place O $\gamma$  of Ser112 equidistantly ( $\sim$ 2.3 Å) from C5 and C6, an appropriate distance for protonation at C5 and subsequent nucleophilic attack at C6. With respect to the latter, the O $\gamma$ -C6-O6 would be 100°, which is close to the Bürgi-Dunitz angle of  $\sim$ 107° for nucleophilic attack at a carbonyl carbon. Thus, the substrate C5 may deprotonate Ser112, which would be positioned for nucleophilic attack at C6 (Figure 36). Such a concerted generation of the nucleophile with protonation of C5 would be consistent with the direct transformation of E:S<sup>se</sup> to HPD proposed for

Mechanism B (Section 4.1.2.2), and therefore the absence of a discrete keto-intermediate. Although the higher  $pK_a$  of serine (alcohol  $pK_a \sim 16$  (85)) versus histidine ( $pK_a \sim 6$  (55)) indicates that the latter would be a more suitable proton donor in solution, the  $pK_a$  of Ser112 might be lowered by the nearby protonated His265. Moreover, the  $pK_a$  value is not the sole determinant of the reactivity of Ser112 in this case. For instance, if Ser112 deprotonation is concerted with nucleophilic attack, the reaction would be driven forward even if the former was relatively unfavourable. Indeed, a similar argument can be applied to the catalytic triad, whereby the unfavourable deprotonation of serine is driven forward by subsequent acyl-enzyme formation (56).

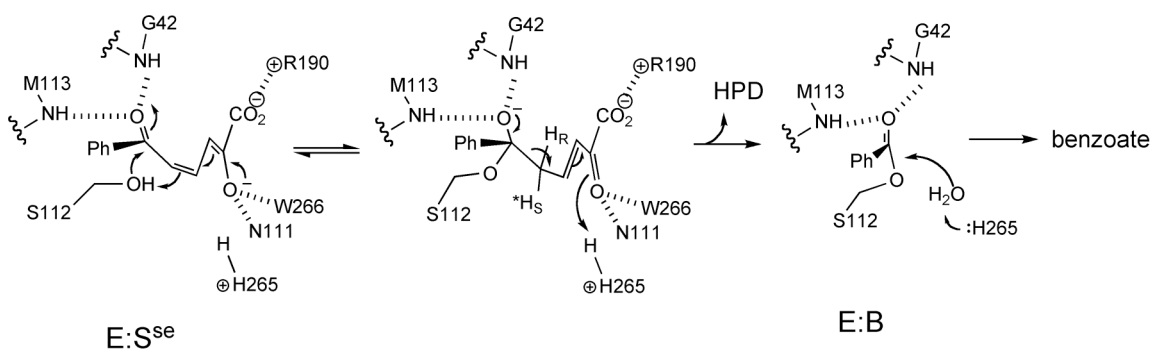


**Figure 36.** Mechanism B: C5 protonation by Ser112 and hydrolysis via nucleophilic catalysis.

Several aspects of the S112A:HOPDA complex are somewhat more consistent with the nucleophilic mechanism. First, the S112A variant traps  $E:S^{se}$  rather than  $E:S^k$ , implying that tautomerization cannot proceed in the absence of Ser112. However, the apparent absence of  $E:S^k$  may result from the preferential stabilization of  $E:S^{se}$  relative to  $E:S^k$  in S112A, and ultimately the presence of some  $E:S^k$  cannot be ruled out. Second, the general base mechanism requires a solvent species to attack  $E:S^k$ . The S112A:HOPDA structure suggests there is inadequate room for a water molecule to approach C6. Moreover, there are no water sized-voids and the nearest ordered water is 7

Å away, beyond a non-polar wall formed by Ile153, Val230, and the HOPDA phenyl moiety. Although it is difficult to imagine that the smaller Ala residue somehow excludes a solvent species in a way that the bulkier Ser would not, it is nevertheless possible that the E:S<sup>sc</sup> structure differs somewhat in conformation from E:S<sup>k</sup>.

#### 4.2.3.5 Significance of the E:S<sup>e</sup> conformation

The planar E:S<sup>e</sup> conformation of HOPDA that was crystallographically characterized in the S112A/H265A variant was spectroscopically observed only in H265A variants, but not in the WT enzyme, indicating that E:S<sup>e</sup> probably does not reflect a catalytically relevant species. However, the poor turnover of this relatively strain-free intermediate indicates the importance of double bond strain in this reaction. Thus, the relatively planar conformation of E:S<sup>e</sup> indicates a stable dienolate substrate that is not readily tautomerized, in contrast to the non-planar E:S<sup>sc</sup> intermediate that is 'primed' for C5 protonation.

The turnover of E:S<sup>e</sup> in H265A suggests that Ser112 is capable of protonation at C5, in accordance with mechanism B (Figure 36). In the H265A variant, the decay of E:S<sup>e</sup> could be described by a single exponential ( $1/\tau \sim 0.0058 \text{ s}^{-1}$ ) prior to a slower steady-state rate of turnover. Significantly, in the absence of His265, E:S<sup>e</sup> must be protonated at C5 by Ser112. In the structures of E:S<sup>e</sup> (the S112A/H265A:HOPDA complex) and E:S<sup>sc</sup> (the S112A:HOPDA complex), the C6 carbonyl occupies the same position in the oxyanion hole. Thus, it seems reasonable that the resulting serinate nucleophile could attack at C6. Accordingly, the slow steady-state phase observed in the H265A variant could represent rate-limiting deacylation in the absence of His265. If Ser112 alone protonates C5 and is involved in acylation, it may seem counterintuitive that this step is so slow in the H265A variant, particularly if the substrate is already

bound as the enolate. The rate of protonation/acylation is probably decreased for two reasons: (i) the E:S<sup>sc</sup> intermediate is not in a twisted conformation to promote C5 protonation, and (ii) His265 is not present to assist in the departure of HPD by protonation of its 2-oxo substituent.

#### 4.2.3.6 Active site conformational changes

Significant conformational changes of active site residues are observed upon formation of E:S<sup>sc</sup>. Most dramatic among them is the movement of the side chain of Trp266 to form a hydrogen bond with the substrate. As observed in Figure 32, the plane of the Trp266 ring in the S112A:HOPDA structure is approximately orthogonal to the plane observed in both the substrate-free and S112A/H265A:HOPDA structures. Moreover, the displacement of Trp266 is coordinated with Phe175 and Phe239 movements to form an extended  $\pi$ -stacking network in the E:S<sup>sc</sup> structure. Interestingly, these conformational changes may provide the necessary stabilization energy to compensate for the double bond strain in the substrate. Thus, the hydrogen bonding with the substrate and new  $\pi$ -stacking interactions may help to drive E:S<sup>sc</sup> formation.

#### 4.2.4 Tautomerization of HPD by variant enzymes

In contrast to WT BphD, the H265A variants did not catalyze tautomerization of HPD, while the S112A substitution resulted in an 80% loss in activity. This result favours the His265-catalyzed proton transfer of Mechanism A but does not rule out the protonation by Ser112 of Mechanism B, as active site residues may interact differently with HOPDA compared to HPD such that different residues protonate C5 for each substrate. For example, a key feature of Mechanism B involves the carbonyl carbon of HOPDA being precisely oriented as an electrophilic sink for the incipient serinate

nucleophile. However, the absence of such a sink in the HPD reaction would yield an unstable serinate upon protonation of C5.

A rationale for the HPD tautomerization activity of variants with respect to Mechanism B is provided in Figure 37. In WT, the serinate would be stabilized by protonated His265. Although S112A substitution would slow the reaction, the protonated His265 could fulfill the role of the absent Ser112. Finally, H265A substitution would drastically reduce activity for two reasons. First, the absence of His265 would slow the deprotonation step, and second, C5 protonation by Ser112 would be thermodynamically unfavourable as it would yield an unstable serinate.

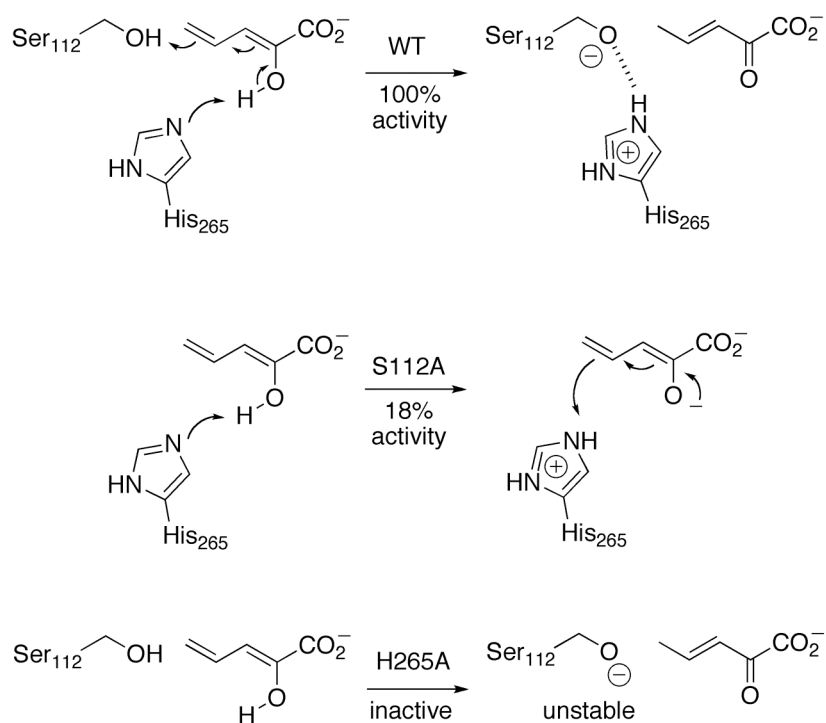


**Figure 37.** Proposed effects of BphD mutations on HPD tautomerization.

### 4.3 Basis for inhibition by 3-Cl HOPDA

The BphD<sub>LB400</sub>-catalyzed reaction represents a bottleneck for PCB degradation by the Bph pathway as some chlorinated HOPDAs are poorly transformed (28, 30, 41). In particular, 3-Cl HOPDAs are particularly potent inhibitors due to their high stability and relatively strong competitive inhibition of the enzyme. Dissection of the structural and functional origins of inhibition in greater detail can inform strategies to improve degradation of 3-Cl HOPDAs.

The steady-state kinetic studies using a series of 3-substituted HOPDAs demonstrate that the steric bulk, not electronegativity, of the 3-substituent obstructs BphD<sub>LB400</sub> catalysis. Incremental increases in the size of the 3-substituent incrementally slowed turnover: the enzyme preferentially hydrolyzed 3-substituted HOPDAs in the order H > F > Cl > Me. By contrast, there is no significant correlation between turnover and electronegativity of the 3-substituent. Stopped-flow spectrophotometry demonstrated that larger 3-substituents impede formation of the E:S<sup>red</sup> intermediate, and therefore presumably prevent the substrate from binding in the non-planar, strained conformation, E:S<sup>se</sup>. For instance, while E:S<sup>se</sup> is apparently completely formed from HOPDA, minor accumulation occurred from 3,10-diF HOPDA, and this intermediate was not detected when 3-Cl HOPDA was used as a substrate. Thus, large 3-substituents apparently inhibit the formation of E:S<sup>se</sup> and ultimately disrupt tautomerization.

The kinetic data predict a non-productive binding mode for 3-substituted HOPDAs. For 3-Cl HOPDA, stopped-flow analysis reveals a two-step transformation: initial formation of an E:S<sup>e</sup> intermediate ( $1/\tau_1 = 15 \text{ s}^{-1}$ ), followed by its decay ( $1/\tau_2 = 0.0077 \text{ s}^{-1}$ ) to products, possibly via rate-determining formation of E:S<sup>se</sup>. The 5 nm spectral blue shift upon formation of E:S<sup>e</sup> from 3-Cl HOPDA is reminiscent of the 2 nm

blue shift observed for HOPDA in the H265A variants. This suggests that 3-Cl HOPDA binds to WT enzyme in the same planar dienolate conformation of E:S<sup>e</sup> in the S112A/H265A variant. For 3,10-diF HOPDA, a similar initial formation of E:S<sup>e</sup> ( $1/\tau_1 = 51 \text{ s}^{-1}$ ) was followed by two slower relaxations ( $1/\tau_2 = 7.6 \text{ s}^{-1}$ ,  $1/\tau_3 = 1.3 \text{ s}^{-1}$ ) during which a small amount of E:S<sup>se</sup> appeared to accumulate. In the S112A variant, the incomplete E:S<sup>se</sup> formation implies reversibility, and suggests that the mechanism may be described by either three-step model in Figure 38.

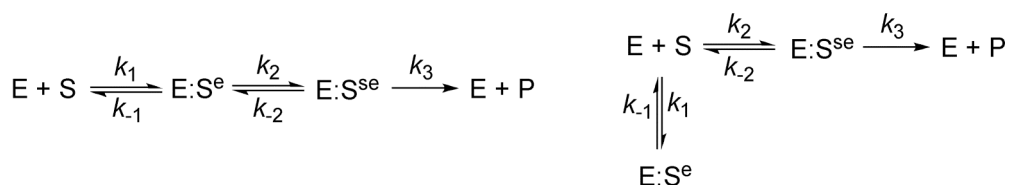


**Figure 38.** Possible kinetic schemes for BphD<sub>LB400</sub>-catalyzed hydrolysis of 3,10-diF HOPDA.

The S112A:3-Cl HOPDA crystal structure is consistent with the kinetic data, indicating that the 3-Cl HOPDA is bound non-productively (Figure 39). This non-productive E:S<sup>e</sup> conformation is very similar to that observed for HOPDA in complex with the S112A/H265A variant (Figure 32), which also does not accumulate E:S<sup>se</sup>. More specifically, the structure reveals a substrate-binding mode wherein 3-Cl HOPDA binds in a C1-C6 coplanar conformation with the plane of the dienolate moiety orthogonal to that of the E:S<sup>se</sup> intermediate of the S112A:HOPDA complex. Thus, the observed binding mode is consistent with the impaired E:S<sup>se</sup> formation of 3-Cl HOPDA observed by stopped-flow. The C1-carboxylate and C2-hydroxyl groups of 3-Cl HOPDA are in remarkably different positions relative to those observed for E:S<sup>se</sup> in the same S112A variant. Whereas both oxygen atoms of the HOPDA C1-carboxylate group hydrogen bond with the guanidinium group of Arg190, this residue instead hydrogen bonds to the 2-oxo/hydroxyl group of 3-Cl HOPDA. As a result, the hydrogen bond between the 2-

oxo/hydroxyl oxygen and the side chain of His265 observed in the S112A complex with HOPDA is not possible for 3-Cl HOPDA. The crystal structure therefore illustrates that the preferred binding mode of 3-Cl HOPDA is incompatible with the proposed His265-mediated deprotonation of the 2-hydroxyl group. Moreover, because the substrate is not bound in the strained conformation of E:S<sup>se</sup>, the stable planar 3-Cl HOPDA dienolate may not be readily protonated at C5.

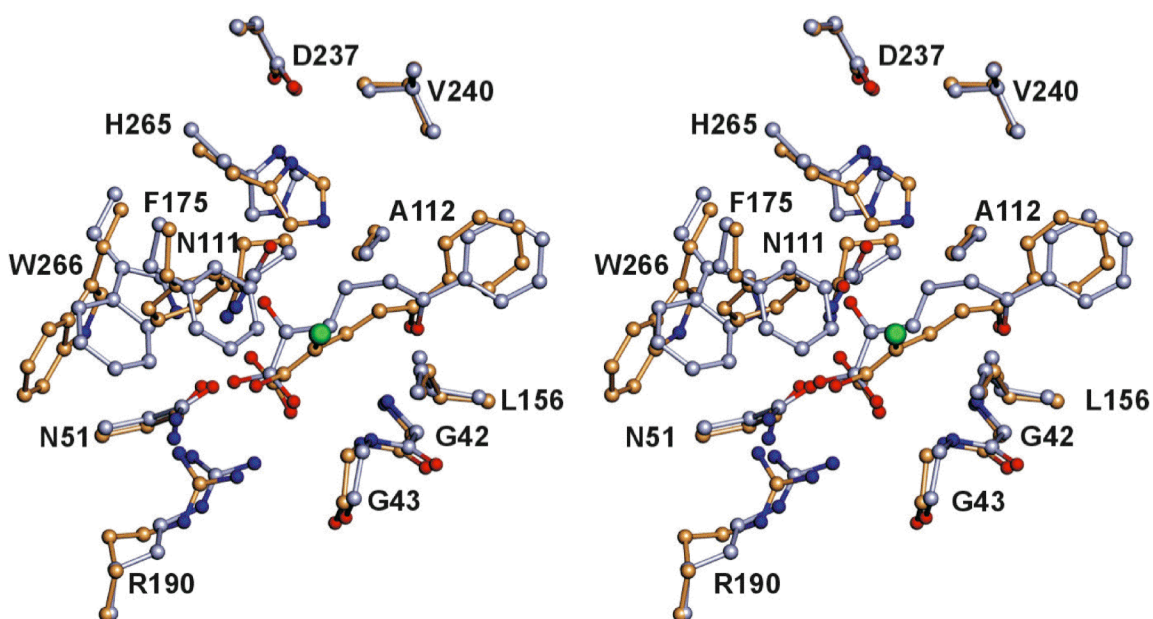


**Figure 39.** Stereo view of superposed active sites of S112A:3-Cl HOPDA and S112A:HOPDA. All C atoms and covalent bonds are coloured in wheat for S112A:3-Cl HOPDA and in gray for S112A:HOPDA. N, O and Cl atoms are colored blue, red and green, respectively. Taken from reference (139).

The crystal structures also provide a possible explanation for the greater accumulation of E:S<sup>e</sup> for 3-Cl HOPDA relative to 3,10-diF HOPDA (Figure 40). The 3-Cl atom occupies a binding pocket formed by the non-polar side chains of Leu156, Phe175, Phe239, and Met171. As these residues do not shift as a result of Ser112 substitution, this binding pocket is probably available and also utilized in the wild type enzyme. It is possible that the compatibility of chlorine vs. fluorine with this

hydrophobic pocket vs. the solution may account for the greater accumulation of 3-Cl HOPDA in the E:S<sup>c</sup> binding mode, although this may also reflect the inability of 3-Cl HOPDA to access the E:S<sup>sc</sup> conformation, as discussed below. Similarly, acetylcholine esterase binds huprine X such that a hydrophobic pocket is fully occupied by the inhibitor's Cl atom, and substitution with fluorine reduces binding affinity (140, 141). In the crystal, the binding of 3-Cl HOPDA is also monomorphic whereas the carboxylate, 2-OH, and 3-F moieties of 3,10-diF HOPDA are not well ordered. This may reflect a difference in binding forces and/or a difference in the interaction between the 2-OH and 3X groups in the 2Z conformation.

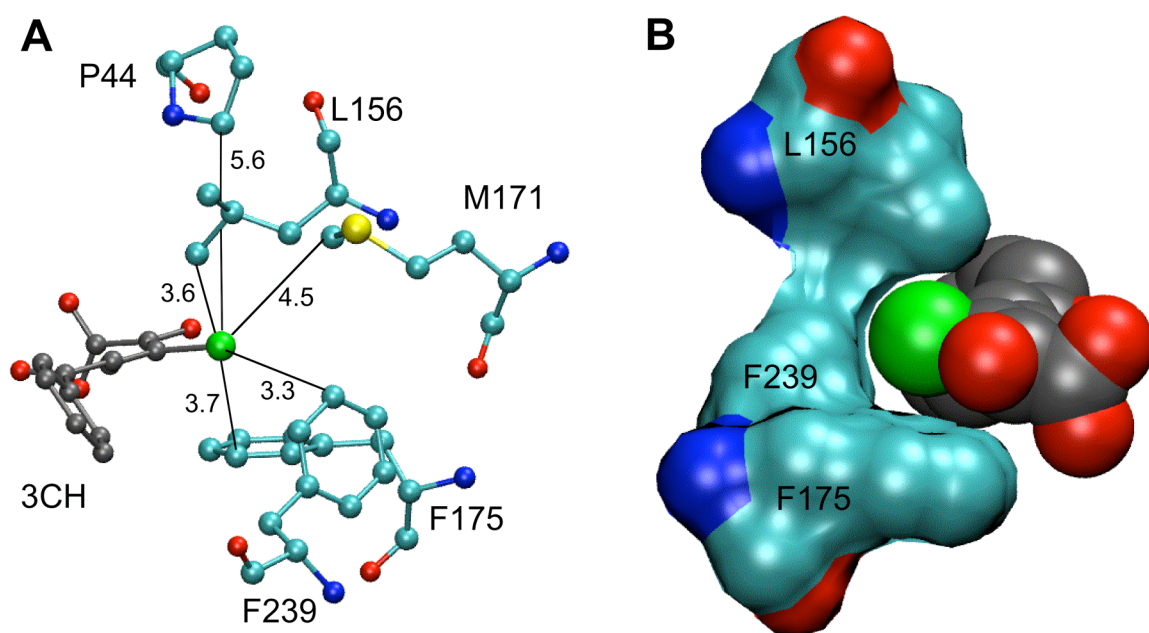


**Figure 40.** The hydrophobic chlorine-binding pocket of the S112A:3-Cl HOPDA complex. A) Ball-and-sticks representations of 3CH and active site residues lining the hydrophobic pocket. Distances between the chlorine atom and nearest atoms of residues are given in Å. B) The closest hydrophobic pocket residues Phe175, Phe239 and Leu156 are shown as a surface calculated using a 1.5 Å probe radius, and 3-Cl HOPDA is shown in space-filling representation. The views in A and B are related by an approximately 180° rotation about the y-axis. Protein and 3-Cl HOPDA carbon atoms are coloured cyan and gray, respectively. Nitrogen, oxygen, and chlorine are blue, red, and green, respectively. Figure made using VMD (117).

The proposed effects of 3-substituted HOPDAs on formation of the catalytically competent E:S<sup>se</sup> are summarized in Figure 41. Unsubstituted HOPDA is rapidly converted to E:S<sup>se</sup> under single turnover conditions ( $1/\tau_1 \sim 500 \text{ s}^{-1}$ ), and the presence of an isosbestic point at  $\sim 461 \text{ nm}$  suggests direct transformation (116, 121). Large 3-substituents may *stabilize* an alternate planar E:S<sup>e</sup> binding mode in which the 3-substituent occupies a hydrophobic pocket. In contrast, large 3-substituents are predicted to *destabilize* the non-planar E:S<sup>se</sup> conformation via a steric clash with the backbone of Gly-43 and/or an intramolecular steric conflict with other HOPDA atoms. Thus, access to E:S<sup>se</sup> is more severely impaired for 3-Cl HOPDA than for 3,10-diF HOPDA. Interestingly, the possibility of moderate destabilization of both E:S<sup>e</sup> and E:S<sup>se</sup> by the 3-F substituent is consistent with the S112A:3,10-diF HOPDA crystal structure indicating multiple binding modes for the carboxylate and 2-OH groups (142). Nevertheless, the association of the 6-oxo group with the oxyanion hole is maintained, which allows the scissile bond to approach the His265 and Ser/Ala112 residues involved in hydrolysis. Although kinetic constants were not determined for 3-Me HOPDA, the volume of the methyl substituent is only  $\sim 25\%$  larger than chlorine, so it may also occupy the hydrophobic pocket.

The preference for 3-Cl HOPDA binding in the alternate planar E:S<sup>e</sup> mode instead of generating the productive, non-planar E:S<sup>se</sup> intermediate has implications for both bioremediation of PCBs and the development of TB therapeutics. With respect to the former, the ability of the BphD homologue DxnB2 to hydrolyze 3-Cl HOPDA with a  $\sim 13$ -fold higher specificity may provide an opportunity to overcome this block in the Bph pathway (42). Nevertheless, the structural basis for the different activities of these enzymes is unclear: Gly-42 and Gly-43, which are proposed to clash with the 3-Cl substituent in the E:S<sup>se</sup> conformation, as well as the flanking residues are conserved

between the two enzymes, as is Phe-74, the residue closest in space to Gly-43. Further studies of DxnB2 should reveal the basis for its improved turnover of 3-Cl HOPDA and may further guide protein engineering efforts.

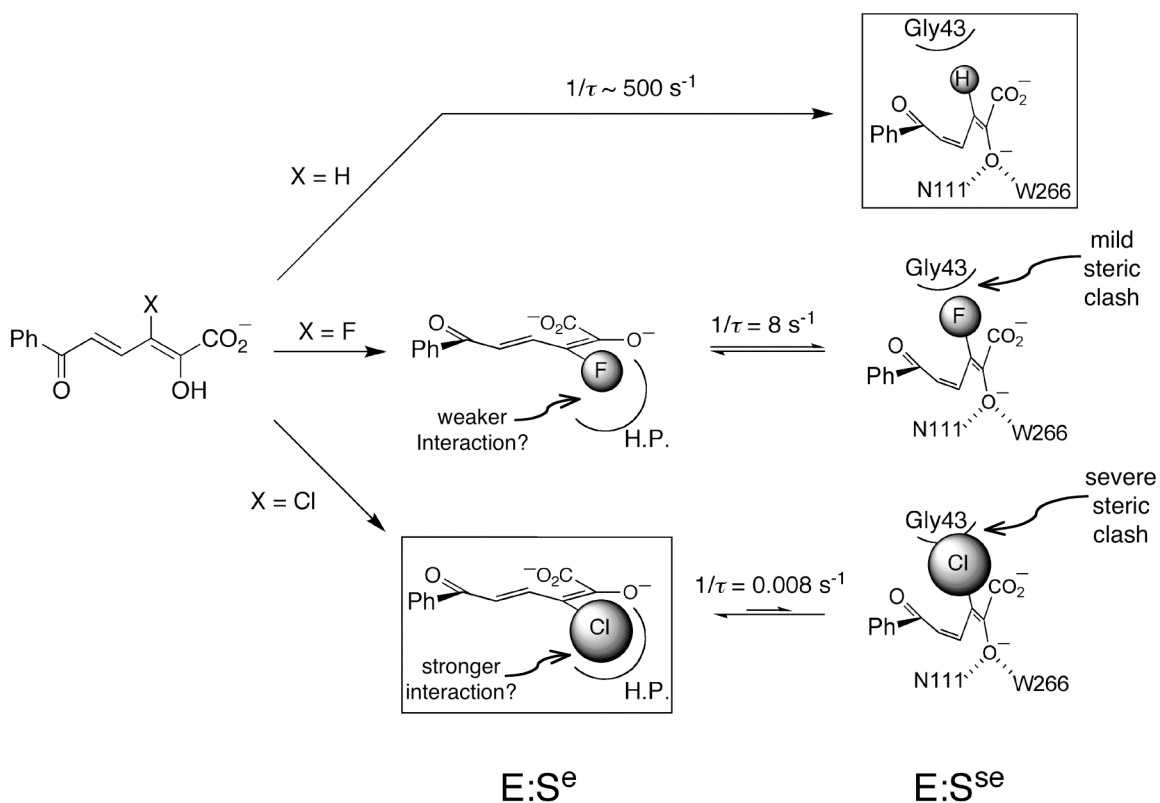


**Figure 41.** The proposed effect of 3-substituent size on  $\text{E:S}^{se}$  formation. H.P. = hydrophobic pocket. Boxes enclose structures that have been crystallographically observed in the hydrolytically-impaired S112A enzyme. Although the protonation state of  $\text{E:S}^e$  is not known, the absorption spectrum is most consistent with an enzyme-bound enolate.

## 4.4 The mechanism of hydrolysis

### 4.4.1 Evidence for a nucleophilic mechanism

As members of the  $\alpha/\beta$ -hydrolase superfamily, the MCP hydrolases are expected to employ the prototypical hydrolytic mechanism in which the catalytic serine acts as a nucleophile to generate a covalent acyl-enzyme intermediate. However, previous work has favoured a general base mechanism involving a non-covalent *gem*-diolate intermediate. Evidence includes the inability to trap a covalent adduct using a  $^{14}\text{C}$ -labelled substrate with MhpC (107, 108), and the observation of a  $^{13}\text{C}$  NMR signal consistent with a *gem*-diol during steady-state turnover of variant MhpC and Ht-BphD<sub>LB400</sub> enzymes (105). Although the results presented in this thesis are not definitive, several lines of evidence favour the existence of an acyl-enzyme intermediate, as outlined below.

First, alanine substitution of the catalytic serine (S112A) reduces turnover by at least  $10^5$ -fold in BphD<sub>LB400</sub>, and activity was not detected in variants of XylF (102) and CumD (103). This suggests that Ser112 contributes  $>29$  kJ/mol to catalysis, consistent with expectations for a nucleophilic role. The general base mechanistic proposal invokes strong hydrogen bonding between Ser112 and the *gem*-diolate (104). Although hydrogen bonds are thought to typically provide 4-12 kJ/mol (56, 143-145), very strong (“low barrier” hydrogen bonds may provide 40-80 kJ/mol (56). For example, strong hydrogen bonds to serine are thought to occur in horse liver alcohol dehydrogenase (146) and UDP-galactose 4-epimerase (147).

Second, the apparent ordered product release can be more satisfactorily rationalized by the nucleophilic mechanism involving a covalent intermediate. Product inhibition experiments imply that HPD is released prior to benzoate, and a burst of HPD

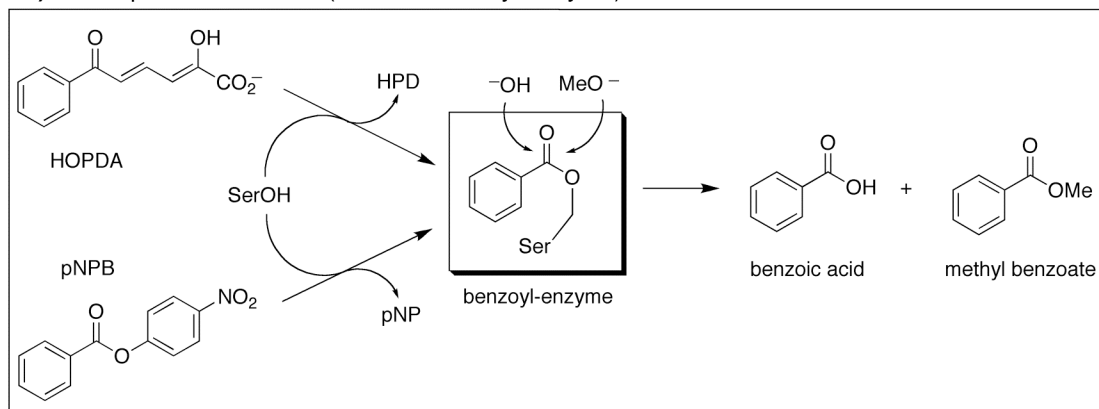
(and *p*-nitrophenol from the pNPB substrate) was observed by stopped-flow spectrophotometry. Both of these results are consistent a nucleophilic mechanism in which rapid acylation of the catalytic serine is followed by rate-limiting deacylation. In contrast, because HPD and benzoate are simultaneously generated from a *gem*-diolate, the general base mechanism must account for impaired benzoate release by its higher affinity and/or hindered release compared to HPD. However, the higher  $K_i$  for benzoate versus HPD suggests that the former should be released more readily than the latter, and therefore apparent binding affinities do not explain the ordered release. Moreover, an active site opening at the NP subsite of the S112A:HOPDA crystal structure also suggests that benzoate should be more readily released than HPD, although movement of the lid domain may enable equally facile release of HPD. Although the instability of HPD warrants cautious interpretation of the product inhibition results, a nucleophilic mechanism provides the simplest explanation for the late release of benzoate.

A third line of evidence supporting a nucleophilic role for Ser112 derives from the structural data. Although the flexibility and dynamics of the active site may enable water to enter during the catalytic cycle, no solvent molecule suitable for attack at the C6 carbonyl was observed in the active site of S112A:HOPDA, despite the extra space made available by removal of the serine hydroxyl: the closest ordered water is 7 Å away. Similarly, the closest ordered waters to the C6 carbonyl are 7.9 and 5.6 Å away in the S112A:3-Cl HOPDA and S112A/H265A:HOPDA structures, respectively. Moreover, the alcohols (methanol, ethanol, n-propanol) that can also attack C6 would be even more difficult to fit into the space between the Ser112 and the bound HOPDA. In contrast, the Ser112 hydroxyl is well positioned for nucleophilic attack at the C6 carbonyl when it is modelled into the S112A:HOPDA structure (121). The structural data also indicates that the main chain amide protons of Met113 and Gly42, which constitute the canonical  $\alpha/\beta$

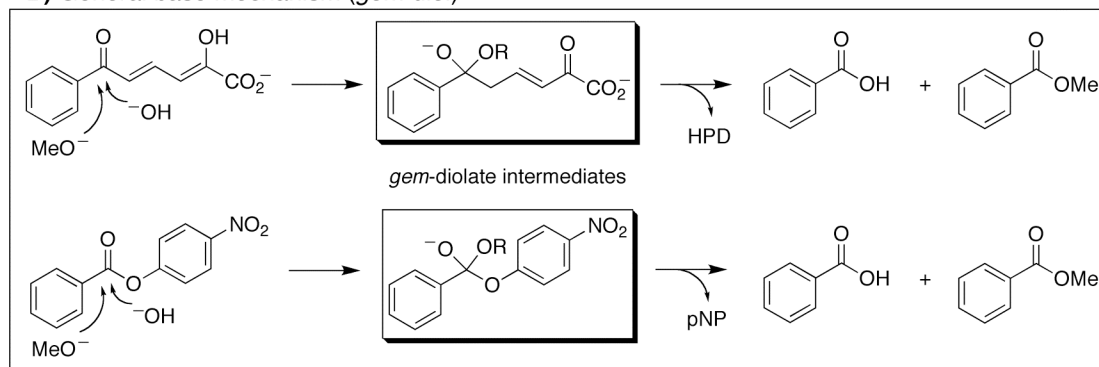
hydrolase oxyanion hole, could readily accommodate any oxyanion intermediates by hydrogen bonding. Hence, the possibility that Ser112 contributes an additional hydrogen bond to the *gem*-diolate oxyanion, as proposed in the general base mechanism (104), seems unnecessary.

Fourth, the similar product ratios afforded by each of HOPDA and pNPB in the presence of methanol implies that these substrates are hydrolyzed via a common intermediate. The nucleophilic mechanism predicts that both substrates should react with Ser112 of BphD<sub>LB400</sub> to generate the same benzoyl-enzyme intermediate, which should be detectable by its subsequent uniform reactivity (Figure 42A). Indeed, the common acid-to-ester product ratio indicates similar partitioning of the benzoyl-enzyme intermediate between water and methanol. In contrast, the absence of a common intermediate in the general base mechanism predicts a unique product ratio for each substrate (Figure 42B). Moreover, a similar  $k_{\text{cat}}$  for both substrates is consistent with rate-determining hydrolysis of a benzoyl-enzyme.

Although similar  $k_{\text{cat}}$  and product ratios for different substrates suggest the presence of a common intermediate whose breakdown is rate-determining, neither result provides definitive evidence for a nucleophilic mechanism. The similar  $k_{\text{cat}}$  may reflect rate-limiting dissociation of a common non-covalent enzyme-benzoate complex. For example, rate-determining dissociation of phosphate from alkaline phosphatase gives rise to similar  $k_{\text{cat}}$  values for the hydrolysis of several phosphate esters (148, 149). The common product ratio also does not completely rule out a general base mechanism, as it is possible that the ratio of hydrolysis to methanolysis is unaffected by the substrate.

**A) Nucleophilic mechanism (covalent benzoyl-enzyme)**

*common intermediate = common product ratio*

**B) General base mechanism (*gem*-diolate)**

*different intermediates = different product ratios*

**Figure 42.** Partitioning between methanol and water may distinguish hydrolytic mechanisms. A) In the nucleophilic mechanism, acylation generates a common covalent intermediate for both substrates. Deacylation by water or methanol produces a common product ratio for both substrates. B) In the general base mechanism, direct attack of the substrate may also yield a common product ratio for each substrate, but not necessarily.

**4.4.2 Evidence for a general base mechanism**

Although this thesis presents evidence consistent with a nucleophilic mechanism for BphD<sub>LB400</sub>, evidence has been obtained for a *gem*-diolate intermediate in MphC (105, 108), BphD<sub>LB400</sub> (109, 110) and Ht-BphD<sub>LB400</sub> (105, 113). This evidence comes from five lines of investigation. First, <1% of the enzyme was covalently modified after quenching MhpC in the presence of a radiolabelled substrate (108). Second, additional

$^{18}\text{O}$  was incorporated into the substrate and a non-hydrolysable analog (108). Third, a reduced analog containing a C6 alcohol underwent enzyme-catalyzed retro-aldol cleavage (109). Fourth, Hammett analysis of BphD<sub>LB400</sub>-catalyzed HOPDA hydrolysis revealed different behaviour than serine proteases (109, 110), and burst kinetics were not observed in the reaction of *p*-nitrophenyl acetate with Ht-BphD<sub>LB400</sub> (113). Finally, a  $^{13}\text{C}$  NMR signal consistent with a *gem*-diol was observed during turnover by Ht-BphD<sub>LB400</sub> and MhpC variants (105).

Initial evidence against an acyl-enzyme intermediate arose from the inability to detect a covalent intermediate by quenching the MhpC reaction in the presence of a radiolabelled substrate (107, 108). Although an acyl-enzyme should be more stable at low pH, the extensive manipulations of the sample (gel filtration, incubation, centrifugation, etc) after quenching may have provided enough time for deacylation to occur. The incorporation of two heavy atoms from  $\text{H}_2^{18}\text{O}$  into ~5% of the acid product was also interpreted as evidence for *gem*-diolate formation (107, 108). A second heavy atom must arise either from: (i) partial (~10%) release of the *gem*-diol into solution and its subsequent decay back to starting material (yielding ~5% heavy atom incorporation) prior to re-entry to the catalytic cycle; or (ii) ~5% of the *gem*-diol decaying back to starting material in the active site by loss of the substrate  $^{16}\text{O}$  atom. As the *gem*-diol should be tightly bound the enzyme, its release in option (i) seems unlikely. Option (ii) effectively represents a side reaction, because decay of the *gem*-diol would release water to the opposite face of the substrate rather than to the face from which it originally attacked (which would constitute the reverse reaction). Thus, it is possible that 5% heavy atom incorporation reflects a side reaction rather than a catalytically-relevant species,. A second exchange experiment demonstrated that MhpC incorporates  $^{18}\text{O}$  into a non-

hydrolyzable inhibitor, but this may not reflect hydrolytic turnover of the natural substrate.

A *gem*-diol mechanism was also favoured because BphD<sub>LB400</sub> catalyzes relatively slow ( $k_{\text{cat}}$  is ~1% of that for HOPDA) retro-aldol cleavage of a reduced substrate containing a C6 alcohol, presumably via general base catalysis (109). However, because this substrate lacks a C6 carbonyl required for nucleophilic catalysis, general base catalysis is expected regardless of the hydrolytic mechanism employed for HOPDA hydrolysis. Thus, the observed retro-aldol cleavage of a reduced substrate does not directly address the question of nucleophilic versus general base-catalyzed hydrolysis of HOPDA.

Hammett analysis of BphD<sub>LB400</sub> with *para*-substituted HOPDAs demonstrated that  $k_{\text{cat}}$  decreases with electron-withdrawing substituents (negative  $\rho$ -value) (109, 110), opposite to the positive  $\rho$ -value obtained with non-natural substrates in chymotrypsin and subtilisin, which employ a nucleophilic mechanism. Although this difference was proposed to reflect a general base mechanism for BphD<sub>LB400</sub>, subsequent Hammett analyses revealed that Ht-BphD<sub>LB400</sub> and several other  $\alpha/\beta$ -hydrolases all hydrolyzed *p*-nitrophenyl benzoyl esters with positive  $\rho$ -values (113). Nevertheless, a general base mechanism was proposed in this study because a *p*-nitrophenol burst was not observed in a multiple turnover stopped-flow experiment with *p*-nitrophenyl acetate. However, the single turnover rate of *p*-nitrophenol formation was ~3-fold larger than  $k_{\text{cat}}$ , suggesting that product release was rate-limiting. This result could be interpreted as evidence for an acyl-enzyme mechanism, in which acylation is only ~3 times faster than deacylation for this substrate. Thus, the burst may not have been observed because of the small difference between these two rates made them difficult to distinguish.

Finally, in the steady-state turnover of HOPDA labelled with  $^{13}\text{C}$  at C6 by each of the S112A and H265A variants of Ht-BphD<sub>LB400</sub> and the H114A variant of MhpC, a  $^{13}\text{C}$  NMR signal (128 ppm) was observed and assigned to the *gem*-diol intermediate (105). Although the signal was also present in the absence of enzyme, line-broadening in the presence of enzyme suggested an enzyme-bound *gem*-diol. Importantly, this signal could not be washed out with unlabelled HOPDA, suggesting that the variant enzymes did not simply bind the *gem*-diol from solution. Nevertheless, as these data were obtained with variant enzymes, it is not clear how relevant they are to the wild type enzyme. Indeed, a *gem*-diol hydrolytic mechanism is the only option in the absence of the Ser112 nucleophile, and may also be favoured without His265. For instance, substitution of the latter with alanine prevented accumulation of E:S<sup>sc</sup>, suggesting that HOPDA accumulates in an E:S<sup>c</sup> conformation that is not relevant to wild type catalysis, as discussed in Section 4.2.3.5.

#### 4.5 Overall Mechanism

Insights from biochemical and structural characterizations can be combined to propose a mechanism for WT BphD<sub>LB400</sub> (Figure 43). The S112A:HOPDA crystal structure suggests that the HOPDA enol is deprotonated by His265 and a conformational change produces a non-planar, strained enolate (E:S<sup>sc</sup>). A conformational change such as lid closure may occur as His265 abstracts the 2-hydroxyl proton, thereby generating E:S<sup>sc</sup>, which can fit in the ‘closed’ active site (*e.g.* simultaneously occupy the oxyanion and carboxylate binding sites). However, it is also possible that the resting enzyme possesses a protonated His265, and binds the enolate from solution.

The strained conformation of E:S<sup>sc</sup> is relevant to its further reactivity. Significant enzyme conformational changes between planar (E:S<sup>c</sup>) and strained (E:S<sup>sc</sup>) enolate

complexes may provide the driving force for inducing double bond strain in the substrate. Most obviously, E:S<sup>se</sup> forms a new interaction resulting from a large movement of Trp266, which also produces a new  $\pi$ -stacking network among Trp266, Phe175 and Phe239. The double bond strain in E:S<sup>se</sup> would activate the substrate towards protonation at C5.

Either His265 (mechanism A) or Ser112 (mechanism B) appear capable of protonating E:S<sup>se</sup> at C5 to generate the ketonized intermediate, E:S<sup>k</sup>. In mechanism A, His265 would then activate water to directly hydrolyze E:S<sup>k</sup> via a *gem*-diol intermediate. This mechanism is consistent with the stopped-flow kinetic data inasmuch as E:S<sup>k</sup> is expected to absorb significantly at 270 nm. However, the transient spectra did not detect an intermediate with a spectrum distinct from HPD. However, the similar  $k_{\text{cat}}$  values and product ratios for HOPDA and pNPB suggest the presence of a common intermediate, which is more consistent with rate-determining hydrolysis of a benzoyl-enzyme expected for the nucleophilic mechanism.

In the nucleophilic mechanism B, Ser112 would protonate C5 and immediately attack C6 to acylate the enzyme and release HPD, followed by rate-limiting His265-catalyzed deacylation. Biphasic E:S<sup>se</sup> decay and HPD formation could be accounted for by two conformational states of the enzyme. This model more satisfactorily explains the apparent ordered product release, the similar  $k_{\text{cat}}$  values and product ratios for HOPDA and pNPB, the apparent burst kinetics for pNPB, and the absence of solvent species in the vicinity of residue 112 in all structurally characterized E:HOPDA complexes.

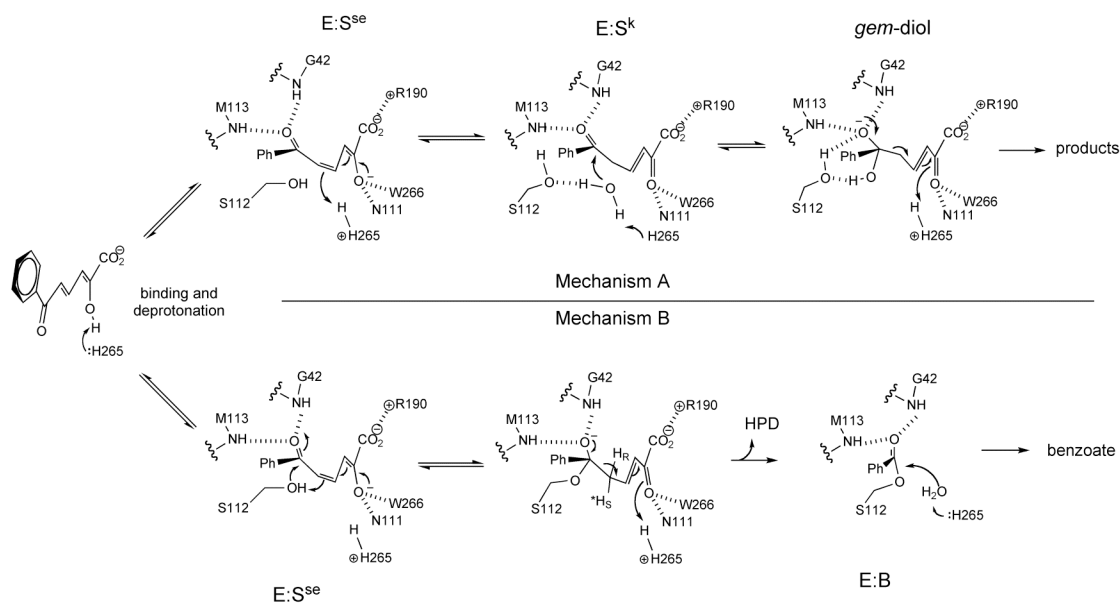


**Figure 43.** Possible mechanisms of BphD<sub>LB400</sub>.

#### 4.6 Concluding Remarks

This thesis describes the characterization of BphD<sub>LB400</sub> leading to several new insights into MCP hydrolases. The new knowledge of catalytic intermediates, mechanism of inhibition, and roles of conserved active site residues benefit future studies of related enzymes. Indeed, similar studies involving HsaD from *M. tuberculosis* have been initiated with a view to developing inhibitors for this enzyme.

Identification of a strained intermediate is particularly interesting, as it identifies double bond strain as a key feature of catalysis. The present evidence for assigning the red-shifted spectrum of E:S<sup>red</sup> to the strained enolate intermediate E:S<sup>se</sup> includes electronic absorption spectroscopy and X-ray crystallography. However, the presence of a mixture of keto (E:S<sup>k</sup>) and E:S<sup>se</sup> could not be ruled out. As the absence of E:S<sup>k</sup> in the S112A:HOPDA structure would favour the role of Ser112 in tautomerization, the identity

of E:S<sup>red</sup> may be further probed by characterizing the hybridization of C5 ( $sp^3$  or  $sp^2$ ) of S112A-bound HOPDA via  $^{19}\text{F}$ -NMR and/or crystallographic analysis of 5-F HOPDA, as well as UV resonance Raman studies.

Inhibition by 3-Cl HOPDAs occurs via binding in an alternate conformation in which the chlorine substituent occupies a hydrophobic pocket. To overcome this inhibition, future work may focus on modifying the active site via protein engineering. Moreover, other MCP hydrolases such as DxnB2 can more efficiently degrade 3-Cl HOPDAs, and may provide a starting point for directed evolution or gene shuffling.

This thesis also presents evidence suggesting the possible existence of an acyl-enzyme rather than a *gem*-diolate intermediate. However, the present evidence is not definitive, as only the direct observation of a covalent intermediate would prove the nucleophilic mechanism. As the acyl-enzyme should accumulate during steady state, its detection may be achieved by quench-flow followed by mass spectrometry if the intermediate is sufficiently stable.

**BIBLIOGRAPHY**

1. Fox, M. A., and Whitesell, J. K. (1994) *Organic Chemistry*, Jones and Bartlett Publishers, Inc., London.
2. Cyranski, M. K. (2005) *Chem. Rev.* *105*, 3773-3811.
3. Dagley, S. (1975) *Essays Biochem.* *11*, 81-138.
4. Boll, M. (2005) *J. Mol. Microbiol. Biotechnol.* *10*, 132-142.
5. Schink, B., Philipp, B., and Muller, J. (2000) *Naturwissenschaften* *87*, 12-23.
6. McLeod, M. P., and Eltis, L. D. (2007) Genomic insights into the aerobic pathways for degradation of organic pollutants., in *Microbial biodegradation: genomics and molecular biology* (Diaz, E., Ed.), Horizon Scientific Press.
7. Deneff, V. J., Klappenbach, J. A., Patrauchan, M. A., Florizone, C., Rodrigues, J. L. M., Tsoi, T. V., Verstraete, W., Eltis, L. D., and Tiedje, J. M. (2006) *Appl. Environ. Microb.* *72*, 585-595.
8. Ferrandez, A., Minambres, B., Garcia, B., Olivera, E. R., Luengo, J. M., Garcia, J. L., and Diaz, E. (1998) *J. Biol. Chem.* *273*, 25974-25986.
9. Ferraro, D. J., Gakhar, L., and Ramaswamy, S. (2005) *Biochem. Biophys. Res. Commun.* *338*, 175-190.
10. Gibson, D. T., and Parales, R. E. (2000) *Curr. Opin. Biotechnol.* *11*, 236-243.
11. Vaillancourt, F. H., Bolin, J. T., and Eltis, L. D. (2006) *Crit. Rev. Biochem. Mol. Biol.* *41*, 241-267.
12. Bugg, T. D. H., and Lin, G. (2001) *Chem. Commun.*, 941-952.
13. U.S. Environmental Protection Agency. Polychlorinated biphenyls (PCBs). <http://www.epa.gov/epaoswer/hazwaste/pcbs/index.htm>. Accessed November 1, 2007.
14. Faroon, O., Keith, L., Smith-Simon, C., and De Rosa, C. (2003) in *Concise international chemical assessment document 55*, World Health Organization, Geneva.
15. National Center for Environmental Assessment, U.S. Environmental Protection Agency. (1996) PCBs: cancer dose-response assessment and application to environmental mixtures. Washington, D.C.
16. Knerr, S., and Schrenk, D. (2006) *Crit. Rev. Toxicol.* *36*, 663-694.
17. Jacobson, J. L., and Jacobson, S. W. (1996) *N. Engl. J. Med.* *335*, 783-789.

18. Mariussen, E., and Fonnum, F. (2006) *Crit. Rev. Toxicol.* 36, 253-289.
19. Nakajima, S., Saijo, Y., Kato, S., Sasaki, S., Uno, K., Kanagami, N., Hirakawa, H., Hori, T., Tobiishi, K., Todaka, T., Nakamura, Y., Yanagiya, S., Sengoku, Y., Iida, T., Sata, F., and Kishi, R. (2006) *Environ. Health Perspect.* 114, 773-778.
20. Sharpe, R. M., and Irvine, D. S. (2004) *Brit. Med. J.* 328, 447-451.
21. Toft, G., Hagmar, L., Giwercman, A., and Bonde, J. P. (2004) *Reprod. Toxicol.* 19, 5-26.
22. Ulbrich, B., and Stahlmann, R. (2004) *Arch. Toxicol.* 78, 252-268.
23. Schwarzenbach, R. P., Escher, B. I., Fenner, K., Hofstetter, T. B., Johnson, C. A., von Gunten, U., and Wehrli, B. (2006) *Science* 313, 1072-1077.
24. Judd, N., Griffith, W. C., and Faustman, E. M. (2004) *Regul. Toxicol. Pharmacol.* 40, 125-135.
25. Mozaffarian, D., and Rimm, E. B. (2006) *JAMA-J. Am. Med. Assoc.* 296, 1885-1899.
26. Indian and Northern Affairs Canada. (2003) Canadian arctic contaminants assessment report II: sources, occurrence, trends and pathways in the physical environment. Ottawa, ON.
27. Pieper, D. H. (2005) *Appl. Microbiol. Biotechnol.* 67, 170-191.
28. Bedard, D. L., and Haberl, M. L. (1990) *Microb. Ecol.* 20, 87-102.
29. Bedard, D. L., Unterman, R., Bopp, L. H., Brennan, M. J., Haberl, M. L., and Johnson, C. (1986) *Appl. Environ. Microbiol.* 51, 761-768.
30. Furukawa, K., Tomizuka, N., and Kamibayashi, A. (1979) *Appl. Environ. Microb.* 38, 301-310.
31. Seeger, M., Timmis, K. N., and Hofer, B. (1995) *Appl. Environ. Microb.* 61, 2654-2658.
32. Billingsley, K. A., Backus, S. M., Juneson, C., and Ward, O. P. (1997) *Can. J. Microbiol.* 43, 1172-1179.
33. Billingsley, K. A., Backus, S. M., Wilson, S., Singh, A., and Ward, O. P. (2002) *Biotechnol. Lett.* 24, 1827-1832.
34. Bopp, L. H. (1986) *J. Indust. Microbiol.* 1, 23-29.
35. Gibson, D. T., Cruden, D. L., Haddock, J. D., Zylstra, G. J., and Brand, J. M. (1993) *J. Bacteriol.* 175, 4561-4564.
36. Barriault, D., and Sylvestre, M. (2004) *J. Biol. Chem.* 279, 47480-47488.

37. Kumamaru, T., Suenaga, H., Mitsuoka, M., Watanabe, T., and Furukawa, K. (1998) *Nat. Biotechnol.* *16*, 663-666.
38. Zielinski, M., Kahl, S., Standfuss-Gabisch, C., Cadmara, B., Seeger, M., and Hofer, B. (2006) *Appl. Environ. Microb.* *72*, 2191-2199.
39. Dai, S. D., Vaillancourt, F. H., Maaroufi, H., Drouin, H. M., Neau, D. B., Snieckus, V., Bolin, J. T., and Eltis, L. D. (2002) *Nat. Struct. Biol.* *9*, 934-939.
40. Fortin, P. D., MacPherson, I., Neau, D. B., Bolin, J. T., and Eltis, L. D. (2005) *J. Biol. Chem.* *280*, 42307-42314.
41. Seah, S. Y. K., Labbé, G., Nerdinger, S., Johnson, M. R., Snieckus, V., and Eltis, L. D. (2000) *J. Biol. Chem.* *275*, 15701-15708.
42. Seah, S. Y. K., Ke, J., Denis, G., Horsman, G. P., Fortin, P. D., Whiting, C. J., and Eltis, L. D. (2007) *J. Bacteriol.* *189*, 4038-4045.
43. Seah, S. Y. K., Labbé, G., Kaschabek, S. R., Reifenrath, F., Reineke, W., and Eltis, L. D. (2001) *J. Bacteriol.* *183*, 1511-1516.
44. Fortin, P. D., Horsman, G. P., Yang, H. M., and Eltis, L. D. (2006) *J. Bacteriol.* *188*, 4424-4430.
45. Rengarajan, J., Bloom, B. R., and Rubin, E. J. (2005) *Proc. Natl. Acad. Sci. U. S. A.* *102*, 8327-8332.
46. Van der Geize, R., Yam, K., Heuser, T., Wilbrink, M. H., Hara, H., Anderton, M. C., Sim, E., Dijkhuizen, L., Davies, J. E., Mohn, W. W., and Eltis, L. D. (2007) *Proc. Natl. Acad. Sci. U. S. A.* *104*, 1947-1952.
47. Dunn, G., Montgomery, M. G., Mohammed, F., Coker, A., Cooper, J. B., Robertson, T., Garcia, J. L., Bugg, T. D. H., and Wood, S. P. (2005) *J. Mol. Biol.* *346*, 253-265.
48. Ollis, D. L., Cheah, E., Cygler, M., Dijkstra, B., Frolow, F., Franken, S. M., Harel, M., Remington, S. J., Silman, I., Schrag, J., Sussman, J. L., Verscheuren, K. H. G., and Goldman, A. (1992) *Protein Eng.* *5*, 197-211.
49. Bugg, T. D. H. (2004) *Bioorg. Chem.* *32*, 367-375.
50. Heikinheimo, P., Goldman, A., Jeffries, C., and Ollis, D. L. (1999) *Structure* *7*, 141-146.
51. Holmquist, M. (2000) *Curr. Prot. Pept. Sci.* *1*, 209-235.
52. Nardini, M., and Dijkstra, B. W. (1999) *Curr. Opin. Struct. Biol.* *9*, 732-737.
53. van Pouderooyen, G., Eggert, T., Jaeger, K. E., and Dijkstra, B. W. (2001) *J. Mol. Biol.* *309*, 215-226.

54. Verger, R. (1997) *Trends Biotechnol.* 15, 32-38.
55. Fersht, A. (1999) *Structure and mechanism in protein science: a guide to enzyme catalysis and protein folding*, W. H. Freeman, New York.
56. Silverman, R. B. (2002) *The Organic Chemistry of Enzyme-Catalyzed Reactions*, Academic Press.
57. Larsen, N. A., Lin, H., Wei, R., Fischbach, M. A., and Walsh, C. T. (2006) *Biochemistry* 45, 10184-10190.
58. Bornscheuer, U. T., and Kazlauskas, R. J. (2004) *Angew. Chem., Int. Ed. Engl.* 43, 6032-6040.
59. Chapus, C., Semeriva, M., Bovierlapierre, C., and Desnuelle, P. (1976) *Biochemistry* 15, 4980-4987.
60. Koller, W., and Kolattukudy, P. E. (1982) *Biochemistry* 21, 3083-3090.
61. Froede, H. C., and Wilson, I. B. (1984) *J. Biol. Chem.* 259, 1010-1013.
62. Li, J., Szittner, R., Derewenda, Z. S., and Meighen, E. A. (1996) *Biochemistry* 35, 9967-9973.
63. Nazi, I., and Wright, G. D. (2005) *Biochemistry* 44, 13560-13566.
64. Hotelier, T., Renault, L., Cousin, X., Negre, V., Marchot, P., and Chatonnet, A. (2004) *Nucleic Acids Res.* 32, D145-D147.
65. Cygler, M., Schrag, J. D., Sussman, J. L., Harel, M., Silman, I., Gentry, M. K., and Doctor, B. P. (1993) *Protein Sci.* 2, 366-382.
66. Kamil, J. P., Tischer, B. K., Trapp, S., Nair, V. K., Osterrieder, N., and Kung, H. J. (2005) *J. Virol.* 79, 6984-6996.
67. Wilson, R. A., Maughan, W. N., Kremer, L., Besra, G. S., and Futterer, K. (2004) *J. Mol. Biol.* 335, 519-530.
68. De Jaco, A., Comoletti, D., Kovarik, Z., Gaietta, G., Radic, Z., Lockridge, O., Ellisman, M. H., and Taylor, P. (2006) *J. Biol. Chem.* 281, 9667-9676.
69. Zeitlmann, L., Sirim, P., Kremmer, E., and Kolanus, W. (2001) *J. Biol. Chem.* 276, 9123-9132.
70. Sussman, J. L., Harel, M., Frolow, F., Oefner, C., Goldman, A., Toker, L., and Silman, I. (1991) *Science* 253, 872-879.
71. Chakravarty, B., Gu, Z. W., Chirala, S. S., Wakil, S. J., and Quioco, F. A. (2004) *Proc. Natl. Acad. Sci. U. S. A.* 101, 15567-15572.

72. Stennicke, H. R., Mortensen, U. H., and Breddam, K. (1996) *Biochemistry* 35, 7131-7141.
73. Bernhardt, P., Hult, K., and Kazlauskas, R. J. (2005) *Angew. Chem., Int. Ed. Engl.* 44, 2742-2746.
74. Connelly, S., Line, K., Isupov, M. N., and Littlechild, J. A. (2005) *Org. Biomol. Chem.* 3, 3260-3262.
75. Ronning, D. R., Klabunde, T., Besra, G. S., Vissa, V. D., Belisle, J. T., and Sacchettini, J. C. (2000) *Nat. Struct. Biol.* 7, 141-146.
76. Liu, J. Q., Kurihara, T., Ichiyama, S., Miyagi, M., Tsunasawa, S., Kawasaki, H., Soda, K., and Esaki, N. (1998) *J. Biol. Chem.* 273, 30897-30902.
77. Janssen, D. B. (2004) *Curr. Opin. Chem. Biol.* 8, 150-159.
78. Nardini, M., Ridder, I. S., Rozeboom, H. J., Kalk, K. H., Rink, R., Janssen, D. B., and Dijkstra, B. W. (1999) *J. Biol. Chem.* 274, 14579-14586.
79. Gruber, K., Gartler, G., Krammer, B., Schwab, H., and Kratky, C. (2004) *J. Biol. Chem.* 279, 20501-20510.
80. Zuegg, J., Gruber, K., Gugganig, M., Wagner, U. G., and Kratky, C. (1999) *Protein Sci.* 8, 1990-2000.
81. Fetzner, S. (2002) *Appl. Microbiol. Biotechnol.* 60, 243-257.
82. Fischer, F., and Fetzner, S. (2000) *FEMS Microbiol. Lett.* 190, 21-27.
83. Fischer, F., Kunne, S., and Fetzner, S. (1999) *J. Bacteriol.* 181, 5725-5733.
84. Frerichs-Deeken, U., Rangelova, K., Kappl, R., Huttermann, J., and Fetzner, S. (2004) *Biochemistry* 43, 14485-14499.
85. Scudder, P. H. (1992) *Electron flow in organic chemistry*, John Wiley & Sons, Inc.
86. Salatin, T. D., and Jorgensen, W. L. (1980) *J. Org. Chem.* 45, 2043-2051.
87. Begley, T. P., and Ealick, S. E. (2004) *Curr. Opin. Chem. Biol.* 8, 508-515.
88. Bennett, J. P., Whittingham, J. L., Brzozowski, A. M., Leonard, P. M., and Grogan, G. (2007) *Biochemistry* 46, 137-144.
89. Grogan, G. (2005) *Biochem. J.* 388, 721-730.
90. Fujii, I., Yasuoka, Y., Tsai, H. F., Chang, Y. C., Kwon-Chung, K. J., and Ebizuka, Y. (2004) *J. Biol. Chem.* 279, 44613-44620.

91. Bateman, R. L., Bhanumoorthy, P., Witte, J. F., McClard, R. W., Grompe, M., and Timm, D. E. (2001) *J. Biol. Chem.* *276*, 15284-15291.
92. Timm, D. E., Mueller, H. A., Bhanumoorthy, P., Harp, J. M., and Bunick, G. J. (1999) *Structure Fold. Des.* *7*, 1023-1033.
93. Momany, C., Levdikov, V., Blagova, L., Lima, S., and Phillips, R. S. (2004) *Biochemistry* *43*, 1193-1203.
94. Phillips, R. S., Sundararaju, B., and Koushik, S. V. (1998) *Biochemistry* *37*, 8783-8789.
95. Schleberger, C., Sachelaru, P., Brandsch, R., and Schulz, G. E. (2007) *J. Mol. Biol.* *367*, 409-418.
96. Sachelaru, P., Schiltz, E., Igloi, G. L., and Brandsch, R. (2005) *J. Bacteriol.* *187*, 8516-8519.
97. Schoefer, L., Braune, A., and Blaut, M. (2004) *Appl. Environ. Microb.* *70*, 6131-6137.
98. Braune, A., Engst, W., and Blaut, M. (2005) *J. Agric. Food Chem.* *53*, 1782-1790.
99. Lam, W. W. Y., and Bugg, T. D. H. (1997) *Biochemistry* *36*, 12242-12251.
100. Lam, W. W. Y., and Bugg, T. D. H. (1994) *J. Chem. Soc., Chem. Comm.*, 1163-1164.
101. Henderson, I. M. J., and Bugg, T. D. H. (1997) *Biochemistry* *36*, 12252-12258.
102. Diaz, E., and Timmis, K. N. (1995) *J. Biol. Chem.* *270*, 6403-6411.
103. Fushinobu, S., Saku, T., Hidaka, M., Jun, S. Y., Nojiri, H., Yamane, H., Shoun, H., Omori, T., and Wakagi, T. (2002) *Protein Sci.* *11*, 2184-2195.
104. Li, C., Montgomery, M. G., Mohammed, F., Li, J. J., Wood, S. P., and Bugg, T. D. H. (2005) *J. Mol. Biol.* *346*, 241-251.
105. Li, J. J., Li, C., Blindauer, C. A., and Bugg, T. D. H. (2006) *Biochemistry* *45*, 12461-12469.
106. Li, C., Li, J. J., Montgomery, M. G., Wood, S. P., and Bugg, T. D. H. (2006) *Biochemistry* *45*, 12470-12479.
107. Bugg, T. D. H., Fleming, S. M., Robertson, T. A., and Langley, G. J. (2002) *Methods Enzymol.* *354*, 106-118.
108. Fleming, S. M., Robertson, T. A., Langley, G. J., and Bugg, T. D. H. (2000) *Biochemistry* *39*, 1522-1531.

109. Speare, D. M., Fleming, S. M., Beckett, M. N., Li, J. J., and Bugg, T. D. H. (2004) *Org. Biomol. Chem.* 2, 2942-2950.
110. Speare, D. M., Olf, P., and Bugg, T. D. H. (2002) *Chem. Commun.*, 2304-2305.
111. Bender, M. L., and Nakamura, K. (1962) *J. Am. Chem. Soc.* 84, 2577-2582.
112. Kanerva, L. T., and Klibanov, A. M. (1989) *J. Am. Chem. Soc.* 111, 6864-6865.
113. Li, J. J., and Bugg, T. D. H. (2007) *Org. Biomol. Chem.* 5, 507-513.
114. Nandhagopal, N., Yamada, A., Hatta, T., Masai, E., Fukuda, M., Mitsui, Y., and Senda, T. (2001) *J. Mol. Biol.* 309, 1139-1151.
115. Habe, H., Morii, K., Fushinobu, S., Nam, J. W., Ayabe, Y., Yoshida, T., Wakagi, T., Yamane, H., Nojiri, H., and Omori, T. (2003) *Biochem. Biophys. Res. Commun.* 303, 631-639.
116. Horsman, G. P., Ke, J., Dai, S., Seah, S. Y. K., Bolin, J. T., and Eltis, L. D. (2006) *Biochemistry* 45, 11071-11086.
117. Humphrey, W., Dalke, A., and Schulten, K. (1996) *J. Molec. Graphics* 14, 33-&.
118. Seah, S. Y. K., Terracina, G., Bolin, J. T., Riebel, P., Snieckus, V., and Eltis, L. D. (1998) *J. Biol. Chem.* 273, 22943-22949.
119. Seto, M., Kimbara, K., Shimura, M., Hatta, T., Fukuda, M., and Yano, K. (1995) *Appl. Environ. Microb.* 61, 3353-3358.
120. Vaillancourt, F. H., Labbe, G., Drouin, N. M., Fortin, P. D., and Eltis, L. D. (2002) *J. Biol. Chem.* 277, 2019-2027.
121. Horsman, G. P., Bhowmik, S., Seah, S. Y. K., Kumar, P., Bolin, J. T., and Eltis, L. D. (2007) *J. Biol. Chem.* 282, 19894-19904.
122. Ausubel, F. M., Brent, R., Kingston, R. E., Moore, D. D., Seidman, J. G., J.A., S., and Struhl, K. (2000) *Current protocols in molecular biology*, J. Wiley & Sons Inc., New York.
123. Bradford, M. M. (1976) *Anal. Biochem.* 72, 248-254.
124. Cornish-Bowden, A. (1995) *Analysis of Enzyme Kinetic Data*, Oxford University Press, New York.
125. Pollard, J. R., Henderson, I. M. J., and Bugg, T. D. H. (1997) *Chem. Commun.*, 1885-1886.
126. Lian, H. L., and Whitman, C. P. (1993) *J. Am. Chem. Soc.* 115, 7978-7984.
127. Hiromi, K. (1979) *Kinetics of Fast Enzyme Reactions*, Halsted Press, Tokyo.

128. Adams, J. A., and Taylor, S. S. (1992) *Biochemistry* 31, 8516-8522.
129. Cole, P. A., Burn, P., Takacs, B., and Walsh, C. T. (1994) *J. Biol. Chem.* 269, 30880-30887.
130. Li, J. J., and Bugg, T. D. H. (2005) *Chem. Commun.*, 130-132.
131. Whitman, C. P., Aird, B. A., Gillespie, W. R., and Stolowich, N. J. (1991) *J. Am. Chem. Soc.* 113, 3154-3162.
132. Cornish-Bowden, A. (2004) *Fundamentals of Enzyme Kinetics*, 3rd ed., Portland Press, London.
133. Zhao, Y. H., Abraham, M. H., and Zissimos, A. M. (2003) *J. Org. Chem.* 68, 7368-7373.
134. Liu, H., Wang, Q. W., and Liu, L. X. (1992) *J. Chem. Educ.* 69, 783-784.
135. Williams, D. H., and Fleming, I. (1995) *Spectroscopic Methods in Organic Chemistry*, 5th ed., McGraw-Hill, London.
136. Takahashi, Y., and Ebrey, T. G. (2003) *Biochemistry* 42, 6025-6034.
137. Hu, J. G. G., Sun, B. Q. Q., Petkova, A. T., Griffin, R. G., and Herzfeld, J. (1997) *Biochemistry* 36, 9316-9322.
138. Lanyi, J. K., and Schobert, B. (2007) *J. Mol. Biol.* 365, 1379-1392.
139. Bhowmik, S., Horsman, G. P., Bolin, J. T., and Eltis, L. D. (2007) *J. Biol. Chem.* 282, 36377-36385.
140. Camps, P., El Achab, R., Gorbig, D. M., Morral, J., Munoz-Torrero, D., Badia, A., Banos, J. E., Vivas, N. M., Barril, X., Orozco, M., and Luque, F. J. (1999) *J. Med. Chem* 42, 3227-3242.
141. Dvir, H., Wong, D. M., Harel, M., Barril, X., Orozco, M., Luque, F. J., Munoz-Torrero, D., Camps, P., Rosenberry, T. L., Silman, I., and Sussman, J. L. (2002) *Biochemistry* 41, 2970-2981.
142. Bhowmik, S., Horsman, G. P., Bolin, J. T., and Eltis, L. D. (2007) *J. Biol. Chem.* 282, 36377-36385.
143. Fersht, A. R. (1987) *Trends in Biochemical Sciences* 12, 301-304.
144. Thorson, J. S., Chapman, E., and Schultz, P. G. (1995) *J. Am. Chem. Soc.* 117, 9361-9362.
145. Usher, K. C., Remington, S. J., Martin, D. P., and Drueckhammer, D. G. (1994) *Biochemistry* 33, 7753-7759.

146. Agarwal, P. K., Webb, S. P., and Hammes-Schiffer, S. (2000) *J. Am. Chem.Soc.* 122, 4803-4812.
147. Thoden, J. B., Wohlers, T. M., Fridovich-Keil, J. L., and Holden, H. M. (2000) *Biochemistry* 39, 5691-5701.
148. Heppel, L. A., Harkness, D. R., and Hilmoie, R. J. (1962) *J. Biol. Chem.* 237, 841-846.
149. Hull, W. E., Halford, S. E., Gutfreund, H., and Sykes, B. D. (1976) *Biochemistry* 15, 1547-1561.

## APPENDIX I: CRYSTALLOGRAPHIC DATA

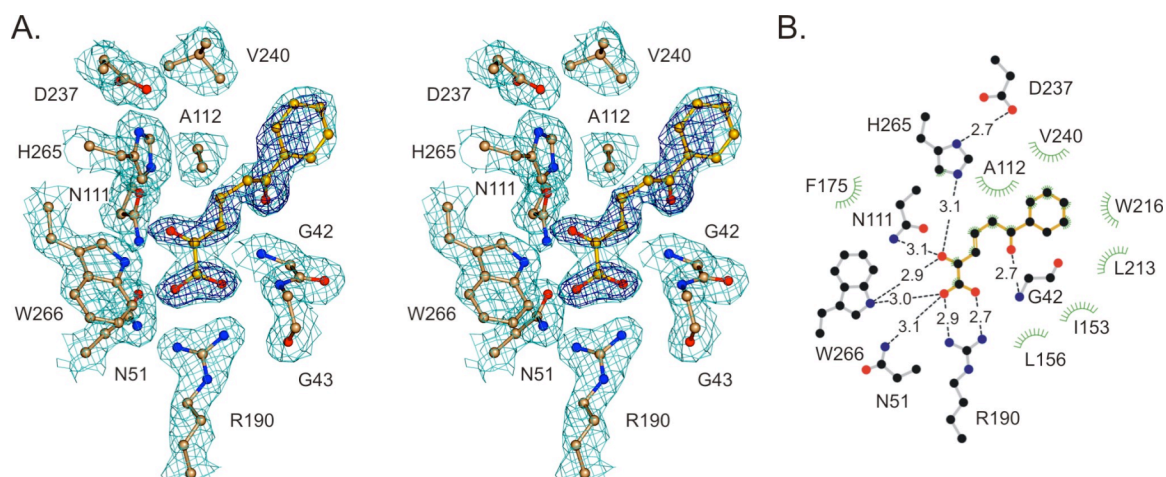


**Figure 44.** Enzyme:substrate interactions in the BphD-S112A:HOPDA complex. (A) Stereo view showing: the refined model; the (2F<sub>o</sub>-F<sub>c</sub>) electron density (cyan, contour level = 1  $\sigma$ ) of the refined structure; and the (F<sub>o</sub>-F<sub>c</sub>) electron density before HOPDA was added to the model (blue, contour level = 3 $\sigma$ ) of the substrate. C, N, and O atoms are coloured gold, blue, and red, respectively. (B) Schematic representation of most enzyme-substrate interactions. C, N, and O atoms are coloured black, blue and red, respectively. Covalent bonds are drawn as orange sticks for the substrate and grey sticks for the protein residues. Protein residues involved in non-polar interactions are represented by green semi-circles with radial lines directed towards the substrate C atoms with which they interact. Hydrogen bonds are shown as dotted lines overlaid with the distance between the donor and acceptor. Not illustrated are interactions of HOPDA with Gly41, Gly43, Ala46, Met113, Gly138, and Gly139, including two hydrogen bonds involving the peptide NHs of Gly43 and Met113 and HOPDA's carboxylate and 6-oxo groups, respectively. Taken from reference (121).

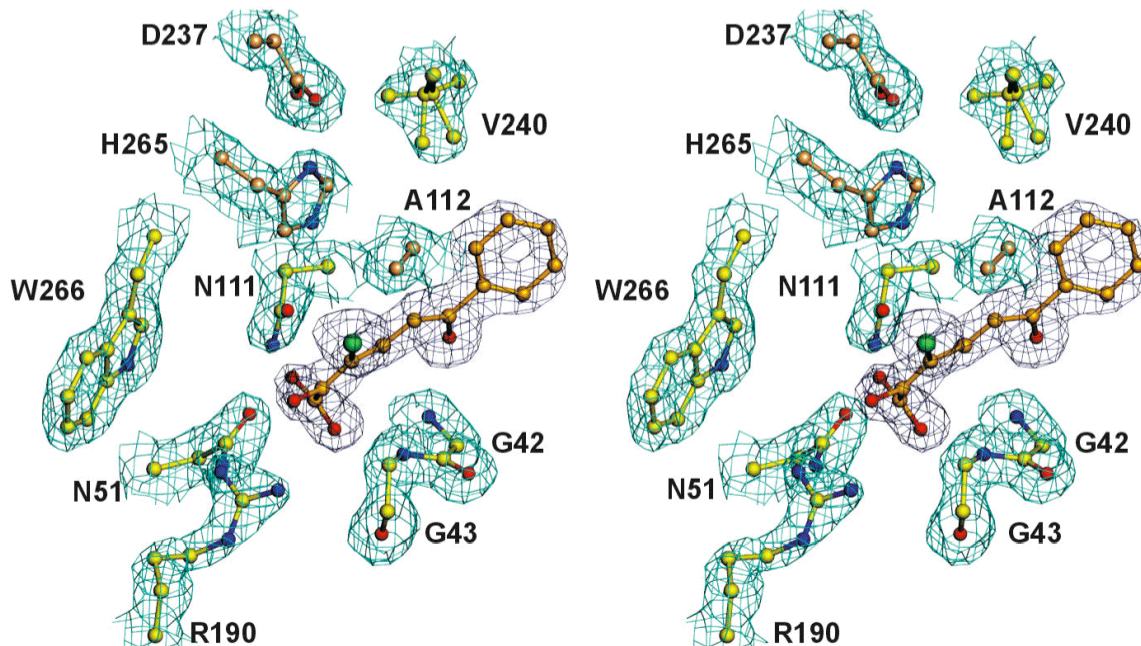


**Figure 45.** Stereo view showing: the refined model of S112A:3-Cl HOPDA complex; the  $(2F_o-F_c)$  electron density (cyan, contour level =  $1\sigma$ ) of the refined structure; and the  $(F_o-F_c)$  electron density before 3-Cl HOPDA was added to the model (blue, contour level =  $3\sigma$ ). The C atoms of His265 and Ala112 are colored wheat, C atoms in other proteins residues are yellow, and C atoms in the ligand are orange. N, O, S and Cl atoms are colored blue, red, olive and green, respectively. Taken from (139).

**Table 6.** Results of model refinement for BphD variants and complexes.

| Parameter or Statistic                                     | Protein: ligand |             |             |             |              |             |            |       |              |
|--|-----------------|-------------|-------------|-------------|--------------|-------------|------------|-------|--------------|
|  | Wild-type:      |             | S112A:      |             | S112A:H265A: |             | S112A:3-Cl |       | S112A/H265A: |
|  | malonate        | malonate    | malonate    | HOPDA       | HOPDA        | HOPDA       | HOPDA      | HOPDA | HOPDA        |
| Resolution range (Å)                                       | 117.0 - 2.30    | 83.0 - 1.68 | 82.2 - 2.07 | 82.5 - 1.82 | 1.70         | 82.5 - 1.57 |            |       |              |
| $R$ (%)  | 18.0            | 17.4        | 18.8        | 17.1        | 15.5         | 17.6        |            |       |              |
| $R_{\text{free}}$ (%)                                      | 27.0            | 20.0        | 27.0        | 20.5        | 19.3         | 20.0        |            |       |              |
| Est. coordinate error <sup>a</sup>                         | 0.24            | 0.09        | 0.20        | 0.11        | 0.09         | 0.08        |            |       |              |
| <b>Model content</b>                                       |                 |             |             |             |              |             |            |       |              |
| Protein atoms  | 4520            | 2264        | 2255        | 2255        | 2289         | 2259        |            |       |              |
| Malonate molecules   | 2               | 2           | 2           | 0           | 1            | 1           |            |       |              |
| Water molecules  | 107             | 143         | 71          | 113         | 165          | 156         |            |       |              |
| <b>Average <math>B</math> factors</b><br>(Å <sup>2</sup> ) |                 |             |             |             |              |             |            |       |              |
| Protein: chain <sup>b</sup>                                | 35, 64          | 18          | 36          | 30          | 21           | 26          |            |       |              |
| Water atoms  | 34              | 23          | 37          | 33          | 29           | 32          |            |       |              |
| All atoms  | 49              | 18          | 36          | 30          | 21           | 26          |            |       |              |
| <b>RMSD from target</b>                                    |                 |             |             |             |              |             |            |       |              |
| Bond lengths (Å)   | 0.022           | 0.009       | 0.015       | 0.013       | 0.010        | 0.010       |            |       |              |
| Bond angles (degrees)                                      | 2.0             | 1.2         | 1.6         | 1.3         | 1.2          | 1.2         |            |       |              |

<sup>a</sup> Cruickshank's diffraction-component precision index as calculated by REFMAC.<sup>b</sup> For the wild-type:malonate complex, the first value is for monomer A and the second is for monomer B

**Table 7.** Results of restrained refinements assuming different isomers of HOPDA.

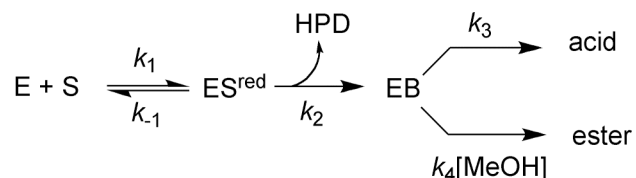
| Bond and Property |                              | HOPDA Isomer |               |                 |
|-------------------|------------------------------|--------------|---------------|-----------------|
|                   |                              | 2-enol       | 2-keto, 6-oxo | 2-keto, 6-oxido |
| C2-C3             | Bonding                      | Double       | Single        | Single          |
|                   | Restraint <sup>a</sup> (°)   | 180          | —             | —               |
|                   | Init. angle <sup>b</sup> (°) | 179          | 180           | 158             |
|                   | Ref. angle <sup>b</sup> (°)  | 175          | 175           | 179             |
| C3-C4             | Bonding                      | Single       | Double        | Double          |
|                   | Restraint (°)                | —            | 180           | 180             |
|                   | Init. angle (°)              | 139          | 180           | 165             |
|                   | Ref. angle (°)               | 145          | 180           | 178             |
| C4-C5             | Bonding                      | Double       | Single        | Single          |
|                   | Restraint (°)                | 0            | —             | —               |
|                   | Init. angle (°)              | 1            | 78            | 12              |
|                   | Ref. angle (°)               | 12           | 69            | 70              |
| C5-C6             | Bonding                      | Single       | Single        | Double          |
|                   | Restraint (°)                | —            | —             | 180             |
|                   | Init. angle (°)              | 164          | 156           | 178             |
|                   | Ref. angle (°)               | 178          | 150           | 150             |

<sup>a</sup> Double bonds were restrained with an estimated standard deviation of 0 degrees; single bonds were not restrained.

<sup>b</sup> “Init. angle” is the value in the initial model as fit to the density manually; deviations of up to 15° from the expected restraint were allowed. “Ref. value” is the value measured after restrained refinement.

## APPENDIX II: DERIVATIONS OF STEADY-STATE EQUATIONS

### A) Nucleophilic mechanism



At steady-state, the concentrations of  $[\text{ES}^{\text{red}}]$  and  $[\text{EB}]$  will not change with time, as expressed by equations (1) and (2).

$$\begin{aligned}
 (1) \quad d[\text{ES}^{\text{red}}]/dt = 0 &= k_1[\text{E}][\text{S}] - k_{-1}[\text{ES}^{\text{red}}] - k_2[\text{ES}^{\text{red}}] \\
 \therefore k_1[\text{E}][\text{S}] &= k_{-1}[\text{ES}^{\text{red}}] + k_2[\text{ES}^{\text{red}}]
 \end{aligned}$$

$$\begin{aligned}
 (2) \quad d[\text{EB}]/dt = 0 &= k_2[\text{ES}^{\text{red}}] - k_3[\text{EB}] - k_4[\text{MeOH}][\text{EB}] \\
 \therefore [\text{ES}^{\text{red}}] &= [\text{EB}] \left( \frac{k_3 + k_4[\text{MeOH}]}{k_2} \right)
 \end{aligned}$$

Equation (3) accounts for the concentration of free enzyme,  $[\text{E}]$ , where  $[\text{E}]_0$  is the total concentration of enzyme.

$$(3) \quad [\text{E}] = [\text{E}]_0 - [\text{ES}^{\text{red}}] - [\text{EB}]$$

The reaction rate can be described by equation (4):

$$(4) \quad v = k_3[\text{EB}] + k_4[\text{MeOH}][\text{EB}] = [\text{EB}](k_3 + k_4[\text{MeOH}])$$

Substituting equation (3) into equation (1) gives equation (5):

$$(5) \quad k_1[\text{S}][\text{E}]_0 = [\text{ES}^{\text{red}}](k_1[\text{S}] + k_{-1} + k_2) + k_1[\text{S}][\text{EB}]$$

Substituting equation (2) into equation (5):

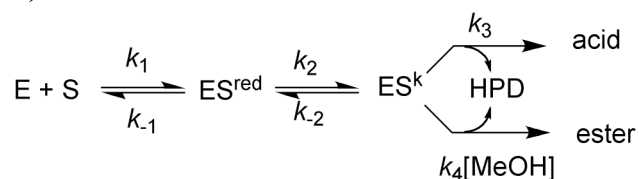
$$(6) \quad [\text{EB}] = \frac{k_1 k_2 [\text{S}] [\text{E}]_0}{k_1 [\text{S}] k_3 + k_{-1} k_3 + k_2 k_3 + k_1 [\text{S}] k_4 [\text{MeOH}] + k_{-1} k_4 [\text{MeOH}] + k_2 k_4 [\text{MeOH}] + k_1 [\text{S}] k_2}$$

Equation (4) may then be substituted with equation (6):

$$(7) v = \frac{\frac{k_2(k_3 + k_4[\text{MeOH}])}{k_2 + k_3 + k_4[\text{MeOH}]} [E]_0[S]}{[S] + \frac{(k_2 + k_{-1})(k_3 + k_4[\text{MeOH}])}{k_1(k_2 + k_3 + k_4[\text{MeOH}])}}$$

Equation (7) takes the form of the Michaelis-Menten equation, yielding the expressions for  $k_{\text{cat}}$  and  $K_m$  shown in Figure 24A.

### B) General base mechanism



Equations may be set up as in case A above.

$$(1) d[\text{ES}^{\text{red}}]/dt = 0 = k_1[\text{S}][\text{E}] - k_{-1}[\text{ES}^{\text{red}}] - k_2[\text{ES}^{\text{red}}] + k_{-2}[\text{ES}^{\text{k}}]$$

$$(2) d[\text{ES}^{\text{k}}]/dt = 0 = k_2[\text{ES}^{\text{red}}] - k_{-2}[\text{ES}^{\text{k}}] - k_3[\text{ES}^{\text{k}}] - k_4[\text{MeOH}][\text{ES}^{\text{k}}]$$

$$\therefore [\text{ES}^{\text{red}}] = [\text{ES}^{\text{k}}] \left( \frac{k_{-2} + k_3 + k_4[\text{MeOH}]}{k_2} \right)$$

$$(3) [\text{E}] = [\text{E}]_0 - [\text{ES}^{\text{red}}] - [\text{ES}^{\text{k}}]$$

$$(4) v = k_3[\text{ES}^{\text{k}}] + k_4[\text{MeOH}][\text{ES}^{\text{k}}]$$

$$= [\text{ES}^{\text{k}}](k_3 + k_4[\text{MeOH}])$$

Substituting equation (3) into (1) yields:

$$(5) k_1[\text{S}][\text{E}]_0 = [\text{ES}^{\text{red}}](k_1[\text{S}] + k_{-1} + k_2) + k_1[\text{S}][\text{ES}^{\text{k}}] - k_{-2}[\text{ES}^{\text{k}}]$$

Substituting equation (2) into (5):

$$(6) [\text{ES}^{\text{k}}] = \frac{k_1 k_2 [\text{S}][\text{E}]_0}{k_1[\text{S}](k_{-2} + k_2 + k_3 + k_4[\text{MeOH}]) + k_{-1}(k_{-2} + k_3 + k_4[\text{MeOH}]) + k_2(k_3 + k_4[\text{MeOH}])}$$

Equation (6) may be substituted into equation (4) to obtain the steady-state rate equation (7), which contains terms describing  $k_{\text{cat}}$  and  $K_m$  as shown in Figure 24B.

$$(7) v = \frac{\frac{k_2(k_3 + k_4[\text{MeOH}])}{k_{-2} + k_2 + k_3 + k_4[\text{MeOH}]} [E]_0[S]}{[S] + \frac{k_{-1}(k_{-2} + k_3 + k_4[\text{MeOH}]) + k_2(k_3 + k_4[\text{MeOH}])}{k_1(k_{-2} + k_2 + k_3 + k_4[\text{MeOH}])}}$$